SpringerBriefs in Applied Sciences and Technology

Jianhang Chen · Yongliang Li · Junwen Zhang

Bond Failure Mechanism of Fully Grouted Rock Bolts

OPEN ACCESS

Springer

SpringerBriefs in Applied Sciences and Technology

SpringerBriefs present concise summaries of cutting-edge research and practical applications across a wide spectrum of fields. Featuring compact volumes of 50 to 125 pages, the series covers a range of content from professional to academic.

Typical publications can be:

- A timely report of state-of-the art methods
- An introduction to or a manual for the application of mathematical or computer techniques
- A bridge between new research results, as published in journal articles
- A snapshot of a hot or emerging topic
- An in-depth case study
- A presentation of core concepts that students must understand in order to make independent contributions.

SpringerBriefs are characterized by fast, global electronic dissemination, standard publishing contracts, standardized manuscript preparation and formatting guidelines, and expedited production schedules.

On the one hand, **SpringerBriefs in Applied Sciences and Technology** are devoted to the publication of fundamentals and applications within the different classical engineering disciplines as well as in interdisciplinary fields that recently emerged between these areas. On the other hand, as the boundary separating fundamental research and applied technology is more and more dissolving, this series is particularly open to trans-disciplinary topics between fundamental science and engineering.

Indexed by EI-Compendex, SCOPUS and Springerlink.

Jianhang Chen · Yongliang Li · Junwen Zhang

Bond Failure Mechanism of Fully Grouted Rock Bolts

Springer

Jianhang Chen
School of Energy and Mining Engineering
China University of Mining
and Technology (Beijing)
Beijing, China

Yongliang Li
School of Energy and Mining Engineering
China University of Mining
and Technology (Beijing)
Beijing, China

Junwen Zhang
School of Energy and Mining Engineering
China University of Mining
and Technology (Beijing)
Beijing, China

ISSN 2191-530X ISSN 2191-5318 (electronic)
SpringerBriefs in Applied Sciences and Technology
ISBN 978-981-99-0500-3 ISBN 978-981-99-0498-3 (eBook)
https://doi.org/10.1007/978-981-99-0498-3

This Springer imprint is published by the registered company Springer Nature Singapore Pte Ltd.
The registered company address is: 152 Beach Road, #21-01/04 Gateway East, Singapore 189721, Singapore

Preface

The mining industry behaves a significant part in the current society. They provide coal and hard rock resources to guarantee the normal operation of the current society. To guarantee that coal mines and hard rock mines can operate smoothly, ground control techniques are compulsory. Among kinds of ground control techniques, rock bolts are widely accepted and applied in mine sites. They can improve the stability of the excavated rock masses. Consequently, the safety of underground excavations and operators can be guaranteed.

In situ tests show that although rock bolts have been used for a long time, failure of the rock bolting system still occurs. Moreover, it is more common to encounter the bond failure of the bolt/grout interface. This leads to improper load transfer between rock bolts and surrounding rock masses. Furthermore, this induces safety concern for the normal operation of mine sites.

Aiming at solving this issue, this book summarises the recent research work regarding by load transfer of rock bolts conducted by the authors. This book is divided into seven chapters. Within those seven chapters, the shear behaviour of the bolt/grout interface, the shear failure of the cement-based grout, the load transfer performance of rock bolts and the parameter analysis on the performance of rock bolts are studied. This book is beneficial for researchers and engineers to better understanding the load transfer performance of rock bolts. Moreover, it can help researchers and engineers to propose and develop new approaches to prevent failure of the rock bolting system.

The publication of this book is financially supported by the National Natural Science Foundation of China (52034009, 52174093, 51904302). The authors also

would like to thank the support provided by the China University of Mining and Technology (Beijing), and International Joint Research Laboratory of Henan Province for Underground Space Development and Disaster Prevention, Henan Polytechnic University, China.

Beijing, China

Jianhang Chen
Yongliang Li
Junwen Zhang

Contents

Chapter 1
Introduction

1.1 Background

Mining engineering plays a significant role in the current society. It provides the energy resources including coal and hard rocks to guarantee the normal operation of the society. Therefore, not only developed countries but also developing countries still pay much attention to their mining industry.

This is more obvious in China. For example, the statistical data shows that more than a half of the electricity still comes from the thermal power generation. Therefore, continuous production of coal resources is important in guaranteeing the normal power generation and convenient running of the society.

To make sure that coal mines can operate stability, the ground control techniques are significant. It is well known that after the rock masses around the mineral resources are excavated, the rock masses around the excavation tend to move towards the excavation direction. Therefore, to maintain the stability of the underground excavations, ground control techniques and instruments should be used.

Among kinds of ground control techniques and instruments, rock bolts are widely accepted and used by mines. The rock bolt is a bar or a cable that is installed in the rock mass. Although rock bolts can be divided into frictional bolts or mechanical bolts, the laboratory and in situ tests show that the mechanical bolts have better performance.

For mechanical rock bolts, either resin-based or cement-based grout can be used as the anchorage agent. These different grouts can be poured into the drilled borehole to bond the rock bolt with the surrounding rock mass. As for the in situ practice, the point-anchored method or the fully grouted method can be used. However, previous research shows that when the fully grouted method is used, there is a better load transfer between the rock bolt and the surrounding rock masses [1].

Nevertheless, when the fully grouted rock bolts are used, failure of the rock bolting system still occurs. A summary of the rock bolting failure modes shows that the rock bolting system can fail by different types, including the bond failure at the

J. Chen et al., *Bond Failure Mechanism of Fully Grouted Rock Bolts*,
SpringerBriefs in Applied Sciences and Technology,
https://doi.org/10.1007/978-981-99-0498-3_1

bolt/grout interface, the bond failure at the grout/rock interface, shear failure of the grout column, shear failure of the rock mass and tensile rupture of the rock bolt [2].

However, it is more common to encounter the bond failure at the bolt/grout interface [3]. The reason is that the shear strength of the bolt/grout interface is much smaller than the tensile strength of the rock bolt. Moreover, in the rock bolting system, the bolt/grout interface has the relatively smaller contact area. This leads to the shear stress concentration at the bolt/grout interface. Consequently, bond failure of the bolt/grout interface is more likely to occur.

To better understand the load transfer mechanism of fully grouted rock bolts and prevent bond failure of the bolt/grout interface, this book summarised the previous research work conducted by the authors regarding the anchorage performance of rock bolts. This book is divided into seven chapters. Within those seven chapters, the shear behaviour of the bolt/grout interface, the shear failure of the cement-based grout, the load transfer performance of rock bolts and the parameter analysis on the performance of rock bolts are studied. This book is beneficial for researchers and engineers to better understanding the load transfer performance of rock bolts. Moreover, it can help researchers and engineers to propose and develop new approaches to prevent failure of the rock bolting system.

1.2 Book Outline

This chapter aims at providing the general introduction for this book. The general background of rock bolting is illustrated. Then, the basic structure of this book is presented.

Chapter 2 gives a literature review on the shear stress propagation mechanism in the rock reinforcement system. More attention is paid to the bolt/grout interface. The investigation approaches used in previous research are summarised. Moreover, the shear stress propagation process at the bolt/grout interface is elaborated. And a detailed discussion is added to analyse the shear stress propagation mechanism of the bolt/grout interface.

Chapter 3 studies the shear behaviour of the cement-based grout. Two different water-cement (w/c) ratios are used: 0.4 and 0.5. The numerical compressive strength tests are conducted to calibrate the input parameters. Then, the direct shear test is simulated to study the shear behaviour of the cement-based grout. Experimental direct shear tests are used to confirm the accuracy of the numerical direct shear test. Moreover, the shear stress distribution in the cement-based grout is analysed.

Chapter 4 presents an analytical modelling to investigate the shear behaviour of the bolt/grout interface. The bond-slip behaviour of the bolt/grout interface is simulated with a tri-linear model. An analytical model is developed based on the shear stress propagation mechanism at the bolt/grout interface. The pull-out performance of the rock bolts is divided into the elastic, elastic-softening, elastic-softening-debonding, softening-debonding and debonding stages. Credibility of the analytical model is validated with experimental pull-out tests.

Chapter 5 studies the influence of the confining medium on the load transfer performance of rock bolts. In this chapter, the tri-linear model is still used to depict the shear behaviour of the bolt/grout interface. Then, this tri-linear model is incorporated into the rock bolting system. After that, based on this analytical model, the influence of the confining medium on the load transfer capacity of rock bolts is studied. Moreover, the critical influence diameter of the confining medium for the rock bolts is analysed.

Chapter 6 conducts a comprehensive parameter study on the load transfer performance of rock bolts. The influence of the bolt diameter, elastic modulus of bolts, grouted length of bolts and bond slipping when bond strength reaches is studied. The maximum load transfer capacity of rock bolts is analysed and compared. Moreover, when the rock bolt reaches the maximum load transfer capacity, the shear stress distribution state of the bolt/grout interface is analysed.

Chapter 7 proposes an analytical model for fully grouted rock bolts based on a nonlinear bond-slip model. In this chapter, an exponential nonlinear model is used to depict the shear behaviour of the bolt/grout interface. Then, the load transfer performance of rock bolt is successfully simulated. Experimental pull-out tests are used to confirm that this nonlinear model can be used to simulate the pull-out performance of rock bolts. Moreover, the load distribution along the axial direction of rock bolts is studied.

References

1. A. Kilik, E. Yasar, A.G. Celik, Effect of grout properties on the pull-out load capacity of fully grouted rock bolt. Tunn. Undergr. Space Technol. **17**, 355–362 (2002). https://doi.org/10.1016/S0886-7798(02)00038-X
2. J. Chen, B. Zeng, L. Liu, K. Tao, H. Zhao, C. Zhang, J. Zhang, D. Li, Investigating the anchorage performance of full-grouted anchor bolts with a modified numerical simulation method. Eng. Fail. Anal. **141**, 1–14 (2022). https://doi.org/10.1016/j.engfailanal.2022.106640
3. S. Ma, X. Zhu, W. Qin, S. Hu, Determination of the bond-slip relationship of fully grouted rockbolts. Environ. Earth Sci. **77**(9), 325–326 (2018). https://doi.org/10.1007/s12665-018-7495-2

Chapter 2
Analysis on the Shear Stress Propagation Mechanism in the Rock Reinforcement System

2.1 Introduction

In rock mechanics, failure of rock masses is commonly encountered [1]. This is because fractures distribute non-uniformly in rock masses [2, 3]. Moreover, experiment work proves that rock masses which are full of fractures have quite low strength [4].

This is more prominent when the rock masses are subjected to manual excavation [5]. For example, in civil engineering and mining engineering, excavation activities are performed to create tunnels, chambers or roadways [6]. These tunnels and roadways will be later used in serving transportation and ventilation [7].

Attention is paid that this manual excavation disturbs the initial stability of rock masses [8]. Moreover, due to manual excavation, stress concentration occurs in rock masses [9, 10]. Consequently, fractures are likely to develop in rock masses [11–13]. This further weakens the rock mass strength.

To guarantee the safety of rock mass excavation, rock reinforcement bolts are commonly used [14–16]. Experimental work proves that rock reinforcement bolts can combine the jointed rock mass. Moreover, once rock masses converge, shear deformation will occur in the grout column. Consequently, stress can be transferred in the rock reinforcement system [17].

During the loading process, the shear stress propagation plays a significant role [18]. Therefore, proper understanding the shear stress propagation mechanism in the rock reinforcement system is quite significant.

This paper aims at revealing the shear stress propagation mechanism in the rock reinforcement system. To realise this purpose, a literature review was conducted. This study is beneficial to propose new reinforcement approaches to prevent rock mass failure.

J. Chen et al., *Bond Failure Mechanism of Fully Grouted Rock Bolts*,
SpringerBriefs in Applied Sciences and Technology,
https://doi.org/10.1007/978-981-99-0498-3_2

2.2 Previous Study on the Shear Stress Propagation

2.2.1 Investigation Approaches

To study the shear stress propagation mechanism in the rock reinforcement system, previous researchers adopted various approaches. Generally, investigation approaches can be classified into three different types: experimental tests [19], analytical simulation [20, 21] and numerical simulation [12].

Experimental tests should be the most credible one. Specifically, strain gauges are adhered on the bolt/grout interface [22]. Then, this instrumented bolt is installed in a rock block. Grout is used to bond the bolt with the rock block [23, 24]. After full curing, the bolt is pulled out. During testing, tensile force distribution along the bolt can be measured. Then, Eq. (2.1) is adopted to simply calculate the shear stress at the bolt/grout interface [25].

$$\tau = \frac{D_{\mathrm{b}} E_{\mathrm{b}} (\varepsilon_1 - \varepsilon_2)}{4\Delta L} \tag{2.1}$$

where τ: shear stress at the bolt/grout interface; D_{b}: bolt diameter; E_{b}: elastic modulus of the bolt; ε: tensile strain of the bolt; ΔL: spacing between two adjacent strain gauges.

This approach has been used by a number of researchers [26]. However, a shortcoming is that the attached strain gauges are likely to be stripped from the bolt/grout interface. To solve this issue, Chekired et al. [27] developed the tension measuring device. This device can be mounted on the bolt to measure the strain distribution. Additionally, Martin et al. [28] proposed replacing central wire in the cable bolt with a modified wire. Specifically, along this modified wire, strain gauges were attached.

Besides, analytical simulation is an efficient approach to study the shear stress propagation mechanism [29]. Specifically, although the bolt may have a long length, infinitesimal method can be used to analyse the shear stress at the bolt/grout interface, as shown in Eq. (2.2) [30]:

$$\tau = \frac{D_{\mathrm{b}}}{4} \frac{\mathrm{d}\sigma_{\mathrm{b}}(x)}{\mathrm{d}x} \tag{2.2}$$

where $\mathrm{d}\sigma_{\mathrm{b}}(x)$: the increment of the tensile stress in the bolt.

Then, it is assumed that the bolt/grout interface has the same mechanical property [31]. And a bond-slip equation can be used to depict the relationship between the shear stress at the bolt/grout interface and the slip [32]. Through incorporating the bond-slip equation into Eq. (2.2), analytical equations can be developed.

This analytical approach was initially proposed by Farmer [33]. However, at that period, the debonding behaviour was not considered. Later, this analysis method was adopted by others [34]. Aydan et al. [35] made a significant improvement on analytical simulation. Their innovation is that the classic tri-linear equation was proposed to

describe the slip behaviour of the bolt/grout interface. Based on the tri-linear equation, the bolt/grout interface encountered the elastic, softening and debonding behaviour. Therefore, the bonding and debonding behaviour of the bolt/grout interface can be simulated.

Moreover, the tri-linear equation may be simplified into the bi-linear equation to evaluate the shear stress propagation of the bolt/grout interface [36]. The main difference between the bi-linear equation and the tri-linear equation is that there is no linear softening behaviour in the bi-linear equation.

In recent years, numerical simulation becomes more popular in rock reinforcement analysis. It is because numerical simulation is powerful in establishing and calculating complicated structures [37]. As for the rock reinforcement analysis, more research was focused on using the structure element, such as the cable or pile. There is a significant difference between the cable and pile. Specifically, the cable only considers the longitudinal performance of rock reinforcement bolts. In contrast, the pile can analyse both the longitudinal performance and the lateral performance of rock reinforcement bolts.

The advantage is that numerical elements have already been created by the commercial company. Therefore, users can conveniently adopt the structure element to simulate different rock reinforcement cases. In contrast, the shortcoming is that the original constitutive equation may not truly reflect the proper behaviour of the rock reinforcement system. For example, in the structure element of cable, the bolt/grout interface is assumed to deform following an elastic perfectly plastic equation, as shown in Eq. (2.3) [38].

$$\begin{cases} \tau = k_{\mathrm{g}}\delta\left(\delta \le \delta_{\mathrm{p}}\right) \\ \tau = \tau_{\mathrm{p}}\left(\delta > \delta_{\mathrm{p}}\right) \end{cases} \tag{2.3}$$

where k_{g}: shear stiffness of the grout column; δ: slip of the bolt/grout interface; δ_{p}: slip of the bolt/grout interface when the peak strength reaches; τ_{p}: peak strength of the bolt/grout interface.

It neglects the post-failure behaviour of the bolt/grout interface. Therefore, it cannot truly simulate the loading performance of bolts without modification.

Nevertheless, the commercial software usually reserves the secondary development interface. For example, for the structure element of cable, the Itasca Company prepares a number of FISH functions [39]. For the structure element of pile, the Itasca Company creates the TABLE function [40]. Therefore, users can use these FISH functions or TABLE function to modify the original rock reinforcement elements. For example, Fig. 2.1 shows the comparison between the original pile and the revised pile. Apparently, with the original pile, at the end of the shear stress propagation process, the shear stress at the full bolt/grout interface equalled the peak strength. This overestimated the loading capacity of bolts. In contrast, with the modified pile, there was always a non-uniform shear stress distribution at the bolt/grout interface. This was more consistent with the experimental test results. Consequently, it saw a wide application of the commercial numerical tools in rock reinforcement analysis [41].

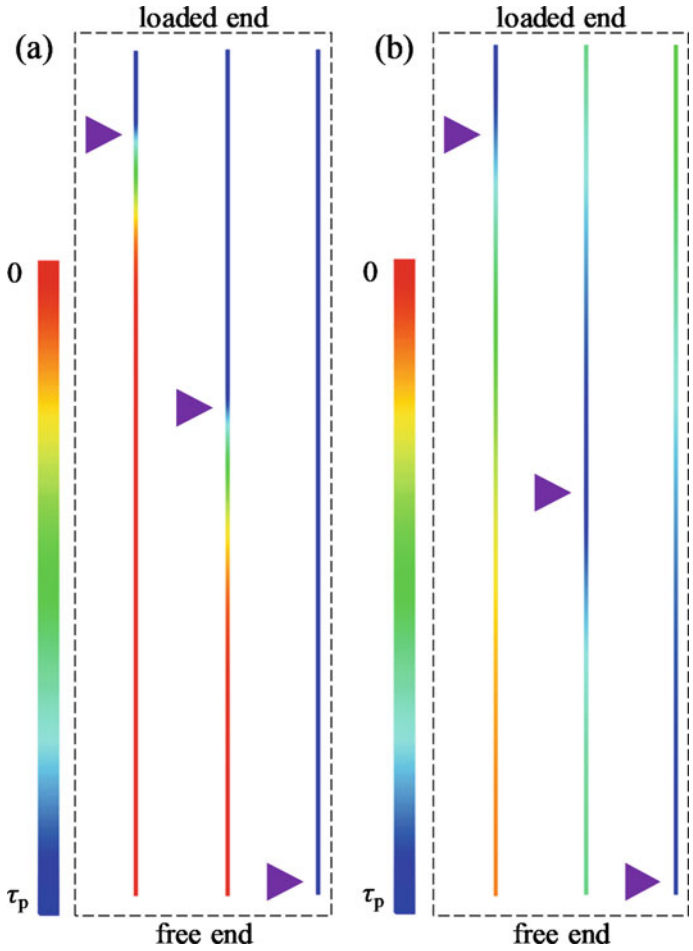

Fig. 2.1 Comparison between the structure element of pile in analysing the shear stress propagation process: **a** original pile; **b** revised pile

2.2.2 Shear Stress Propagation Mechanism

Based on previous research, it is accepted that the shear stress at the bolt/grout interface may have a uniform distribution if the anchor length was short enough [42]. Benmokrane et al. [43] indicated that when the anchor length is less than four times of the bolt diameter, the shear stress can be treated equal. Based on this concept, Eq. (2.4) was used to calculate the shear stress at the bolt/grout interface [44]:

$$\tau = \frac{F}{\pi D_b L} \tag{2.4}$$

where F: pull-out force; L: anchor length.

Attention should be noted that Eq. (2.4) is valid when the anchor length is constant during the pull-out process. Nevertheless, it is more common to encounter the scenario where the anchor length decreases gradually. Then, Eq. (2.5) can be used to calculate the shear stress [44].

$$\tau = \frac{F}{\pi D_{\mathrm{b}}(L - u_{\mathrm{b}})} \tag{2.5}$$

where u_{b}: pull-out displacement.

More importantly, rock reinforcement bolts usually have a long length [45]. In this case, after the bolt is subjected to tensile loading, non-uniform shear stress distribution occurs. For the laboratory monotonous loading condition, the bolt usually has two ends. One is embedded in the rock block, and it is called as the internal end. By contrast, the other one is left outside and it is called as the external end. Since there is a non-uniform shear stress distribution, shear stress propagation between two ends of the bolts generates.

Some research indicated that the maximum shear stress under each loading level was likely to occur around the same position [46]. Moreover, that position was close to the borehole collar.

In contrast, it is more common to see that during the initial load process, shear stress at the borehole collar increased gradually. With the loading increasing, the shear stress at the borehole collar increased to the peak strength. Then, it started dropping. More interestingly, the maximum shear stress moved towards the internal end direction. This shear stress propagation ended when the shear stress at the internal end of the bolt reached the peak strength.

As a validation of this shear stress propagation concept, Rong et al. [47] conducted laboratory pull-out tests on bolts. Strain gauges were attached on the bolt/grout interface to record the tensile force distribution. Later, Ma et al. [44] analysed these experimental data. Equation (2.1) was used to calculate the shear stress at the bolt/grout interface. The analysis results showed that at the initial loading grade, the shear stress at the borehole collar increased gradually. However, after a certain loading level, the shear stress at the borehole collar reached the peak strength. With the loading level further increasing, the maximum shear stress propagated gradually towards the external end. This analysis result was consistent with the above shear stress propagation concept. Therefore, the experimental work and the corresponding data analysis proved the reliability of the shear stress propagation concept.

Additionally, the analytical simulation and numerical simulation can better reflect the shear stress propagation process. Ren et al. [48] used the classic tri-linear equation to depict the slip behaviour of the bolt/grout interface. They analysed the shear stress propagation process at the bolt/grout interface. The results showed that the maximum shear stress at the bolt/grout interface propagated from the external end to the internal end. Moreover, although each point at the bolt/grout interface experienced

the elastic, softening and debonding behaviour, the full bolt/grout interface underwent five different grades. They were the elasticity, elasticity-weakening, elasticity-weakening-debonding, weakening-debonding and debonding grades. Later, Blanco Martín et al. [49] indicated that when the tri-linear equation was used to depict the slip behaviour of the bolt/grout interface, the full bolt/grout interface may undergo the pure softening grade.

It should be mentioned that when different bond-slip equations are used, the full bolt/grout interface may undergo different grades. For example, Chen et al. [50] indicated that when a bi-linear equation was used to depict the slip behaviour of the bolt/grout interface, the full bolt/grout interface only experienced three grades: the elastic grade, elastic-debonding grade and debonding grade.

Although different bond-slip equations can be used, the shear stress propagation mechanism was consistent. Specifically, the maximum shear stress at the bolt/grout interface consistently propagated from the external end to the internal end, as shown in Fig. 2.2.

This finding was also confirmed with numerical simulation. Nemcik et al. [38] modified the original structure element in Fast Lagrangian Analysis of Continua (FLAC) and simulated the shear stress propagation process at the bolt/grout interface. A nonlinear bond-slip equation was used. The results showed that each point at the bolt/grout interface obeyed the same nonlinear bond-slip equation. With the loading level increasing, the maximum shear stress at the bolt/grout interface propagated towards the internal end. This finding was consistent with the others [51].

2.3 Discussion

The shear stress at the bolt/grout interface plays a significant role in determining the loading capacity of bolts [52]. Under the static loading condition, the loading capacity of bolts equals the sum of the shear force at the bolt/grout interface [53]. Since the shear stress at the bolt/grout interface can be calculated directly with the shear force at the bolt/grout interface, as shown in Eq. (2.6), there is a close relationship between the shear stress at the bolt/grout interface and the loading capacity of bolts [54].

$$\tau = \frac{F_s}{A_s} \tag{2.6}$$

where F_s: shear force at the bolt/grout interface; A_s: contact area between the bolt and the grout column.

Therefore, it is valuable to understand the shear stress propagation mechanism of bolts. To realise this purpose, previous researchers used various approaches. It is believed that the experimental approach is more credible. This is because compared with the experimental approach, the analytical simulation and numerical simulation usually relied on a number of assumptions [55]. Whether those assumptions are reasonable is doubted. In analytical simulation, it is usually assumed that the bolt,

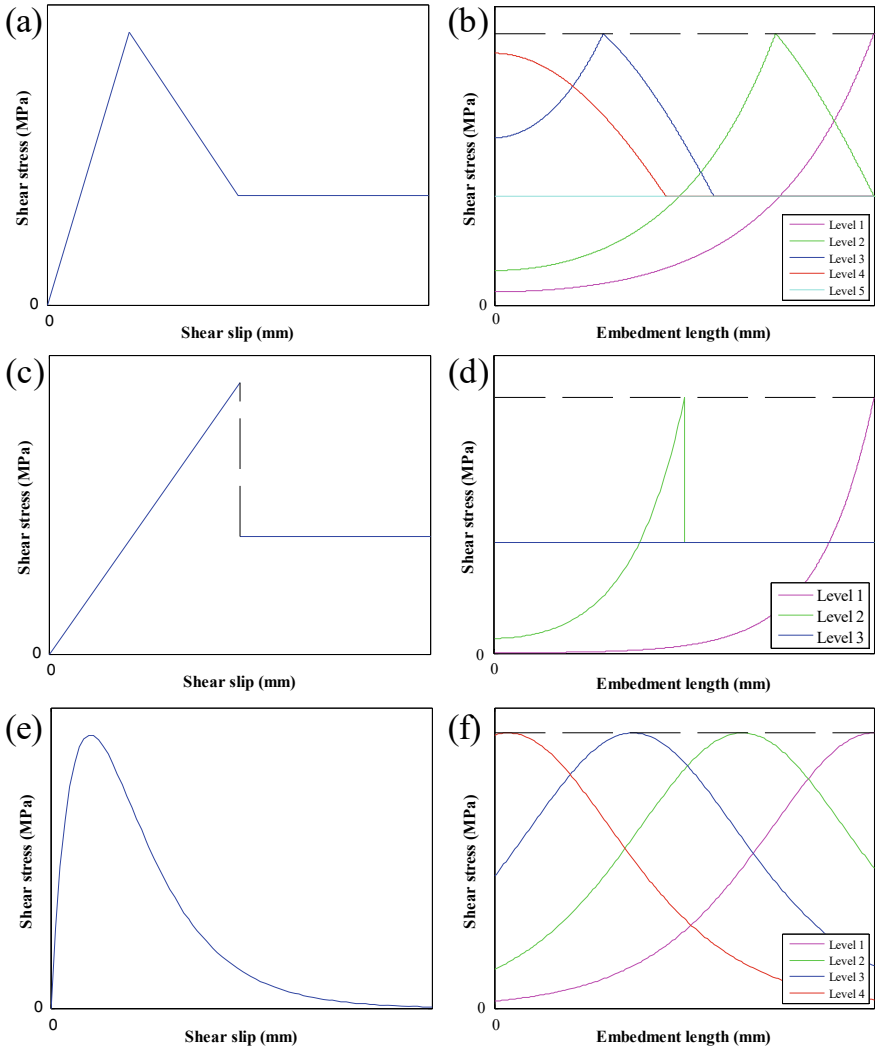

Fig. 2.2 Shear stress propagation process: **a** tri-linear equation; **b** corresponding shear stress propagation process; **c** bi-linear equation; **d** corresponding shear stress propagation process; **e** nonlinear equation; **f** corresponding shear stress propagation process

grout column and surrounding rock masses deform elastically. In fact, in experimental tests, failure of the rock masses may occur because of the radial dilation at the bolt/grout interface. Therefore, under this scenario, the analytical simulation which assumes that only slip failure occurs at the bolt/grout interface may not be trustable.

Similarly, in numerical simulation, rock masses are simulated with different elastoplastic equations. Among kinds of equations, the Mohr–Coulomb equation

is more commonly used. This equation is relatively simpler, and its input parameters can be acquired directly from experimental tests. However, it cannot properly simulate the post-failure behaviour of rock masses. Specifically, after the peak, the strain softening behaviour and residual behaviour of rock masses cannot be properly simulated. In this case, the interaction between the numerical rock mass and bolts cannot be the same as the reality. This is also the reason why the numerical simulation work should be calibrated and compared with experimental results.

Nevertheless, this is not to deny the significance of analytical simulation and numerical simulation. In fact, these two approaches are more powerful for researchers to understand the shear stress propagation mechanism of bolts. Therefore, it is suggested that combing the experimental tests, analytical simulation and numerical simulation is a better choice in studying the shear stress propagation mechanism of bolts.

2.4 Conclusions

This paper conducted a literature review on the shear stress propagation mechanism of rock reinforcement bolts. The previous investigation approaches were summarised. It is concluded that previous researchers usually used the experimental tests, analytical simulation and numerical simulation. Among those approaches, the experimental approach is more widely used. And the experimental test results are more likely to be accepted by others. By contrast, the analytical approach had more degree of freedom. With this approach, researchers can use different bond-slip equation to depict the slip behaviour of the bolt/grout interface. As for the numerical simulation, it is convenient for users since the original constitutive equation has already been created by the developer. Moreover, developers usually reserve the secondary development interface for users to modify the original constitutive equations.

As for the shear stress propagation mechanism, it is more commonly agreed that during the pull-out process of bolts, the shear stress at the borehole collar firstly increased. With the loading level increasing, the shear stress at the borehole collar gradually reaches the peak strength. Then, with the further increasing of the loading level, the maximum shear stress starts propagating towards the internal end. This phenomenon was consistently observed in experimental tests, analytical simulation and numerical simulation.

References

1. Z. Wang, T. Wang, S. Wu, Y. Hao, Investigation of microcracking behaviors in brittle rock using polygonal grain-based distinct method. Int. J. Numer. Anal. Meth. Geomech. **45**(13), 1871–1899 (2021). https://doi.org/10.1002/nag.3246

2. P.V. Nikolenko, S.A. Epshtein, V.L. Shkuratnik, P.S. Anufrenkova, Experimental study of coal fracture dynamics under the influence of cyclic freezing–thawing using shear elastic waves. Int. J. Coal Sci. Technol. **8**(4), 562–574 (2021). http://doi.org/10.1007/s40789-020-00352-x
3. H. Yang, M. Krause, J. Renner, Determination of fracture toughness of mode I fractures from three-point bending tests at elevated confining pressures. Rock Mech. Rock Eng. **54**(10), 5295–5317 (2021). https://doi.org/10.1007/s00603-021-02432-z
4. H. Gao, Q. Wang, B. Jiang, P. Zhang, Z. Jiang, Y. Wang, Relationship between rock uniaxial compressive strength and digital core drilling parameters and its forecast method. Int. J. Coal Sci. Technol. **8**(4), 605–613 (2021). https://doi.org/10.1007/s40789-020-00383-4
5. Z. Zhang, M. Deng, J. Bai, S. Yan, X. Yu, Stability control of gob-side entry retained under the gob with close distance coal seams. Int. J. Min. Sci. Technol. **31**(2), 321–332 (2021). https://doi.org/10.1016/j.ijmst.2020.11.002
6. J. Chen, P. Liu, L. Liu, B. Zeng, H. Zhao, C. Zhang, J. Zhang, D. Li, Anchorage performance of a modified cable anchor subjected to different joint opening conditions. Constr. Build. Mater. **336**, 1–12 (2022). https://doi.org/10.1016/j.conbuildmat.2022.127558
7. H. Yao, H. Wang, Y. Li, L. Jin, Three-dimensional spatial and temporal distributions of dust in roadway tunneling. Int. J. Coal Sci. Technol. **7**(1), 88–96 (2020). https://doi.org/10.1007/s40789-020-00302-7
8. S. Wu, H. Chen, F.L. Ramandi, P.C. Hagan, B. Hebblewhite, A. Crosky, S. Saydam, Investigation of cable bolts for stress corrosion cracking failure. Constr. Build. Mater. **187**, 1224–1231 (2018). https://doi.org/10.1016/j.conbuildmat.2018.08.066
9. Y. Chen, J. Teng, R.A. Bin Sadiq, K. Zhang, Experimental study of bolt-anchoring mechanism for bedded rock mass. Int. J. Geomech. **20**(4), 1–12 (2020). http://doi.org/10.1061/(ASCE)GM.1943-5622.0001561
10. C. Zhang, Y. Zhao, P. Han, Q. Bai, Coal pillar failure analysis and instability evaluation methods: a short review and prospect. Eng. Fail. Anal. **138**, 1–19 (2022). https://doi.org/10.1016/j.engfailanal.2022.106344
11. H. Yang, J. Renner, L. Brackmann, A. Roettger, Normal indentation of rock specimens with a blunt tool: role of specimen size and indenter geometry. Rock Mech. Rock Eng. **55**(4), 2027–2047 (2022). https://doi.org/10.1007/s00603-021-02732-4
12. Y. Chen, J. Zuo, D. Liu, Y. Li, Z. Wang, Experimental and numerical study of coal-rock bimaterial composite bodies under triaxial compression. Int. J. Coal Sci. Technol. 1–17 (2021). http://doi.org/10.1007/s40789-021-00409-5
13. Z. Zhang, M. Deng, J. Bai, X. Yu, Q. Wu, L. Jiang, Strain energy evolution and conversion under triaxial unloading confining pressure tests due to gob-side entry retained. Int. J. Rock Mech. Min. Sci. **126**, 1–10 (2020). https://doi.org/10.1016/j.ijrmms.2019.104184
14. S. Wang, Y. Wang, Z. Wang, J. Gong, C. Li, Anchoring performances analysis of tension-torsion grouted anchor under free and non-free rotating conditions. DYNA **96**(1), 166–172 (2021). https://doi.org/10.6036/9985
15. D. Li, H. Masoumi, C. Ming, A constitutive model for modified cable bolts exhibiting cone shaped failure mode. Int. J. Rock Mech. Min. Sci. **145**, 104855 (2021). https://doi.org/10.1016/j.ijrmms.2021.104855
16. J. Chang, K. He, D. Pang, D. Li, C. Li, B. Sun, Influence of anchorage length and pretension on the working resistance of rock bolt based on its tensile characteristics. Int. J. Coal Sci. Technol. **8**, 1384–1399 (2021). https://doi.org/10.1007/s40789-021-00459-9
17. A.G. Thompson, E. Villaescusa, C.R. Windsor, Ground support terminology and classification: an update. Geotech. Geol. Eng. **30**(3), 553–580 (2012). https://doi.org/10.1007/s10706-012-9495-4
18. S. Wang, Z.L. Wang, J. Gong, Y.H. Wang, Q.X. Huang, Coupling effect analysis of tension and reverse torque during axial tensile test of anchor cable. DYNA **95**(3), 288 (2020). https://doi.org/10.6036/9603
19. W. Marian, K. Krzysztof, N. Jacek, S. Marcin, B. Wioleta, An exsitu underground coal gasification experiment with a siderite interlayer: course of the process. Int. J. Coal Sci. Technol. **8**(6), 1447–1460 (2021). https://doi.org/10.1007/s40789-021-00456-y

20. J. Liu, H. Yang, H. Wen, X. Zhou, Analytical model for the load transmission law of rock bolt subjected to open and sliding joint displacements. Int. J. Rock Mech. Min. Sci. **100**, 1–9 (2017). https://doi.org/10.1016/j.ijrmms.2017.01.018
21. D. Li, Y. Li, J. Chen, H. Masoumi, An analytical model for axial performance of rock bolts under constant confining pressure based on continuously yielding criterion. Tunn. Undergr. Space Technol. **113**, 1–9 (2021). https://doi.org/10.1016/j.tust.2021.103955
22. S. Wang, H.G. Xiao, Z.S. Zou, C. Cao, Y.H. Wang, Z.L. Wang, Mechanical performances of transverse rib bar during pull-out test. Int. J. Appl. Mech. **11**(5), 1–15 (2019). https://doi.org/10.1142/S1758825119500480
23. J. Chen, P.C. Hagan, S. Saydam, An experimental study of the specimen geometry effect on the axial performance of cement-based grouts. Constr. Build. Mater. **310**, 125167 (2021). https://doi.org/10.1016/j.conbuildmat.2021.125167
24. H. Yu, H. Jia, S. Liu, Z. Liu, B. Li, Macro and micro grouting process and the influence mechanism of cracks in soft coal seam. Int. J. Coal Sci. Technol. **8**, 969–982 (2021). https://doi.org/10.1007/s40789-020-00404-2
25. T. Aoki, K. Shibata, F. Nakahara, Y. Maeno, R. Kawano, Y. Obara, Pull tests of long-embedded cablebolts, in *ISRM 2003—Technology Roadmap for Rock Mechanics*. South African National Institute of Rock Engineering and South African Institute of Mining and Metallurgy, Gauteng, South Africa (2003), pp. 45–48
26. S. Wang, Y.H. Wang, J. Gong, Z.L. Wang, Q.X. Huang, F.L. Kong, Failure mechanism and constitutive relation for an anchorage segment of an anchor cable under pull-out loading. Acta Mech. **231**(8), 3305–3317 (2020). https://doi.org/10.1007/s00707-020-02717-4
27. M. Chekired, B. Benmokrane, H.S. Mitri, Laboratory evaluation of a new cable bolt tension measuring device. Int. J. Rock Mech. Min. Sci. **34**(3–4), 1–13 (1997). https://doi.org/10.1016/S1365-1609(97)00076-2
28. L. Martin, R. Pakalnis, D. Milne, Determination of physical properties of cable bolts in cement grout pull tests using instrumented king wires. National Institute for Occupational Safety and Health, Spokane (2008), pp. 1–8
29. J. Chen, Y. Zhao, H. Zhao, J. Zhang, C. Zhang, D. Li, Analytic study on the force transfer of full encapsulating rockbolts subjected to tensile force. Int. J. Appl. Mech. **13**(9), 1–13 (2021). https://doi.org/10.1142/S1758825121500976
30. H. Ma, X. Tan, J. Qian, X. Hou, Theoretical analysis of anchorage mechanism for rock bolt including local stripping bolt. Int. J. Rock Mech. Min. Sci. **122**, 1–6 (2019). https://doi.org/10.1016/j.ijrmms.2019.104080
31. J. Zou, P. Zhang, Analytical model of fully grouted bolts in pull-out tests and in situ rock masses. Int. J. Rock Mech. Min. Sci. **113**, 278–294 (2019). https://doi.org/10.1016/j.ijrmms.2018.11.015
32. W. Zhang, L. Huang, C.H. Juang, An analytical model for estimating the force and displacement of fully grouted rock bolts. Comput. Geotech. **117**, 1–10 (2020). https://doi.org/10.1016/j.compgeo.2019.103222
33. I.W. Farmer, Stress distribution along a resin grouted rock anchor. Int. J. Numer. Anal. Meth. Geomech. **12**, 347–351 (1975). https://doi.org/10.1016/0148-9062(75)90168-0
34. S. Zhu, C. Chen, F. Mao, H. Cai, Application of disturbed state concept for load-transfer modeling of recoverable anchors in layer soils. Comput. Geotech. **137**, 1–16 (2021). https://doi.org/10.1016/j.compgeo.2021.104292
35. O. Aydan, Y. Ichikawa, K. Kawamoto, Load bearing capacity and stress distributions in/along rockbolts with inelastic behaviour of interfaces, in *Fifth International Conference on Numerical Methods in Geomechanics*, Nagoya, Japan, (1985), pp. 1281–1292
36. Y. Cai, T. Esaki, Y. Jiang, A rock bolt and rock mass interaction model. Int. J. Rock Mech. Min. Sci. **41**, 1055–1067 (2004). https://doi.org/10.1016/j.ijrmms.2004.04.005
37. K. Mohamed, G. Rashed, Z. Radakovic-Guzina, Loading characteristics of mechanical rib bolts determined through testing and numerical modelling. Int. J. Min. Sci. Technol. **30**, 17–24 (2020). https://doi.org/10.1016/j.ijmst.2019.12.016

38. J. Nemcik, S. Ma, N. Aziz, T. Ren, X. Geng, Numerical modelling of failure propagation in fully grouted rock bolts subjected to tensile load. Int. J. Rock Mech. Min. Sci. **71**, 293–300 (2014). https://doi.org/10.1016/j.ijrmms.2014.07.007
39. J. Chen, H. Zhao, F. He, J. Zhang, K. Tao, Studying the performance of fully encapsulated rock bolts with modified structural elements. Int. J. Coal Sci. Technol. **8**(1), 64–76 (2021). https://doi.org/10.1007/s40789-020-00388-z
40. J. Chen, D. Li, Numerical simulation of fully encapsulated rock bolts with a tri-linear constitutive relation. Tunn. Undergr. Space Technol. **120**, 1–13 (2022). https://doi.org/10.1016/j.tust.2021.104265
41. J. Shang, Y. Yokota, Z. Zhao, W. Dang, DEM simulation of mortar-bolt interface behaviour subjected to shearing. Constr. Build. Mater. **185**(120–137) (2018). http://doi.org/10.1016/j.conbuildmat.2018.07.044
42. L. Blanco Martín, M. Tijani, F. Hadj-Hassen, A new analytical solution to the mechanical behaviour of fully grouted rockbolts subjected to pull-out tests. Constr. Build. Mater. **25**(2), 1–18 (2010). http://doi.org/10.1016/j.conbuildmat.2010.07.011
43. B. Benmokrane, A. Chennouf, H.S. Mitri, Laboratory evaluation of cement-based grouts and grouted rock anchors. Int. J. Rock Mech. Min. Sci. **32**(7), 633–642 (1995). https://doi.org/10.1016/0148-9062(95)00021-8
44. S. Ma, J. Nemcik, N. Aziz, An analytical model of fully grouted rock bolts subjected to tensile load. Constr. Build. Mater. **49**, 519–526 (2013). https://doi.org/10.1016/j.conbuildmat.2013.08.084
45. C. Cao, J. Nemcik, T. Ren, N. Aziz, A study of rock bolting failure modes. Int. J. Min. Sci. Technol. **23**(1), 79–88 (2013). https://doi.org/10.1016/j.ijmst.2013.01.012
46. A. Teymen, A. Kilic, Effect of grout strength on the stress distribution (tensile) of fully-grouted rockbolts. Tunn. Undergr. Space Technol. **77**, 280–287 (2018). https://doi.org/10.1016/j.tust.2018.04.022
47. G. Rong, H. Zhu, C. Zhou, Testing study on working mechanism of fully grouted bolts of thread steel and smooth steel. Chin. J. Rock Mech. Eng. **23**(3), 469–475 (2004) (in Chinese)
48. F. Ren, Z.J. Yang, J.F. Chen, W.W. Chen, An analytical analysis of the full-range behaviour of grouted rockbolts based on a tri-linear bond-slip model. Constr. Build. Mater. **24**(3), 361–370 (2010). https://doi.org/10.1016/j.conbuildmat.2009.08.021
49. L. Blanco Martín, M. Tijani, F. Hadj-Hassen, A. Noiret, Assessment of the bolt-grout interface behaviour of fully grouted rockbolts from laboratory experiments under axial loads. Int. J. Rock Mech. Min. Sci. **63**, 50–61 (2013). http://doi.org/10.1016/j.ijrmms.2013.06.007
50. J. Chen, P. Liu, H. Zhao, C. Zhang, J. Zhang, Analytical studying the axial performance of fully encapsulated rock bolts. Eng. Fail. Anal. **128**, 1–16 (2021). https://doi.org/10.1016/j.engfailanal.2021.105580
51. W. Nie, Z. Zhao, S. Ma, W. Guo, Effects of joints on the reinforced rock units of fully-grouted rockbolts. Tunn. Undergr. Space Technol. **71**, 15–26 (2018). https://doi.org/10.1016/j.tust.2017.07.005
52. S. Wu, H.L. Ramandi, H. Chen, A. Crosky, P.C. Hagan, S. Saydam, Mineralogically influenced stress corrosion cracking of rockbolts and cable bolts in underground mines. Int. J. Rock Mech. Min. Sci. **119**, 109–116 (2019). https://doi.org/10.1016/j.ijrmms.2019.04.011
53. D.-A. Ho, M. Bost, J.-P. Rajot, Numerical study of the bolt-grout interface for fully grouted rockbolt under different confining conditions. Int. J. Rock Mech. Min. Sci. **119**, 168–179 (2019). https://doi.org/10.1016/j.ijrmms.2019.04.017
54. J. Zuo, J. Wen, Y. Li, Y. Sun, J. Wang, Y. Jiang, L. Liu, Investigation on the interaction mechanism and failure behaviour between bolt and rock-like mass. Tunn. Undergr. Space Technol. **93**, 103070 (2019). https://doi.org/10.1016/j.tust.2019.103070
55. Y. Yokota, Z. Zhao, W. Nie, K. Date, K. Iwano, Y. Okada, Experimental and numerical study on the interface behaviour between the rock bolt and the bond material. Rock Mech. Rock Eng. **52**, 869–879 (2019). http://doi.org/10.1007/s00603-018-1629-4

Chapter 3
Numerical Simulation of the Shear Behaviour of Cement Grout

3.1 Introduction

Cement is grey fine powder that is widely used in civil engineering and mining engineering [1, 2]. In civil engineering, as an important ingredient, cement is always mixed with water, sand and rocks to form concrete, which is the commonly used construction or building material [3, 4]. In mining engineering, cement is usually mixed with water to form the cement grout, which is then poured into drilled boreholes to bond the reinforcing tendon, such as rock bolts and cable bolts, with the surrounding rock masses [5]. Moreover, the cement can be used as the grouting material to be poured into rock mass to improve its mechanical behaviour.

The mechanical properties of the cement grout have a significant effect in deciding the performance of the rock reinforcement systems [6]. Consequently, a vast of research has been conducted to study the mechanical behaviour of the cement grout [7]. Those studies can be basically divided into studying the axial behaviour of the cement grout and shear behaviour of the cement grout.

To study the axial behaviour of the cement grout, researchers mainly used the Uniaxial Compressive Strength (UCS) tests. Feldman and Beaudoin [8] indicated that the strength and elastic modulus of the Portland cement grout were largely influenced by the porosity. Domone and Thurairatnam [9] found that with the *w/c* ratio decreasing, the strength of the cement grout increased. Hyett et al. [10] evaluated the influence of curing time on the grout strength and found that the grout UCS increased nonlinearly with the hydration time ranging from 1 to 7 days. Boumiz et al. [11] adopted the ultrasonic and calorimetric methods on cement grout. They found that the larger the hydration degree, the higher the elastic modulus of the cement grout. Li et al. [12] studied the influence of nanoparticles on the performance of cement grout. They proved that adding nanoparticles was beneficial for improving the grout strength. Mirza et al. [13] revealed that the grout strength increased within the curing period, independent of the cement type.

J. Chen et al., *Bond Failure Mechanism of Fully Grouted Rock Bolts*,
SpringerBriefs in Applied Sciences and Technology,
https://doi.org/10.1007/978-981-99-0498-3_3

The above research played an important role in revealing the mechanical performance of cement grout. However, experimental tests proved that in the fully grouted rock reinforcing system, failure of the system usually occurred at the bolt/grout interface [14]. This was resulted by the low shear strength of the interface [15]. The shear behaviour of the cement grout has a significant role in determining the shear strength of the bolt/grout interface [16]. Therefore, better understanding the shear behaviour of the cement grout was beneficial for preventing failure of the bolt/grout interface.

To study the shear behaviour of cement grout, researchers commonly used tri-axial tests and direct shear tests. For tri-axial tests, Hyett et al. [17] studied the performance of Portland cement grout with the confining pressure ranging from 5 to 15 MPa. The results showed that the larger the confining pressure, the higher the strength of the cement grout. Moreover, the cohesion and the internal friction angle were successfully acquired. Simms and Grabinsky [18] performed tri-axial tests on cement material under the confined condition. The results showed that in the shearing process, the cementitious material had an apparent tendency to dilate. Sakai et al. [19] studied the performance of the cement paste under the tri-axial condition. The results proved that increasing the confining pressure changed the sample failure mode. Specifically, when the confining pressure was 30 MPa, oblique shear failure plane occurred in the sample. However, once the confining pressure was much larger, horizontal failure plane occurred in the sample. Aziz et al. [20] conducted tri-axial tests on two types of cement grout and used Mohr–Coulomb (MC) model to fit the shear strength envelope. A vast of tri-axial tests were conducted by Chen and Xu [21] to study the performance of the cement grout under the high confining pressure condition. It was found that with the confining pressure increasing, the performance of the cement grout changed from brittle to ductile. Moreover, this phenomenon was valid independent of the *w*/*c* ratio. Those tri-axial testing research improved the understanding in the shear behaviour of cement grout. However, in tri-axial tests, the shear failure plane occurred dependent on the properties of the grout and the loading status [22]. This was not a true reflection of the shear failure of the bolt/grout interface in the rock reinforcing system, where the shear failure plane was a pre-defined plane [23, 24].

Therefore, the direct shear test was a better approach to study the shear behaviour of the cement grout for the rock reinforcement scenario. The direct shear test is a traditional method to evaluate the shear strength of a material. Normally, a shear box is prepared. Then, the tested sample is cut to the desired geometry with the required dimension. After that, the sample was set in the shear box and installed in the apparatus. Operators can apply normal stress on the sample and then apply shear velocity along the shear direction. This test is continued until the shear strength was obtained. In this way, the shear strength of the material can be acquired. Moosavi and Bawden [25] designed a shear box to conduct direct shear tests on Portland cement grout. The results showed that the direct shear test was likely to provide a smaller shear strength of the cement grout, when compared with tri-axial tests. Lu and Wang [26] performed direct shear tests on cementitious samples with two different *w*/*c* ratios: 0.3 and 0.4. They found that when the *w*/*c* ratio was 0.3, shear strength of the cement-based sample increased apparently with normal stress. However, when

the *w*/*c* ratio was 0.4, shear strength of the cement-based sample did not increase much with the normal stress. Assaad et al. [27] proposed using the direct shear test to study the yield stress of cement material. The results revealed that the material shear strength was largely dependent on the normal stress, following the MC rule. Chen et al. [28] compared the shear performance of a Portland cement grout under the constant normal load and constant normal stiffness condition. It was found that the boundary condition might influence the performance of the cement grout. Li et al. [29] adopted the direct shear tests to investigate the influence of particle size on the shear strength of cement grout. They found that through adding superfine cement, the early-age shear strength parameters of the cement grout can be largely enhanced.

That research provided new insights and knowledge in revealing the shear performance of cement grout. However, most research was conducted with experimental tests. Compared with that, much less work has been performed via numerical simulation. Therefore, this study aims at studying the shear behaviour of the cement grout with numerical simulation.

First, a numerical calculating programme was selected to conduct this research. After that, numerical direct shear tests were performed to evaluate the shear behaviour of the cement grout. Then, the numerical calculating results were validated with experimental results. Last, the shear stress distribution on the shear failure plane was investigated.

3.2 Selection of the Software

In this study, the three-dimensional software FLAC3D was used. This programme was developed by the Itasca Consulting Group.

The reason to use this programme is that the Itasca Company developed the interface element in it. This interface element is composed of triangular elements and corresponding nodes. Moreover, the interface element is defined with the shear coupling constitutive model. In this case, once shear displacement occurs in the interface element, shear stress at the interface accumulates and can be calculated. Relied on this function, the shear behaviour of a material can be studied.

The authors of this study previously used the two-dimensional software FLAC to simulate the shear failure process of the bolt/grout interface [30]. However, the drawback was that the problem was simplified to be two dimensional. Compared with FLAC, the advantage of FLAC3D was that it can simulate objects in three dimensions. Therefore, it can better reflect the mechanical behaviour of objects. Then, in this study, the FLAC3D was used to simulate the shearing process of the cement grout.

3.3 Numerical Simulation Process

A vast of direct shear tests were performed by Moosavi and Bawden [25]. Those tests were used in this study and simulated with FLAC3D. In their study, two different *w*/*c* ratios were used, namely 0.4 and 0.5. Then, in the following section, numerical tests on those two cement grouts were performed.

3.3.1 Simulation of the Cement Grout with a Higher Strength

3.3.1.1 Numerical UCS Test and Validation

Before the direct shear test was conducted, UCS tests were performed to acquire the basic mechanical properties of the grout, including the UCS, elastic modulus and the Poisson's ratio. Detailed information about the UCS test process and results were reported by Moosavi [24]. Experimental results showed that for the cement grout with a *w*/*c* ratio of 0.4, the UCS, elastic modulus and Poisson's ratio were 50.6 MPa, 12.66 GPa and 0.25. More specifically, in the UCS test, the cement grout was filled in PVC tubes with the diameter of 50 mm and the length of 150 mm.

In numerical simulation in FLAC3D, the *w*/*c* ratio cannot be directly simulated. As a compromise, the UCS of the numerical mesh was selected as the index to compare with the experimental result. In FLAC3D, a numerical UCS test was created (Fig. 3.1).

In the numerical UCS test, a cylindrical mesh was established. At the top and bottom of the cylinder, two square steel plates were established to simulate the loading plates. The whole mesh was composed of 16,032 zones and 16,531 grid points. For the numerical plate, there were 32 zones and 100 grid points. For the numerical sample, there were 16,000 zones and 16,441 grid points.

A strain softening model was used for the cylindrical sample. It was developed based on the MC model. Compared with the MC model, the strain softening model had additional input parameters: the cohesion table and the internal friction angle table. With those two parameters, the cohesion and internal friction angle of the materials can decrease with the increasing plastic shear strain. Therefore, this model can simulate the post-peak behaviour of materials.

The reason to use this strain softening model was that this model can simulate the post-peak behaviour of materials. Therefore, it is better in reflecting the mechanical behaviour of materials.

An elastic model was used for the square plates. The reason to use the elastic model to simulate the square plate was that in the experimental compressive test, the cement-based sample was compressed by the steel plate, since the strength of the steel plate was much higher than the cement-based sample. Failure only occurred in the cement-based sample. The steel plate consistently kept the elastic state. The input parameters for the cylindrical sample and the square plates are tabulated in Table 3.1.

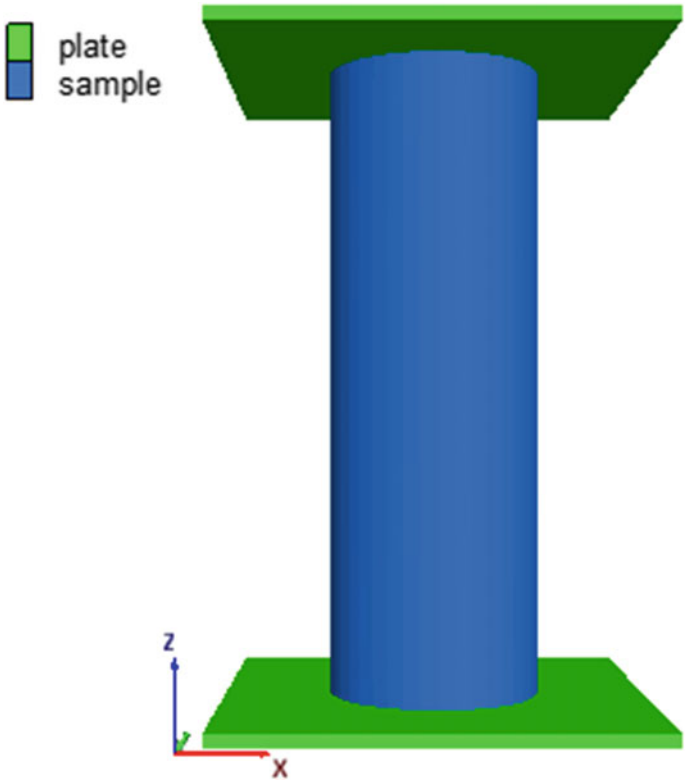

Fig. 3.1 Geometry of the UCS test created in numerical simulation

Table 3.1 Input parameters for the sample and the plate

Group	Input parameter	Value
Sample	Bulk modulus (GPa)	8.44
	Shear modulus (GPa)	5.06
	Cohesion (MPa)	19.3
	Internal friction angle (°)	21
	Tension (MPa)	2
Plate	Bulk modulus (GPa)	133.33
	Shear modulus (GPa)	80

The velocity of the plates was fixed. Moreover, the initial velocity of the top plate along the z-axis was set as $-1e{-}7$ m per step (minus represented that the velocity was along the negative direction of the z-axis). Since the velocity of the plate was fixed during the simulation process, the top plate would decline with a constant velocity. Additionally, no velocity was applied on the bottom plate. Consequently, the bottom

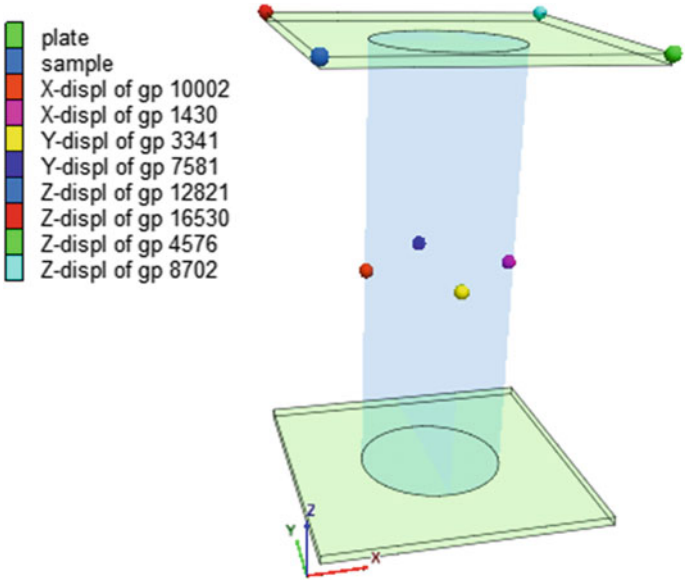

Fig. 3.2 Grid points monitored in the simulation process

plate would be stable in the whole simulation process. With this method, the sample in the middle would be compressed by the top plate to simulate the UCS process.

In the simulation process, the displacement along the z-axis of four grid points in the top plate was monitored (Fig. 3.2).

Those four displacements were averaged as the uniaxial displacement of the sample, as shown in Eq. (3.1).

$$s_{\mathrm{a}} = \frac{s_{\mathrm{a1}} + s_{\mathrm{a2}} + s_{\mathrm{a3}} + s_{\mathrm{a4}}}{4} \tag{3.1}$$

where s_{a}: the axial displacement; and $s_{\mathrm{a}i}$: the axial displacement of the grid point i in the top plate.

In UCS test, to calculate the Poisson's ratio, the circumferential strain gauge was usually attached at the middle of the sample, to record the circumferential displacement of the sample. Then, in this simulation, the circumferential displacement of four grid points at the middle of the outside surface of the sample was monitored. Those four displacements were also averaged as the circumferential displacement of the sample, as shown in Eq. (3.2).

$$s_{\mathrm{c}} = \frac{s_{\mathrm{c1}} + s_{\mathrm{c2}} + s_{\mathrm{c3}} + s_{\mathrm{c4}}}{4} \tag{3.2}$$

where s_{c}: the circumferential displacement of the sample; $s_{\mathrm{c}i}$: the circumferential displacement of the grid point i at the middle of outside surface of the sample.

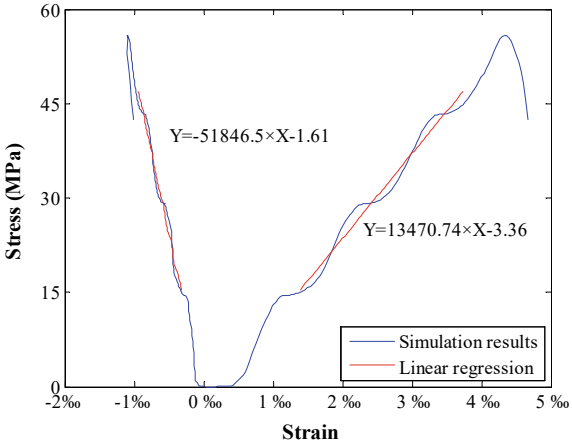

Fig. 3.3 Stress-to-strain relationship of the cement grout sample

Since the bottom plate was stabilised in the whole simulation process, the reaction force along the z-axis of the grid points at the bottom surface of bottom plate was summed. Then, this summed force was divided by the cross-section area of the sample, and the result was regarded as the uniaxial compressive stress of the sample.

Then, the numerical UCS test was conducted. The stress-to-strain relationship of the sample is shown in Fig. 3.3. In the numerical simulation, the UCS of the sample was 55.87 MPa.

In the experimental test, the UCS of the cement grout sample was 50.6 MPa, which was consistent with the numerical simulation results.

It also shows that in numerical simulation, after the stress of the sample reached the peak, the circumferential strain decreased. To check the reason, the circumferential displacement of a grid point was taken as an example and plotted. The grid point at the right middle of the sample (with an ID of 1430) was selected. The circumferential displacement of the grid point with the calculating time step is shown in Fig. 3.4. The results show that before the calculating time step reached 6650, the circumferential displacement of the grid point increased. This indicated that the diameter of the sample at the middle increased because of the compression. However, after the calculating time step reached 6650, the circumferential displacement of the grid point started decreasing. This indicated that after the sample reached the peak strength, the diameter of the sample in the middle also reached the peak. After the sample failed, the diameter of the sample in the middle started decreasing. This explained the phenomenon that after the sample reached the peak strength, the circumferential strain started decreasing.

Based on the numerical simulation, the elastic modulus and the Poisson's ratio can also be acquired. The results showed that the elastic modulus in numerical simulation was 13.47 GPa. The Poisson's ratio can be calculated with Eq. (3.3) [31]:

$$\mu = -\frac{\varepsilon_c}{\varepsilon_a} \tag{3.3}$$

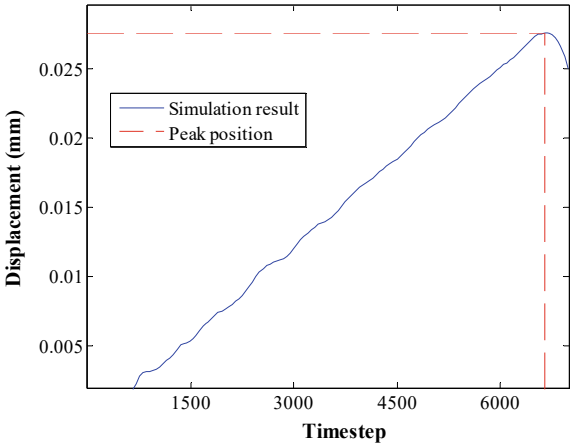

Fig. 3.4 Circumferential displacement of the grid point at the right middle of the sample

Table 3.2 Comparison between the mechanical properties of the cement grout acquired from laboratory tests conducted by Moosavi [24] and calculated from numerical simulation

Properties	Laboratory test	Numerical simulation
UCS	50.6	55.87
Elastic modulus (GPa)	12.66	13.47
Poisson's ratio	0.25	0.26

where μ: Poisson's ratio; ε_c: the circumferential strain of the sample; and ε_a: the axial strain of the sample.

Then, the Poisson's ratio can be calculated as 0.26. Comparing the elastic modulus and Poisson's ratio acquired from numerical simulation with those acquired from experimental tests, there was a close match between them, as shown in Table 3.2. This further confirmed that the input mechanical parameters were capable for simulating the cement grout.

3.3.1.2 Numerical Direct Shear Test and Validation

The input mechanical parameters used in the UCS simulation were then used in this section to simulate the direct shear process. Moosavi and Bawden [25] conducted experimental direct shear tests on cylindrical samples with a diameter of 100 mm and length of 200 mm. The test process was simulated in this section, and the simulation result was then validated with experimental results.

In FLAC3D, a numerical cylindrical sample whose dimension was same as the experimental sample was established. The sample was composed of two sections, namely the top section and the bottom section. In the whole numerical model, there were 18,000 zones and 19,232 grid points. It should be mentioned that in the direct shear test, the shear failure plane is a pre-defined plane. Consequently, in numerical

Table 3.3 Input parameters for the interface

Group	Input parameter	Value
Interface	Normal stiffness (GPa/m)	40
	Shear stiffness (GPa/m)	8.28
	Cohesion (MPa)	5.3
	Friction angle (°)	30

simulation, an interface was created at the middle of the sample, namely between the top section and the bottom section, to simulate the shear failure plane. The interface was composed of 49,128 elements and 24,725 nodes.

The constitutive model of the created interface was MC model, and the input parameters of the interface are tabulated in Table 3.3.

The top section was fixed along the *x*-axis. For the bottom section, the external surface was fixed along the *x*-axis and *y*-axis. This was to simulate that in the experimental test, the bottom sample was restricted by the shear box and no movement could occur. As for the bottom surface of the sample, it was fully fixed to simulate that in the experiment, the whole sample was supported with a plate. A compressive normal stress of 2 MPa was applied on the top surface of the sample. Then, this numerical model was calculated until the unbalanced force ratio decreased to 1e−5. With this method, the initial normal stress equilibrium condition was acquired. The normal stress distribution in the sample is shown in Fig. 3.5. It is apparent to see that there was basically a uniform normal stress distribution in the sample. Under compression of the normal stress of 2 MPa, the normal stress in the sample was around 2 MPa.

Before the direct shear test was performed, the displacement along the shearing direction of four grid points at the top surface of the sample was monitored. In the simulation process, the displacements of those four grid points were averaged as the shear displacement of the sample.

It is more important to monitor the shear stress in the direct shear test process. To acquire this, in each step in the direct shear test process, each node on the interface was checked whether that node was still contact. If it was, the shear force of that node was recorded and summed. The accumulated shear force was the whole shear force of the interface and was then divided by the area of the interface. The result was regarded as the shear stress of the interface.

Then, the direct shear test was performed. A shearing velocity of 1e−6 m per step was applied on the top section of the sample. This velocity was kept constant in the whole simulation process, to simulate the servo control. The direct shear test was conducted until the sample failed.

The comparison between the numerical simulation result and the experimental test result is shown in Fig. 3.6. In numerical simulation, when the shear displacement increased to 0.94 mm, the shear stress of the interface increased to the peak of 6.48 MPa. After that, the shear stress decreased gradually. Also, there was a close match between numerical and experimental results. This confirmed that numerical simulation was capable in simulating the shear behaviour of the cement grout.

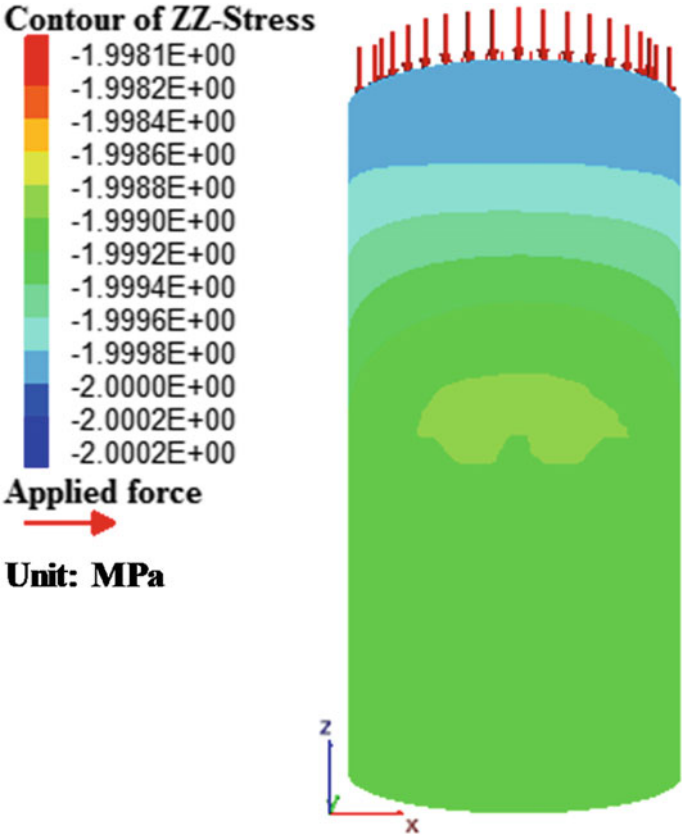

Fig. 3.5 Normal stress distribution in the sample

It should be mentioned that this comparison was compared with the final shear displacement being less than 2 mm.

In the shearing process, the averaged normal stress of the interface was also monitored. The variation of the normal stress on the interface is shown in Fig. 3.7. Before the shear displacement increased to 0.94 mm, the normal stress of the interface increased slightly to the peak of 2.15 MPa. After that, the normal stress of the interface decreased gradually. However, in the whole process, the minimum normal stress of the interface was 1.99 MPa, which was only a little bit smaller than the maximum normal stress of the interface. This indicated that in the direct shear process, the normal stress of the interface was not constant although the applied normal stress was constant. This was probably due to the separation between the top sample and the bottom sample, and the frictional failure of the interface.

After the direct shear test, a plot of the normal stress distribution on the interface is shown in Fig. 3.8.

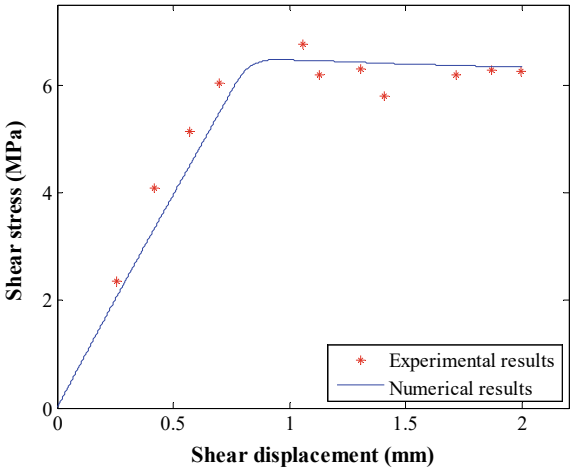

Fig. 3.6 Comparison between numerical simulation result and the experimental test conducted by Moosavi and Bawden [25]

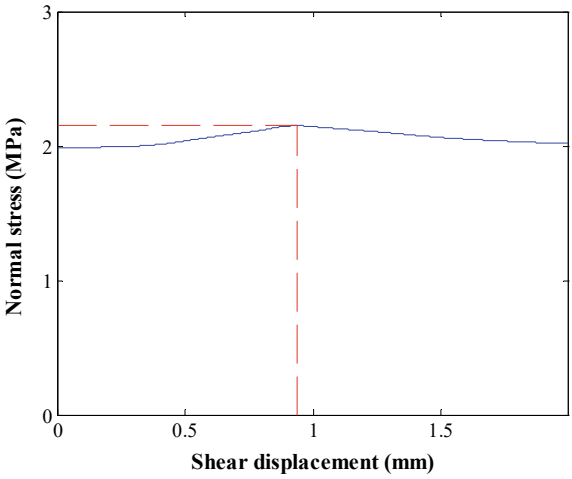

Fig. 3.7 Variation of the normal stress of the shear failure plane

The results showed that the normal stress at the left side of the interface was zero. This was due to the separation of the top and bottom samples. Consequently, the interface was non-contact around the left side, as shown in Fig. 3.9.

Since it is more important to study the state of the interface that was contact, the stresses on the contacted interface were further studied. At the left side of the contacted interface, the normal stress was apparently much higher, with a maximum normal stress of 3.56 MPa. Moreover, the normal stress on the interface decreased towards the shearing direction. At the right side, the normal stress was much lower, with a minimum normal stress around 0.75 MPa.

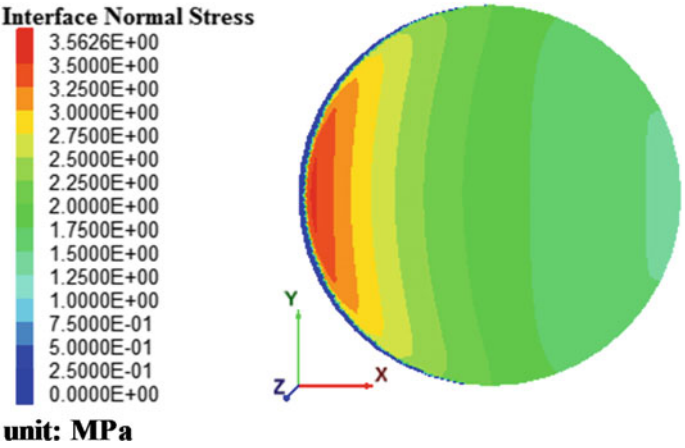

Fig. 3.8 Normal stress distribution on the shear failure plane

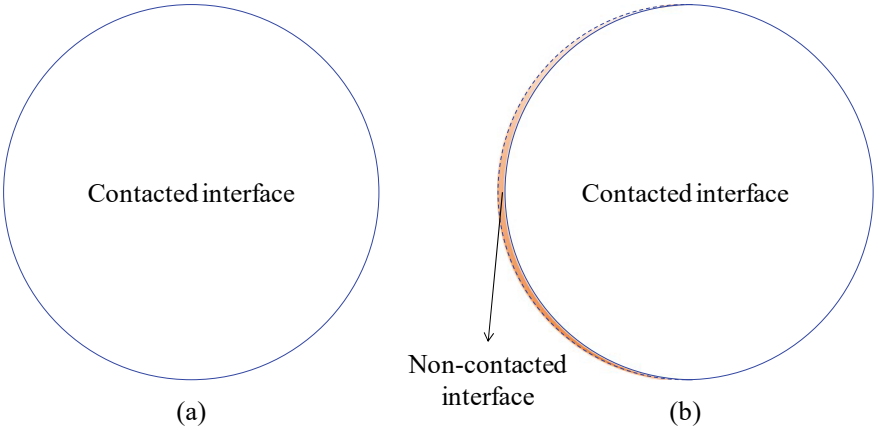

Fig. 3.9 State of the interface in the direct shear test: **a** before the direct shear test; **b** after the direct shear test

As for the shear stresses on the interface, its distribution is shown in Fig. 3.10. Around the left side of the whole interface, the shear stress was also zero, due to the non-contact of the interface.

As for the contacted interface, the shear stress distribution was apparently not uniform. At the left side of the contacted interface, the shear stress was much higher, with a maximum of 7.36 MPa. Then, the shear stress decreased towards the shearing direction. At the right side, the shear stress was relatively lower, with a minimum around 6.0 MPa. This trend was basically consistent with the distribution of the normal stress on the interface.

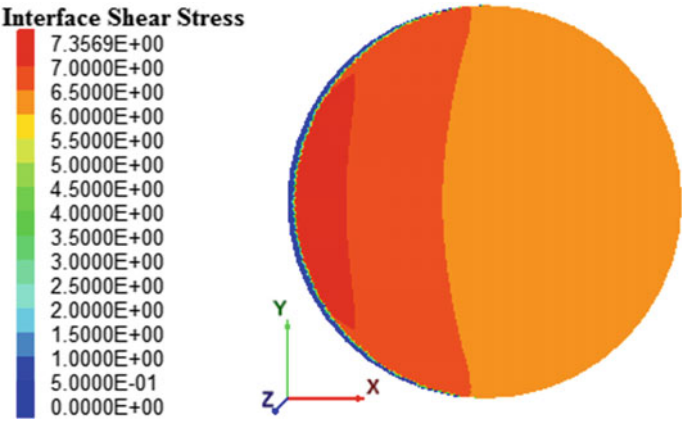

Fig. 3.10 Shear stress distribution on the shear failure plane

However, attention should be paid that Figs. 3.8 and 3.10 depicted the interface stress state after the test. In the middle shearing process, whether the distribution state was consistent with them was uncertain. And this will be studied in the following section.

After the direct shear test, the plastic state of the sample is shown in Fig. 3.11. In this figure, "tension-n" means that the zone was experiencing tensile failure now. "tension-p" means that the zone previously experienced tensile failure. It is apparent to see that at the left side of the bottom sample, tensile failure occurred in the sample. Specifically, in the bottom sample, tensile failure occurred around the left side. In fact, this was consistent with the laboratory experimental test. Moosavi and Bawden [25] indicated that in the experimental test, tension crack occurred in the cement grout sample around the shear failure plane.

3.3.2 Simulation of the Cement Grout with a Lower Strength

Numerical simulation was also conducted on the same cement grout type while with a relative lower strength. First, the numerical UCS test was performed and compared with the experimental result, to confirm the proper input parameters.

3.3.2.1 Numerical UCS Test and Validation

The UCS test was simulated in FLAC3D. The simulation process was generally consistent with the procedures described above. Therefore, detailed simulation procedures were not described here. Only the simulation results were presented.

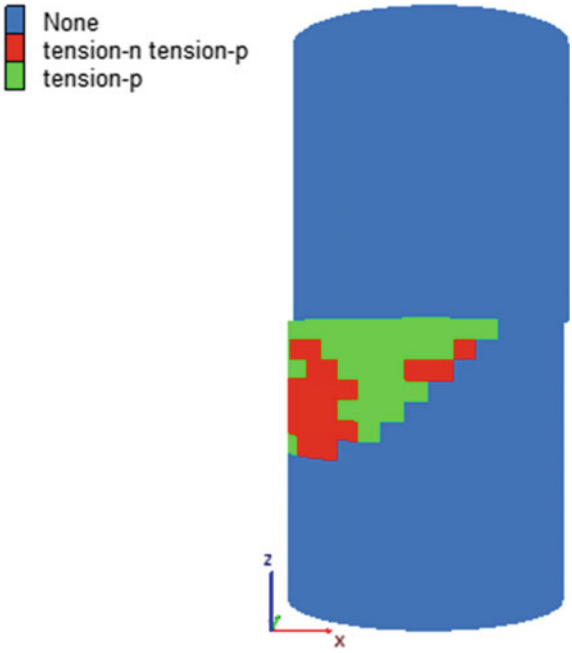

Fig. 3.11 Plastic zone distribution in the sample

Table 3.4 Comparison between the experimental result reported by Moosavi [24] and calculated from numerical simulation

Properties	Laboratory test	Numerical simulation
UCS	40.3	46.09
Elastic modulus (GPa)	8.571	8.33
Poisson's ratio	0.25	0.26

After the simulation, the stress-to-strain relationship of the sample was obtained. When the axial strain increased to 0.53%, the axial stress of the sample reached the peak of 46.09 MPa. In experimental test, the measured UCS was 40.3 MPa. Therefore, there was a close match between them.

The elastic modulus and Poisson's ratio were also obtained. In numerical simulation, the elastic modulus and Poisson's ratio of the cement grout sample were 8.33 GPa and 0.26. A comparison between experimental and numerical results is shown in Table 3.4. There was a good correlation between them. This further confirmed that the input parameters were robust for simulating the cement grout and can be used in the following direct shear test.

3.3.2.2 Numerical Direct Shear Test and Validation

Then, the numerical direct shear test was performed. And the input parameters of the sample were same as those used in the UCS simulation. A comparison between the

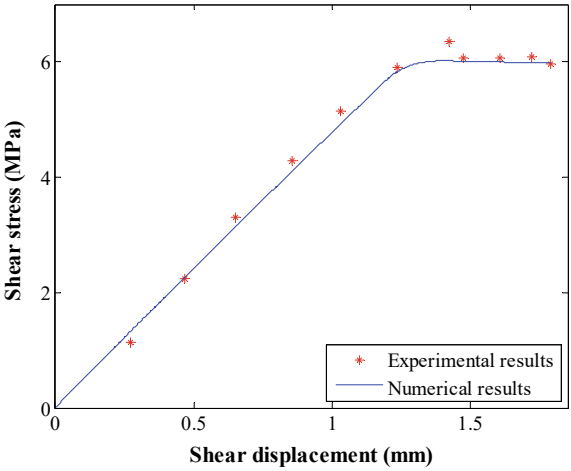

Fig. 3.12 Comparison between the experimental result reported by Moosavi and Bawden [25] and the numerical simulation result

experimental and the numerical results is shown in Fig. 3.12. In numerical simulation, when the shear displacement increased to 1.41 mm, the shear stress of the interface reached the peak, which was 6.02 MPa. Following this, the shear stress reduced gradually with the shear displacement. The results also showed that there was a good correlation between experimental and numerical results. This further confirmed the effectiveness of numerical simulation in evaluating the shear behaviour of the cement grout. Attention was paid that in this comparison, the maximum shear displacement was less than 1.8 mm.

Also, the variation of the normal stress on the shear failure plane was checked. In the simulation process, the normal stress on the shear failure plane was not constant. It had a slight increasing trend at the beginning and then decreased gradually.

3.4 Analysis on the Shear Stress Distribution

Figures 3.8 and 3.10 showed that after the direct shear test, the normal stress and shear stress distribution on the shear failure plane were not uniform. However, in the middle process of the direct shear test, the normal stress and shear stress distribution state were uncertain. Therefore, in this section, the distribution of the shear stress and normal stress on the shear failure plane was further studied.

On the numerical shear stress versus shear displacement curve for the cement grout with a *w*/*c* ratio of 0.4, another three different points when the shear displacement increased to 0.6 mm, 0.94 mm and 1.2 mm, were selected. At those points, the shear stress and normal stress distribution on the shear failure plane was plotted.

When the shear displacement was 0.6 mm, the shear stress and normal stress distribution on the shear failure plane was shown in Fig. 3.13. At this point, the shear stress distribution on the interface was generally uniform. On the contacted

interface, the maximum shear stress was 4.97 MPa while the minimum shear stress was 4.63 MPa. The relative difference between the maximum and the minimum shear stresses was only 0.34 MPa and the standard deviation was 0.09. Since this relative difference was too small, it can be neglected.

As for the normal stress, on the contacted interface, there was a non-uniform distribution. Specifically, the maximum normal stress was around 2.96 MPa while the minimum normal stress was around 1.69 MPa. The relative difference between the maximum and the minimum normal stresses was 1.27 MPa, and the standard deviation was 0.29.

When the shear displacement increased to 0.94 m, the distribution of the shear stress and normal stress is shown in Fig. 3.14. Currently, there was an apparent non-uniform distribution of the shear stress on the contacted interface. At the left side, the shear stress was relatively higher, with a maximum of 7.33 MPa. As for the right side, the minimum was around 6.20 MPa. The relative difference between the maximum

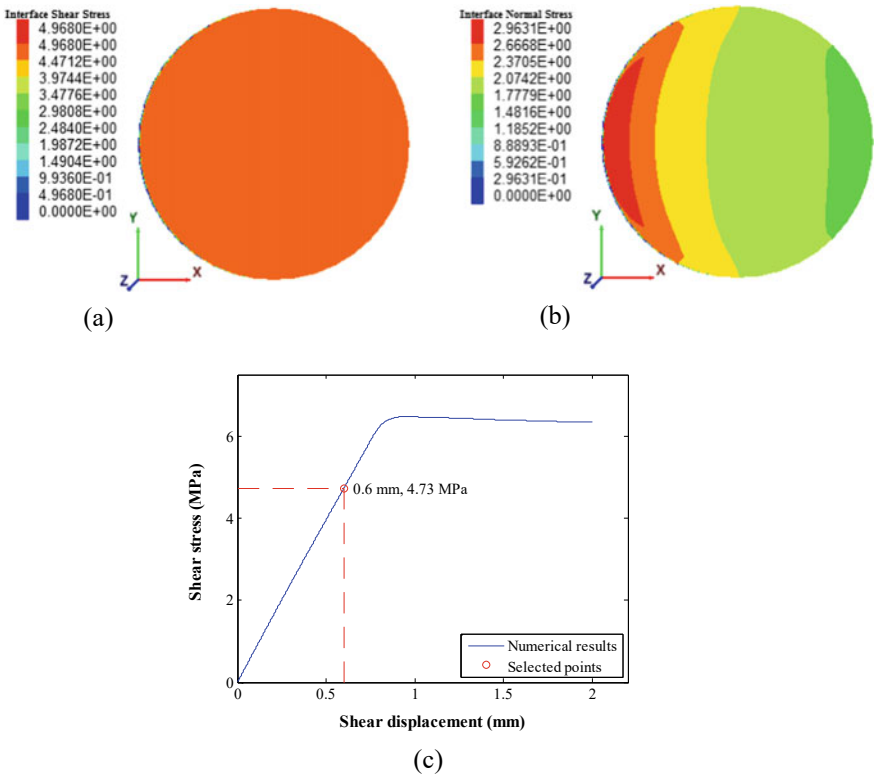

Fig. 3.13 Distribution of the shear stress and normal stress on the shear failure plane when the shear displacement arrived at 0.6 mm: **a** shear stress distribution; **b** normal stress distribution; **c** point selected on shear stress–shear displacement curve

shear stress and minimum shear stresses was 1.13 MPa, and the standard deviation was 0.28.

The results also revealed that the non-uniform distribution of the normal stress became more apparent. On the contacted interface, the maximum normal stress was 3.63 MPa, occurring at the left side while the minimum normal stress was 1.55 MPa, occurring at the right side. The relative difference between the maximum normal stress and minimum normal stress was 2.08 MPa, and the standard deviation was 0.5.

When the shear displacement reached 1.2 mm, the non-uniform shear stress distribution was still maintained, as shown in Fig. 3.15. On the contacted interface, the maximum shear stress was 7.39 MPa while the minimum shear stress was 6.18 MPa. The relative difference between the maximum shear stress and the minimum shear stress was 1.21 MPa, and the standard deviation was 0.29.

As for the normal stress distribution, it was still non-uniform. At the left side of the contacted interface, the normal stress was much higher, with a maximum

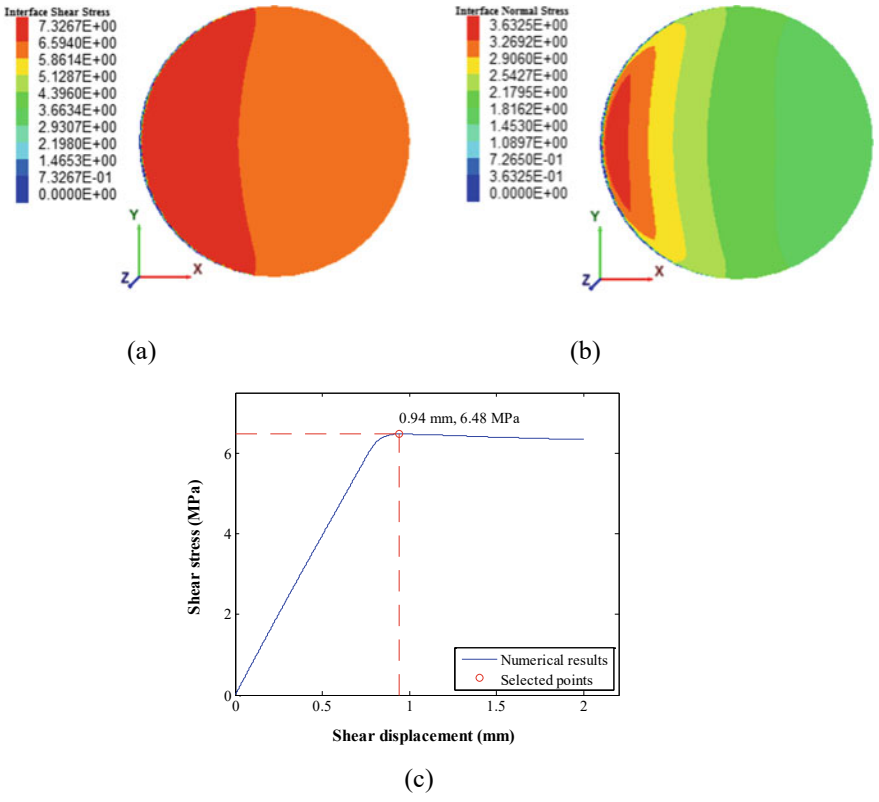

Fig. 3.14 Distribution of the shear stress and normal stress on the shear failure plane when the shear displacement arrived at 0.94 mm: **a** shear stress distribution; **b** normal stress distribution; **c** point selected on shear stress–shear displacement curve

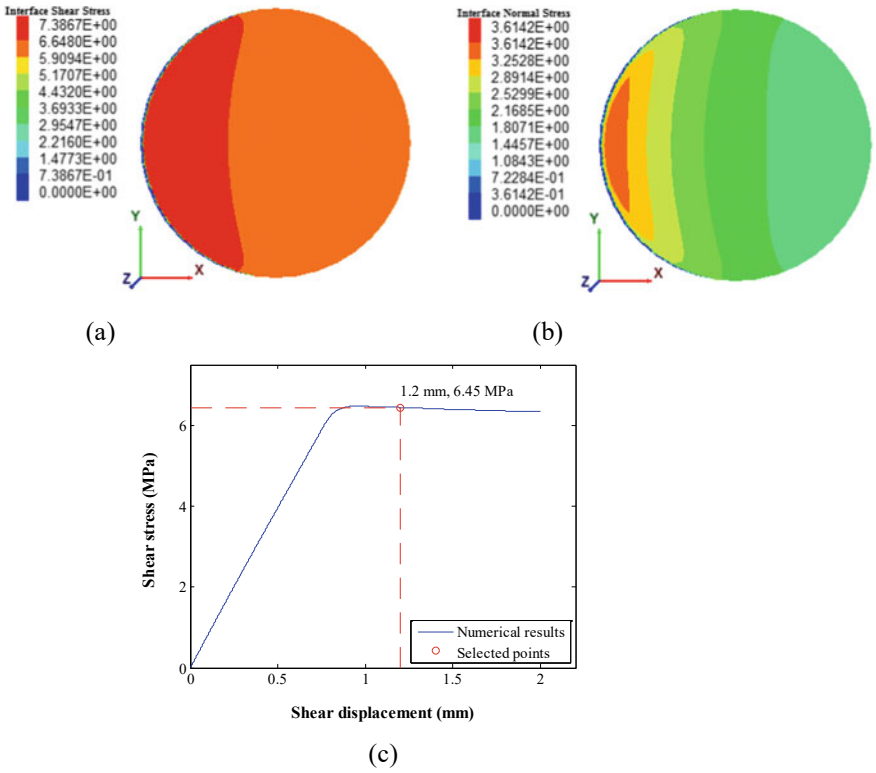

Fig. 3.15 Distribution of the shear stress and normal stress on the shear failure plane when the shear displacement arrived at 1.2 mm: **a** shear stress distribution; **b** normal stress distribution; **c** point selected on shear stress–shear displacement curve

of 3.61 MPa. At the right side, the normal stress was smaller, with a minimum of 1.52 MPa. The relative difference between the maximum normal stress and minimum normal stress was 2.09 MPa, and the standard deviation was 0.5.

The above three figures showed that at the beginning of the direct shear test, on the contacted area of the shear failure plane, the relative difference between the maximum shear stress and minimum shear stress was quite small. However, with the shear displacement increasing, the relative difference became larger.

To show the variation of the relative difference of the shear stresses, in the calculating process, the relative difference between the maximum shear stress and the minimum shear stress was monitored, as shown in Fig. 3.16. When the shear displacement was smaller than 0.81 mm, the relative difference of shear stresses was quite small. This indicated that in this stage, the shear stress can be regarded that it uniformly distributed on the shear failure plane. However, after that, the relative difference of the shear stresses increased dramatically. When the shear displacement

increased to 0.97 mm, which was around the shear strength point, the relative difference of the shear stresses was maximal. After that, the relative difference became almost constant.

Meanwhile, the relative difference between the maximum normal stress and minimum normal stress was monitored, as shown in Fig. 3.17. It shows that before the shear displacement increased to 0.97 mm, which was around the shear strength point, the relative difference increased monotonously. After that, the relative difference became also constant.

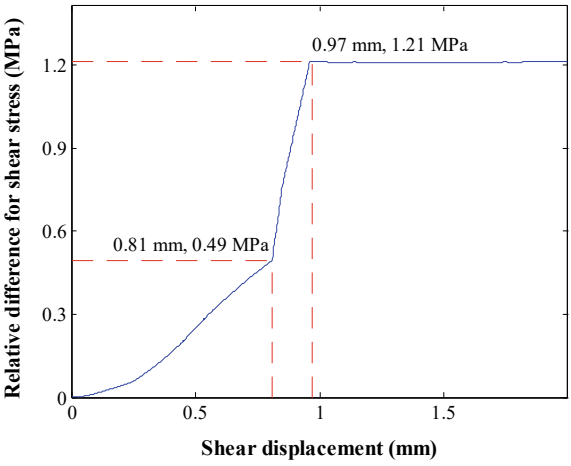

Fig. 3.16 Variation of the relative difference of shear stresses in the numerical test

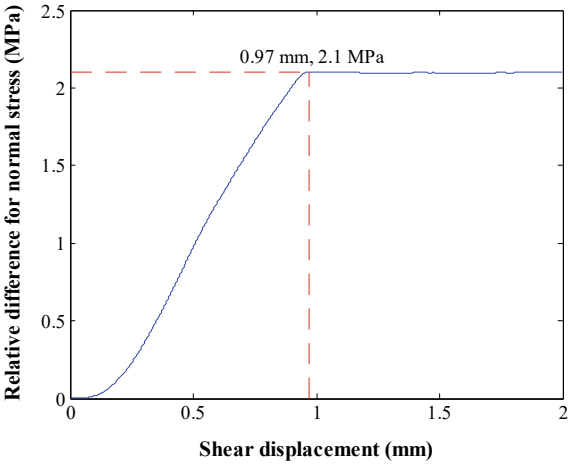

Fig. 3.17 Variation of the relative difference of normal stresses in the numerical test

3.5 Recommendation for Further Work

Following the current study, the authors plan to continue the numerical study on the shear behaviour of cement grouts. Considering that the shear behaviour of cement grouts can also be studied with tri-axial tests, the authors may use the numerical method to evaluate the mechanical response of cement grouts under the tri-axial loading condition. Its purpose is to reveal the shear failure mechanism of cement grout during the tri-axial loading process.

3.6 Conclusions

Shear behaviour of the cement grout plays a significant role in determining the stability of systems and structures in civil and mining engineering. To better understand the shear behaviour of the cement grout, numerical direct shear tests were performed with the FLAC3D software.

Cylindrical cement grout samples with two different strengths were established and numerically simulated. The numerical simulation results were compared with experimental results. There was a good correlation between them, confirming that numerical simulation can be used to evaluate the shear behaviour of the cement grout.

The numerical direct shear test results showed that in the shearing process, along the shear failure plane, the shear stress at each point was not identical. There was a shear stress distribution on the contacted shear failure plane. At the beginning of the direct shear test, the relative difference of the shear stresses was quite small. Then, in this stage, it can be assumed that there was a uniform shear stress distribution on the contacted shear failure plane. However, once the shear displacement increased to around the shear strength point, the relative difference of the shear stresses became much larger. In this stage, the shear stress was non-uniformly distributed on the contacted shear failure plane. After that, the relative difference of the shear stress became stable.

Additionally, although the applied normal stress on the sample was constant, the normal stress on the contacted shear failure plane was variable. Before the shear strength point, the normal stress increased slightly. After that, the normal stress gradually decreased. There was also a distribution of the normal stress on the contacted shear failure plane. This normal stress distribution was not apparent at the beginning of the test. However, when the shear displacement increased to around the shear strength point, it became much obvious. Moreover, after that, this non-uniform normal stress distribution became stable.

References

1. Z. Wang, Y. Song, Adsorption properties of CFBC ash–cement pastes as compared with PCC fly ash–cement pastes. Int. J. Coal Sci. Technol. **3**(1), 62–67 (2016). https://doi.org/10.1007/s40789-016-0103-8
2. S. Tang, Y. Wang, Z. Geng, X. Xu, W. Yu, J. Chen, Structure, fractality, mechanics and durability of calcium silicate hydrates. Fractal Fractional **5**(2), 5020047 (2021). http://doi.org/10.3390/fractalfract5020047
3. L. Wang, T. He, Y. Zhou, S. Tang, J. Tan, Z. Liu, J. Su, The influence of fiber type and length on the cracking resistance, durability and pore structure of face slab concrete. Constr. Build. Mater. **282**, 122706 (2021). https://doi.org/10.1016/j.conbuildmat.2021.122706
4. S. Wang, D. Li, C. Li, C. Zhang, Y. Zhang, Thermal radiation characteristics of stress evolution of a circular tunnel excavation under different confining pressures. Tunn. Undergr. Space Technol. **78**, 76–83 (2018). https://doi.org/10.1016/j.tust.2018.04.021
5. M. Ghadimi, K. Shahriar, H. Jalalifar, Study of fully grouted rock bolt in Tabas Coal Mine using numerical and instrumentation methods. Arab. J. Sci. Eng. **41**(6), 2305–2313 (2016). https://doi.org/10.1007/s13369-015-1935-z
6. M. Wang, J. Bai, W. Li, X. Wang, S. Cao, Failure mechanism and control of deep gob-side entry. Arab. J. Geosci. **8**(11), 9117–9131 (2015). https://doi.org/10.1007/s12517-015-1904-6
7. L. Wang, F. Guo, Y. Lin, H. Yang, S. Tang, Comparison between the effects of phosphorous slag and fly ash on the C-S-H structure, long-term hydration heat and volume deformation of cement-based materials. Constr. Build. Mater. **250**, 118807 (2020). https://doi.org/10.1016/j.conbuildmat.2020.118807
8. R.F. Feldman, J.J. Beaudoin, Microstructure and strength of hydrated cement. Cem. Concr. Res. **6**(3), 389–400 (1976). https://doi.org/10.1016/0008-8846(76)90102-2
9. P.L. Domone, H. Thurairatnam, Development of mechanical properties of ordinary Portland and Oilwell B cement grouts. Mag. Concr. Res. **38**(136), 129–138 (1986). https://doi.org/10.1680/macr.1986.38.136.129
10. A.J. Hyett, W.F. Bawden, A.L. Coulson, Physical and mechanical properties of normal Portland cement pertaining to fully grouted cable bolts, in *Proceedings of the International Symposium on Rock Support*, Sudbury, Canada (1992), pp. 341–348
11. A. Boumiz, C. Vernet, F.C. Tenoudji, Mechanical properties of cement pastes and mortars at early ages. Adv. Cem. Based Mater. **3**, 94–106 (1996). https://doi.org/10.1016/S1065-7355(96)90042-5
12. H. Li, H. Xiao, J. Qu, A study on mechanical and pressure-sensitive properties of cement mortar with nanophase materials. Cem. Concr. Res. **34**(3), 435–438 (2004). https://doi.org/10.1016/j.cemconres.2003.08.025
13. A. Mirza, N. Aziz, W. Ye, J. Nemcik, Mechanical properties of grouts at various curing times, in *Coal Operators' Conference*, University of Wollongong, Wollongong, Australia (2016), pp. 84–90
14. S. Ma, X. Zhu, W. Qin, S. Hu, Determination of the bond-slip relationship of fully grouted rockbolts. Environ. Earth Sci. **77**(9), 325–326 (2018). https://doi.org/10.1007/s12665-018-7495-2
15. J. Chen, H. Zhao, F. He, J. Zhang, K. Tao, Studying the performance of fully encapsulated rock bolts with modified structural elements. Int. J. Coal Sci. Technol. **8**(1), 64–76 (2021). https://doi.org/10.1007/s40789-020-00388-z
16. J. Chen, X. Dai, J. Zhang, Analytical studying the confining medium diameter impact on bearing capacity of rock bolts. Math. Probl. Eng. **2021**, 6680886 (2021). http://doi.org/10.1155/2021/6680886
17. A.J. Hyett, W.F. Bawden, R.D. Reichert, The effect of rock mass confinement on the bond strength of fully grouted cable bolts. Int. J. Rock Mech. Min. Sci. **29**(5), 503–524 (1992). https://doi.org/10.1016/0148-9062(92)92634-O
18. P. Simms, M. Grabinsky, Direct measurement of matric suction in triaxial tests on early-age cemented paste backfill. Can. Geotech. J. **46**, 93–101 (2009). https://doi.org/10.1139/T08-098

19. Y. Sakai, M. Nakatani, A. Takeuchi, Y. Omorai, T. Kishi, Mechanical behaviour of cement paste and alterations of hydrates under high-pressure triaxial testing. J. Adv. Concr. Technol. **14**, 1–12 (2016). https://doi.org/10.3151/jact.14.1
20. N. Aziz, D. Majoor, A. Mirzaghorbanali, Strength properties of grout for strata reinforcement. Procedia Eng. **191**, 1178–1184 (2017). https://doi.org/10.1016/j.proeng.2017.05.293
21. J. Chen, C. Xu, A study of the shear behaviour of a Portland cement grout with the triaxial test. Constr. Build. Mater. **176**, 81–88 (2018). https://doi.org/10.1016/j.conbuildmat.2018.04.189
22. Z. Zhang, M. Deng, J. Bai, X. Yu, Q. Wu, L. Jiang, Strain energy evolution and conversion under triaxial unloading confining pressure tests due to gob-side entry retained. Int. J. Rock Mech. Min. Sci. **126**, 1–10 (2020). https://doi.org/10.1016/j.ijrmms.2019.104184
23. S. Wang, H.G. Xiao, Z.S. Zou, C. Cao, Y.H. Wang, Z.L. Wang, Mechanical performances of transverse rib bar during pull-out test. Int. J. Appl. Mech. **11**(5), 1–15 (2019). https://doi.org/10.1142/S1758825119500480
24. M. Moosavi, *Load Distribution Along Fully Grouted Cable Bolts Based on Constitutive Models Obtained from Modified Hoek Cells* (Queen's University, Kingston, 1997)
25. M. Moosavi, W.F. Bawden, Shear strength of Portland cement grout. Cement Concr. Compos. **25**(7), 729–735 (2003). https://doi.org/10.1016/S0958-9465(02)00101-4
26. G. Lu, K. Wang, Investigation into yield behaviour of fresh cement paste: model and experiment. ACI Mater. J. **107**(1), 12–19 (2010)
27. J.J. Assaad, J. Harb, Y. Maalouf, Measurement of yield stress of cement pastes using the direct shear test. J. Nonnewton. Fluid Mech. **214**, 18–27 (2014). https://doi.org/10.1016/j.jnnfm.2014.10.009
28. J. Chen, P.C. Hagan, S. Saydam, Shear behaviour of a cement grout tested in the direct shear test. Constr. Build. Mater. **166**, 271–279 (2018). https://doi.org/10.1016/j.conbuildmat.2018.01.151
29. W. Li, F.U.A. Shaikh, L. Wang, Y. Lu, B. Wang, C. Jiang, Y. Su, Experimental study on shear property and rheological characteristic of superfine cement grouts with nano-SiO_2 addition. Constr. Build. Mater. **228**, 1–11 (2019). https://doi.org/10.1016/j.conbuildmat.2019.117046
30. J. Chen, S. Saydam, P.C. Hagan, Numerical simulation of the pull-out behaviour of fully grouted cable bolts. Constr. Build. Mater. **191**, 1148–1158 (2018). https://doi.org/10.1016/j.conbuildmat.2018.10.083
31. X. Li, Z.C. Grasley, J.W. Bullard, E.J. Garboczi, Computing the time evolution of the apparent viscoelastic/viscoplastic Poisson's ratio of hydrating cement paste. Cement Concr. Compos. **56**, 121–133 (2015). https://doi.org/10.1016/j.cemconcomp.2014.11.004

Chapter 4
Analytical Modelling to Study the Load Transfer Performance of Fully Grouted Rock Bolts

4.1 Introduction

A rock bolt is a rock tendon which can be either a rod or a strand, installed in a borehole to reinforce the surround rock mass and soil [1]. Rock bolts have been used in civil and mining for a long time [2]. Numerous filed applications and computer simulation have proved that rock bolts play a significant role in improving the internal strength of rock mass and enhancing the safety of underground excavations [3–6].

The rock bolt reinforcement system is basically composed of four components: the surrounding confining medium, e.g. rocks or soils, the rock reinforcement element, the internal fixture and the external fixture [7–9]. It is found that all these four components have an influence on the performance of a reinforcement system.

To better understand the performance of the reinforcement system, Thompson et al. [10] classified the rock reinforcement system as three types: Continuously Mechanically Coupled (CMC), Continuously Frictionally Coupled and Discrete Mechanically or Frictionally Coupled. This study deals with fully grouted rock bolts, and based on this classification, fully grouted rock bolts belong to the CMC system.

For the CMC system, cementitious grout or polyester resin can be used to bond rock bolts with surrounding confining medium [11–13]. Via the bonding material, the load from exterior unstable rock mass can be transferred to interior stable rock mass. It should be mentioned that in the in situ applications, rock bolts can encounter axial, shear, combined axial and shear loading conditions [14]. However, this paper focused on the axial performance of rock bolts.

Failure of the rock bolting system has different modes. Jeremic and Delaire [15] summarised that failure of the rock bolting system can be classified as bond failure of the bolt/grout interface, bond failure of the grout/rock interface, failure of the grout annulus and failure in the surrounding rock mass. Then, Hutchinson and Diederichs [16] added that rupture of the rock tendon also occurred in the in situ scenario. Nevertheless, among these failure modes, bond failure of the bolt/grout interface and the grout/rock interface are more common to encounter [17].

J. Chen et al., *Bond Failure Mechanism of Fully Grouted Rock Bolts*,
SpringerBriefs in Applied Sciences and Technology,
https://doi.org/10.1007/978-981-99-0498-3_4

Jalalifar [18] stated that when fully grouted rock bolts were loaded axially, the shear stress along the bolt/grout interface was larger than the shear stress along the grout/rock interface because the bolt/grout interface had a smaller contact area. When the grout and the rock had similar strength, failure was likely to occur along the bolt/grout interface. Previous experimental pull-out tests also showed that bond failure of the bolt/grout interface occurred in the tests [19, 20]. Therefore, this paper deals with the bond failure of the bolt/grout interface.

Gambarova [21] stated that the bonding performance of the bolt/grout interface mainly relies on chemical adhesion, mechanical interlock and friction. Chemical adhesion plays a negligible role on the bonding performance and can be easily removed after a small relative movement between the bolt and grout [22].

To understand the load transfer performance of rock bolts, extensive research has been conducted via experimental pull-out tests [23–25]. Compared with that, much less work has been conducted with analytical modelling. Hawkes and Evans [26] conducted the pioneering work in analytically modelling the load transfer of rock bolts. Specifically, an analytical model was proposed to evaluate the load distribution along a fully grouted rock bolt. However, this assumption was only valid in the coupling stage. In the modelling process, a linear relationship between the axial stress in the bolt and the shear stress along the bolt/grout interface was assumed. However, this assumption was credible when the bolt was fully coupled with the surrounding medium. With the axial load in the bolt increasing, debonding occurred along the bolt/grout interface and this assumption may not be valid again. Farmer [27] deduced an analytical model to study the load distribution along a rock bolt. In this analytical model, it was assumed that the shear stress along the bolt/grout interface was linear with the grout shear modulus. Therefore, this model was only applicable when the bolt/grout interface underwent elastic behaviour. Once debonding occurred along the bolt/grout interface, the credibility of this analytical model decreased. Aydan et al. [28] deduced an analytical solution to study the load transfer of rock bolts. However, no experimental work was conducted to validate the credibility of the model. Rajaie [29] studied the load transfer of cable bolts and an energy approach was adopted to analyse the loading process of cable bolts. There was a good correlation between laboratory results and analytical results. However, this model mainly focused on the peak load calculation and no equation was deduced to calculate the load variation with displacement in the pull-out process. Therefore, this model cannot be used to study the load–displacement relationship of cable bolts.

Yazici and Kaiser [30] proposed a bond strength model to study the load transfer of plain cable bolts. Later, this model was modified to study the influence of stress change on load transfer of cable bolts [31]. This model treated the bolt/grout interface as a zigzag geometry, similar to a rock joint. For the rock joint, strength of the rock is usually weak along two sides. However, for the cable bolting system, strength of the steel is much higher along the bolt side. Following that, Hyett et al. [32] developed a constitutive model to study the load–displacement performance of cable bolts. Two different boundary conditions, constant normal stress and constant normal stiffness, were considered. This model assumed that the shear stress along the bolt/grout interface was uniform. However, experimental work proved that when

the bolt had a long embedment length, the shear stress along the bolt/grout interface was not uniform [22]. Therefore, this model was applicable to calculate the load–displacement relationship for short-embedded bolts. However, it may not be suitable for long-embedded bolts. A load distribution model was proposed by Hyett et al. [33]. This model can study the load distribution in the embedment section and the anchor section. Moosavi [34] developed an analytical model for modified cable bolts. However, when modified cable bolts were used to reinforce rock masses, the modified geometry can be installed at different positions in the embedment section. And, the influence of the modified geometry position on the load transfer performance of cable bolts was not considered. Li and Stillborg [35] developed an analytical model to study the load distribution of rock bolts. The bolt/grout interface was assumed to be composed of four sections: completely debonded, partially debonded, softening and elastic.

Cai et al. [36] used a modified shear-lag model to study the load transfer of rock bolts. However, the softening behaviour of the bolt/grout interface was neglected. Xiao and Chen [37] assumed that the bolt/grout interface underwent elastic, softening and debonding stages and developed a model for rock bolts. Ren et al. [38] deduced the load transfer process of rock bolts with an analytical model. Experimental work was used to validate the credibility of this analytical model. However, when deducing the analytical model, it was assumed that the shear slippage of the bolt/grout interface was equal to the axial displacement of the rock bolt. Then, the displacement of the surrounding confining medium was neglected. Consequently, this model cannot be used to study the influence of the surrounding confining medium on the performance of rock bolts. Blanco Martín et al. [39] proposed an analytical solution to evaluate the load–displacement performance of rock bolts. Jalalifar [40] evaluated the performance of rock bolts installed in an elastoplastic rock mass. In this model, it was assumed that the shear force in the grout annulus had a linear relationship with the shear slippage. Therefore, this model was only valid when the bolt/grout interface underwent elastic deformation. After the bolt/grout interface started plastic deformation, this model was not valid again. Cao et al. [41] studied the influence of rib geometry on the bonding capacity of rock bolts. It was predicted that rock bolts with small rib face angles were more effective in hard rock conditions.

Ma et al. [42] used a nonlinear equation to depict the bond-slip behaviour of the bolt/grout interface and studied the load transfer of rock bolts. Later, the model was modified to study the influence of free-end slip on the performance of rock bolts [43]. However, in this model, an empirical equation was used to depict the bond-slip relationship of the bolt/grout interface. Therefore, the properties of the rock bolting system may modify the coefficients in the bond-slip model. Consequently, this model cannot be used to predict the influence of rock mass confinement on the performance of rock bolts. Chen et al. [13] used an analytical model to study the axial performance of cable bolts. However, the model was only appropriate for laboratory pull-out scenario. Li et al. [44] developed an analytical model to study the load transfer of modified cable bolts. Cable bolts with short embedment length

were used to validate the model. However, in situ tests proved that the installed cable bolts can be very long for the field scenario [45]. And whether this model can be used to study the performance of cable bolts with long embedment length was not discussed.

The literature review shows that for the rock bolting system, when the shear behaviour of the bolt/grout interface was depicted with a bond-slip equation, different analytical models can be used, such as the exponential model [42] or the tri-linear model [46]. Among them, the tri-linear model considers the elastic, softening and debonding behaviour of the bolt/grout interface and thus is more commonly used. However, when the tri-linear model was incorporated into the rock bolting system to deduce the load–displacement relationship of rock bolts, the involvement of the surrounding confining medium was usually not considered.

It should be mentioned that Vaculik et al. [47] conducted an analytical study to evaluate the load-slip relationship of the FRP-to-substrate joints with the bond-slip model. A framework was proposed to depict the performance of FRP-to-substrate joints. However, for the rock bolting system, cylindrical rock bolts are always used to reinforce the excavated rock masses, such as tunnels, roadways and stopes [48, 49]. Therefore, this paper applies the method proposed by Vaculik et al. [47] into the fully grouted rock bolting system and further deduced the specific analytical solution for fully grouted rock bolts. Additionally, they evaluated the performance of FRP-to-substrate joints with the embedment length ranging from short to long. However, for fully grouted rock bolts, the embedment length is usually extremely long [45, 50]. For example, Cao et al. [51] summarised that the embedment length for a rock bolt can be around 3 m. Furthermore, when the cable bolt is used, the embedment length may range from 3 to 15 m. Considering this, this paper especially focused on the long embedment length scenario for rock bolts.

First the relationship between the shear stress of the bolt/grout interface and the shear slippage was simulated with a tri-linear model. Then, the pull-out process of rock bolts was analysed with five stages: elastic, elastic-softening, elastic-softening-debonding, softening-debonding and debonding stages. After that, the analytical model was validated with experimental pull-out tests. Last, a parametric study was conducted to evaluate the influence of elastic modulus of the confining medium, the shear strength of the bolt/grout interface and the residual shear strength of the bolt/grout interface on the load transfer performance of rock bolts.

4.2 Analytical Modelling

4.2.1 Bond-Slip Model

A tri-linear model was used to depict the bond-slip behaviour of the bolt/grout interface. The tri-linear model is composed of three parts: ascending section, descending section and horizontal section [13, 38], as shown in Fig. 4.1. Specifically, with the

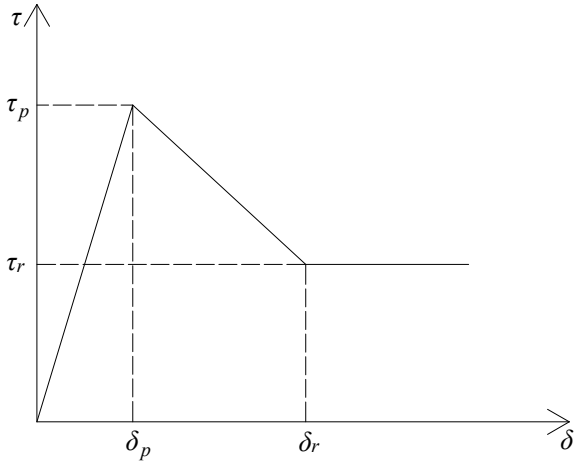

Fig. 4.1 A tri-linear model [13, 38, 47]

shear slippage of the bolt/grout interface increasing from 0 to δ_p, the shear stress increases linearly from zero to the shear strength of the bolt/grout interface. Then, with δ increasing to δ_r, the shear stress decreases linearly to the residual shear strength of the bolt/grout interface. After δ_r, the shear stress keeps constant and equals τ_r.

Therefore, the tri-linear model can be expressed as Eq. (4.1a–4.1c) [13, 38]:

$$\tau = \frac{\tau_p}{\delta_p}\delta \quad (0 \le \delta \le \delta_p) \tag{4.1a}$$

$$\tau = \frac{\tau_p\delta_r - \tau_r\delta_p}{\delta_r - \delta_p} - \frac{\tau_p - \tau_r}{\delta_r - \delta_p}\delta \quad (\delta_p < \delta \le \delta_r) \tag{4.1b}$$

$$\tau = \tau_r \ (\delta > \delta_r) \tag{4.1c}$$

where τ_p: shear strength of the bolt/grout interface; τ_r: residual shear strength of the bolt/grout interface; and δ_r: shear slippage when the residual shear strength of the bolt/grout interface reaches.

4.2.2 Governing Equation

In previous research, the shear slippage of the bolt/grout interface was usually simplified as the axial displacement of the rock bolt [38, 42]. However, previous experimental work proved that the shear slippage of the bolt/grout interface was different from the axial displacement of the rock bolt because of the displacement of the confining medium [52]. Furthermore, Hyett et al. [33] found that the displacement of the confining medium had an apparent influence on the load transfer performance of rock bolts. Therefore, neglecting the displacement of the confining medium in

the analytical model could not properly reflect the load transfer performance of rock bolts. Considering this issue, in this paper, the displacement of the confining medium was included.

Since this study aims at studying the bond failure of the bolt/grout interface, the grout/medium interface was assumed to be intact in the pull-out process of rock bolts. Then, the shear slippage of the bolt/grout interface was defined as the relative movement between the rock bolt and the confining medium [53, 54]:

$$\delta(x) = u_{\mathrm{b}}(x) - u_{\mathrm{m}}(x) \tag{4.2}$$

where $\delta(x)$: shear slippage of the bolt/grout interface at the position of x; $u_{\mathrm{b}}(x)$: rock bolt displacement at the position of x; and $u_{\mathrm{m}}(x)$: confining medium displacement at the position of x.

Differentiating Eq. (4.2) twice with respect to x leads to:

$$\frac{\mathrm{d}^2\delta(x)}{\mathrm{d}x^2} = \frac{\mathrm{d}^2 u_{\mathrm{b}}(x)}{\mathrm{d}x^2} - \frac{\mathrm{d}^2 u_{\mathrm{m}}(x)}{\mathrm{d}x^2} \tag{4.3}$$

The axial stress in the rock bolt can be expressed with the displacement of the rock bolt. As for the confining medium, this is also applicable. Then, the following equations can be acquired [40]:

$$\sigma_{\mathrm{b}}(x) = E_{\mathrm{b}} \frac{\mathrm{d}u_{\mathrm{b}}(x)}{\mathrm{d}x} \tag{4.4}$$

$$\sigma_{\mathrm{m}}(x) = E_{\mathrm{m}} \frac{\mathrm{d}u_{\mathrm{m}}(x)}{\mathrm{d}x} \tag{4.5}$$

where $\sigma_{\mathrm{b}}(x)$: axial stress in the rock bolt at the position of x; $\mathrm{E_m}$: elastic modulus of the confining medium; and $\sigma_{\mathrm{m}}(x)$: axial stress applied on the confining medium.

Substituting Eqs. (4.4) and (4.5) into (4.3) leads to:

$$\frac{\mathrm{d}^2\delta(x)}{\mathrm{d}x^2} = \frac{1}{E_{\mathrm{b}}} \frac{\mathrm{d}\sigma_{\mathrm{b}}(x)}{\mathrm{d}x} - \frac{1}{E_{\mathrm{m}}} \frac{\mathrm{d}\sigma_{\mathrm{m}}(x)}{\mathrm{d}x} \tag{4.6}$$

According to the mechanical equilibrium, the relationship between the axial stress in the bolt and the axial stress applied on the confining medium can be expressed as [55]:

$$\sigma_{\mathrm{m}} = -\sigma_{\mathrm{b}} \frac{\pi r_{\mathrm{b}}^2}{A_{\mathrm{m}}} \tag{4.7}$$

where A_{m}: cross-section area of the confining medium; and $\mathrm{r_b}$: rock bolt radius.

Substituting Eq. (4.7) into Eq. (4.6) leads to:

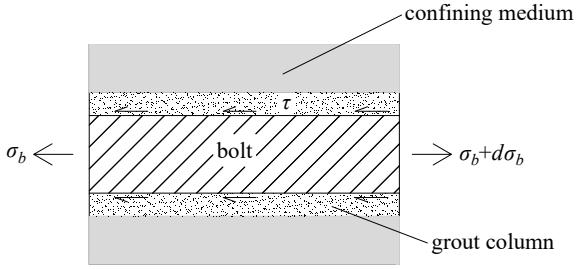

Fig. 4.2 The cross-section view of a rock bolting system

$$\frac{\mathrm{d}^2\delta(x)}{\mathrm{d}x^2} = \left(\frac{1}{E_\mathrm{b}} + \frac{\pi r_\mathrm{b}^2}{E_\mathrm{m}A_\mathrm{m}}\right)\frac{\mathrm{d}\sigma_\mathrm{b}(x)}{\mathrm{d}x} \tag{4.8}$$

The relationship between the axial stress in the rock bolt and the shear stress along the bolt/grout interface can be seen in Fig. 4.2.

Then, the following equation can be acquired [42]:

$$\tau(x) = \frac{r_\mathrm{b}}{2}\frac{\mathrm{d}\sigma_\mathrm{b}(x)}{\mathrm{d}x} \tag{4.9}$$

where $\tau(x)$: shear stress of the bolt/grout interface at the position of x.

Substituting Eq. (4.9) into Eq. (4.8) leads to:

$$\frac{\mathrm{d}^2\delta(x)}{\mathrm{d}x^2} - \frac{2}{r_\mathrm{b}}\left(\frac{1}{E_\mathrm{b}} + \frac{\pi r_\mathrm{b}^2}{E_\mathrm{m}A_\mathrm{m}}\right)\tau(x) = 0 \tag{4.10}$$

It is defined that:

$$\lambda^2 = \frac{2}{r_\mathrm{b}}\left(\frac{1}{E_\mathrm{b}} + \frac{\pi r_\mathrm{b}^2}{E_\mathrm{m}A_\mathrm{m}}\right) \tag{4.11}$$

Then, Eq. (4.10) can be written as:

$$\frac{\mathrm{d}^2\delta(x)}{\mathrm{d}x^2} - \lambda^2\tau(x) = 0 \tag{4.12}$$

Equation (4.12) is the governing equation of this analytical model, and it can be solved with the pre-defined shear stress equations.

4.2.3 Pull-Out Stages of Rock Bolts

According to previous research, the pull-out stages of the bolt/grout interface can be classified as elastic stage, elastic-softening stage, elastic-softening-debonding

stage, softening-debonding stage and debonding stage [38, 53, 56]. Therefore, in the following contents, the pull-out process of a rock bolt was analysed with those five stages.

4.2.3.1 Elastic Stage

When the pull-out load is small, the bolt/grout interface undergoes elastic deformation. And the full bolt/grout interface is elastic, as shown in Fig. 4.3.

Then, Eq. (4.1a) can be substituted into Eq. (4.12), leading to:

$$\frac{\mathrm{d}^2\delta(x)}{\mathrm{d}x^2} - \frac{\tau_\mathrm{p}}{\delta_\mathrm{p}}\lambda^2\delta(x) = 0 \tag{4.13}$$

It is defined that:

$$\lambda_1^2 = \frac{\tau_\mathrm{p}}{\delta_\mathrm{p}}\lambda^2 \tag{4.14}$$

Then, Eq. (4.13) can be written as:

$$\frac{\mathrm{d}^2\delta(x)}{\mathrm{d}x^2} - \lambda_1^2\delta(x) = 0 \tag{4.15}$$

Equation (4.15) can be solved with boundary conditions. First, the axial stress in the bolt should be deduced. According to Eq. (4.2), the following equation can be acquired:

$$\frac{\mathrm{d}\delta(x)}{\mathrm{d}x} = \frac{\mathrm{d}u_\mathrm{b}(x)}{\mathrm{d}x} - \frac{\mathrm{d}u_\mathrm{m}(x)}{\mathrm{d}x} \tag{4.16}$$

It can be further written as:

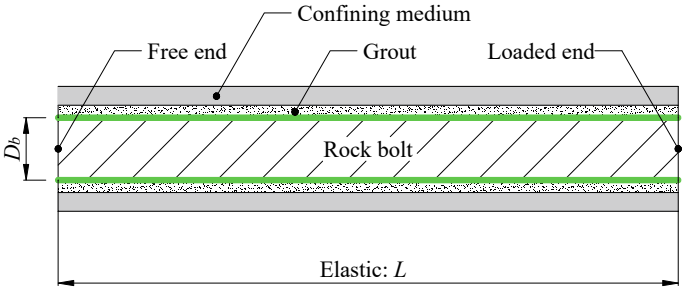

Fig. 4.3 The full bolt/grout interface is elastic in the elastic stage

$$\frac{\mathrm{d}\delta(x)}{\mathrm{d}x} = \frac{\sigma_\mathrm{b}(x)}{E_\mathrm{b}} - \frac{\sigma_\mathrm{m}(x)}{E_\mathrm{m}} \tag{4.17}$$

Substituting Eq. (4.7) into Eq. (4.17) leads to:

$$\frac{\mathrm{d}\delta(x)}{\mathrm{d}x} = \left(\frac{1}{E_\mathrm{b}} + \frac{\pi r_\mathrm{b}^2}{E_\mathrm{m} A_\mathrm{m}}\right)\sigma_\mathrm{b}(x) \tag{4.18}$$

Substituting Eq. (4.11) into Eq. (4.18), the axial stress in the bolt can be written as:

$$\sigma_\mathrm{b}(x) = \frac{2}{r_\mathrm{b}\lambda^2}\frac{\mathrm{d}\delta(x)}{\mathrm{d}x} \tag{4.19}$$

The boundary conditions are:

$$\sigma_\mathrm{b}(x = 0) = 0 \tag{4.20}$$

$$\sigma_\mathrm{b}(x = L) = \frac{F}{\pi r_\mathrm{b}^2} \tag{4.21}$$

Combining Eqs. (4.19), (4.20) and (4.21) with Eq. (4.15) leads to:

$$\delta(x) = \frac{F\lambda_1\delta_\mathrm{p}}{2\pi r_\mathrm{b}\tau_\mathrm{p}\sinh(\lambda_1 L)}\cosh(\lambda_1 x) \tag{4.22}$$

$$\sigma_\mathrm{b}(x) = \frac{F}{\pi r_\mathrm{b}^2\sinh(\lambda_1 L)}\sinh(\lambda_1 x) \tag{4.23}$$

$$\tau(x) = \frac{F\lambda_1}{2\pi r_\mathrm{b}\sinh(\lambda_1 L)}\cosh(\lambda_1 x) \tag{4.24}$$

It is defined that at the loaded end, the shear slippage of the bolt/grout interface is equal to the pull-out displacement of the rock bolt [57]. Substituting $x = L$ into Eq. (4.22), the pull-out load of the rock bolt can be expressed as:

$$F = \frac{2\pi r_\mathrm{b}\tau_\mathrm{p}\tanh(\lambda_1 L)}{\lambda_1\delta_\mathrm{p}}u_\mathrm{b} \tag{4.25}$$

At the end of this stage, the shear stress at the position of $x = L$ increases to the shear strength of the bolt/grout interface. Therefore, substituting $\tau(x = L) = \tau_\mathrm{p}$ into Eq. (4.24) leads to:

$$F_\mathrm{sof} = \frac{2\pi r_\mathrm{b}\tau_\mathrm{p}\tanh(\lambda_1 L)}{\lambda_1} \tag{4.26}$$

where F_{sof}: pull-out load when the bolt/grout interface starts softening.

4.2.3.2 Elastic-Softening Stage

In the elastic-softening stage, the full bolt/grout interface is composed of elastic section and softening section, as shown in Fig. 4.4.

It is defined that a_s is the softening length. In the elastic-softening stage, the interface in the domain $[0, L - a_s]$ is still elastic. A boundary condition is Eq. (4.20) and the other boundary condition is:

$$\tau(x = L - a_s) = \tau_p \tag{4.27}$$

Combining Eqs. (4.9), (4.19), (4.20) and (4.27) with Eq. (4.15) leads to:

$$\delta(x) = \frac{\delta_p}{\cosh(\lambda_1(L - a_s))} \cosh(\lambda_1 x) \tag{4.28}$$

$$\sigma_b(x) = \frac{2\tau_p}{r_b\lambda_1 \cosh(\lambda_1(L - a_s))} \sinh(\lambda_1 x) \tag{4.29}$$

$$\tau(x) = \frac{\tau_p}{\cosh(\lambda_1(L - a_s))} \cosh(\lambda_1 x) \tag{4.30}$$

Substituting $x = L - a_s$ into Eq. (4.29), the axial stress can be acquired:

$$\sigma_b(x = L - a_s) = \frac{2\tau_p}{r_b\lambda_1} \tanh(\lambda_1(L - a_s)) \tag{4.31}$$

In the domain $[L - a_s, L]$, the bolt/grout interface softens. Substituting Eq. (4.1b) into Eq. (4.12) leads to:

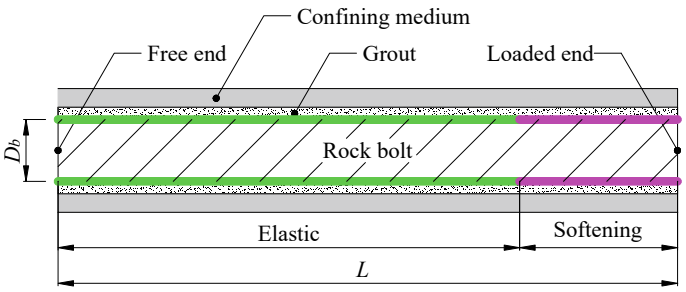

Fig. 4.4 The full bolt/grout interface is composed of elastic section and softening section in the elastic-softening stage

$$\frac{\mathrm{d}^2\delta(x)}{\mathrm{d}x^2}+\lambda^2\frac{\tau_\mathrm{p}-\tau_\mathrm{r}}{\delta_\mathrm{r}-\delta_\mathrm{p}}\delta(x)-\lambda^2\frac{\tau_\mathrm{p}\delta_\mathrm{r}-\tau_\mathrm{r}\delta_\mathrm{p}}{\delta_\mathrm{r}-\delta_\mathrm{p}}=0 \tag{4.32}$$

It is defined that:

$$\lambda_2^2=\frac{\tau_\mathrm{p}-\tau_\mathrm{r}}{\delta_\mathrm{r}-\delta_\mathrm{p}}\lambda^2 \tag{4.33}$$

Therefore, Eq. (4.32) can be further written as:

$$\frac{\mathrm{d}^2\delta(x)}{\mathrm{d}x^2}+\lambda_2^2\delta(x)-\lambda_2^2\frac{\tau_\mathrm{p}\delta_\mathrm{r}-\tau_\mathrm{r}\delta_\mathrm{p}}{\tau_\mathrm{p}-\tau_\mathrm{r}}=0 \tag{4.34}$$

The boundary conditions are Eqs. (4.27) and (4.31). Combining Eqs. (4.9), (4.19), (4.27) and (4.31) with Eq. (4.34) leads to:

$$\begin{aligned}\delta(x)=&\frac{\lambda_1\delta_\mathrm{p}}{\lambda_2}\tanh(\lambda_1(L-a_\mathrm{s}))\sin(\lambda_2(x+a_\mathrm{s}-L))\\&-\frac{\lambda_1^2\delta_\mathrm{p}}{\lambda_2^2}\cos(\lambda_2(L-a_\mathrm{s}-x))+\frac{\tau_\mathrm{p}\delta_\mathrm{r}-\tau_\mathrm{r}\delta_\mathrm{p}}{\tau_\mathrm{p}-\tau_\mathrm{r}}\end{aligned} \tag{4.35}$$

$$\begin{aligned}\sigma_\mathrm{b}(x)=&\frac{2\tau_\mathrm{p}}{r_\mathrm{b}}\left(\frac{1}{\lambda_1}\tanh(\lambda_1(L-a_\mathrm{s}))\cos(\lambda_2(L-a_\mathrm{s}-x))\right.\\&\left.+\frac{1}{\lambda_2}\sin(\lambda_2(x+a_\mathrm{s}-L))\right)\end{aligned} \tag{4.36}$$

$$\tau(x)=\tau_\mathrm{p}\left(\frac{\lambda_2}{\lambda_1}\tanh(\lambda_1(L-a_\mathrm{s}))\sin(\lambda_2(L-a_\mathrm{s}-x))+\cos(\lambda_2(L-a_\mathrm{s}-x))\right) \tag{4.37}$$

Substituting $x=L$ and $\sigma_\mathrm{b}(x=L)=\frac{F}{\pi r_\mathrm{b}^2}$ into Eqs. (4.35) and (4.36), respectively, the pull-out displacement and pull-out load of the rock bolt can be acquired:

$$F=2\pi r_\mathrm{b}\tau_\mathrm{p}\left(\frac{1}{\lambda_1}\tanh(\lambda_1(L-a_\mathrm{s}))\cos(\lambda_2 a_\mathrm{s})+\frac{1}{\lambda_2}\sin(\lambda_2 a_\mathrm{s})\right) \tag{4.38}$$

$$u_\mathrm{b}=\frac{\lambda_1\delta_\mathrm{p}}{\lambda_2}\tanh(\lambda_1(L-a_\mathrm{s}))\sin(\lambda_2 a_\mathrm{s})-\frac{\lambda_1^2\delta_\mathrm{p}}{\lambda_2^2}\cos(\lambda_2 a_\mathrm{s})+\frac{\tau_\mathrm{p}\delta_\mathrm{r}-\tau_\mathrm{r}\delta_\mathrm{p}}{\tau_\mathrm{p}-\tau_\mathrm{r}} \tag{4.39}$$

At the end of this stage, the shear stress at the position of $x=L$ reduces to τ_r. Therefore, substituting $\tau(x=L)=\tau_\mathrm{r}$ into Eq. (4.37) leads to:

$$\cos(\lambda_2 a_\mathrm{s})-\frac{\lambda_2}{\lambda_1}\tanh(\lambda_1(L-a_\mathrm{s}))\sin(\lambda_2 a_\mathrm{s})=\frac{\tau_\mathrm{r}}{\tau_\mathrm{p}} \tag{4.40}$$

For an infinite embedment length, $\tanh(\lambda_1(L-a_s))$ is equal to 1. Then, the softening length when the elastic-softening stage ends can be acquired:

$$a_{s1}=\frac{1}{\lambda_2}\left(\arcsin\frac{\lambda_1}{\sqrt{\lambda_1^2+\lambda_2^2}}-\arcsin\frac{\tau_r\lambda_1}{\tau_p\sqrt{\lambda_1^2+\lambda_2^2}}\right) \tag{4.41}$$

where a_{s1}: the softening length when the elastic-softening stage ends.

4.2.3.3 Elastic-Softening-Debonding Stage

After $\tau(x=L)$ reduces to τ_r, the bolt/grout interface enters the elastic-softening-debonding stage. In this stage, the full bolt/grout interface is composed of elastic section, softening section and debonding section, as shown in Fig. 4.5.

Assuming that the debonding length is a_d, the bolt/grout interface in the domain $[0, L-a_d-a_s]$ is still elastic. Therefore, Eqs. (4.28), (4.29) and (4.30) are still valid if L is replaced with $L-a_d$:

$$\delta(x)=\frac{\delta_1}{\cosh(\lambda_1(L-a_d-a_s))}\cosh(\lambda_1 x) \tag{4.42}$$

$$\sigma_b(x)=\frac{2\tau_p}{r_b\lambda_1\cosh(\lambda_1(L-a_d-a_s))}\sinh(\lambda_1 x) \tag{4.43}$$

$$\tau(x)=\frac{\tau_p}{\cosh(\lambda_1(L-a_d-a_s))}\cosh(\lambda_1 x) \tag{4.44}$$

As for the domain $[L-a_d-a_s, L-a_d]$, the bolt/grout interface softens. Therefore, Eqs. (4.35), (4.36) and (4.37) are still valid if L is replaced with $(L-a_d)$:

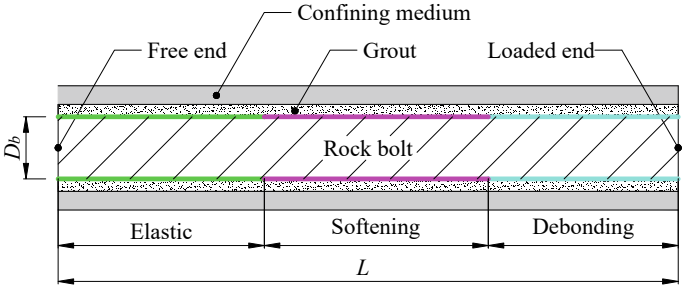

Fig. 4.5 The full bolt/grout interface is composed of elastic section, softening section and debonding section in the elastic-softening-debonding stage

$$\delta(x) = \frac{\lambda_1 \delta_p}{\lambda_2} \tanh(\lambda_1(L - a_d - a_s)) \sin(\lambda_2(x + a_d + a_s - L)) - \frac{\lambda_1^2 \delta_p}{\lambda_2^2} \cos(\lambda_2(L - a_d - a_s - x)) + \frac{\tau_p \delta_r - \tau_r \delta_p}{\tau_p - \tau_r} \tag{4.45}$$

$$\sigma_b(x) = \frac{2\tau_p}{r_b}\left(\frac{1}{\lambda_1} \tanh(\lambda_1(L - a_d - a_s)) \cos(\lambda_2(L - a_d - a_s - x)) + \frac{1}{\lambda_2} \sin(\lambda_2(x + a_d + a_s - L))\right) \tag{4.46}$$

$$\tau(x) = \tau_p\left(\frac{\lambda_2}{\lambda_1} \tanh(\lambda_1(L - a_d - a_s)) \sin(\lambda_2(L - a_d - a_s - x)) + \cos(\lambda_2(L - a_d - a_s - x))\right) \tag{4.47}$$

Substituting $\tau(L - a_d) = \tau_r$ into Eq. (4.47) leads to:

$$\cos(\lambda_2 a_s) - \frac{\lambda_2}{\lambda_1} \tanh(\lambda_1(L - a_d - a_s)) \sin(\lambda_2 a_s) - \frac{\tau_r}{\tau_p} = 0 \tag{4.48}$$

Equation (4.48) depicts the relationship between a_d and a_s. It shows that in this stage, the softening length keeps varying with the debonding length increasing. Combining Eqs. (4.45) and (4.48) together, the shear slippage of the bolt/grout interface at the position of $x = L - a_d$ can be acquired:

$$\delta(x = L - a_d) = \delta_r \tag{4.49}$$

Substituting $x = L - a_d$ *into Eq.* (4.46)*, the axial stress can be acquired:*

$$\sigma_b(x = L - a_d) = \frac{2\tau_p}{r_b}\left(\frac{1}{\lambda_1} \tanh(\lambda_1(L - a_d - a_s)) \cos(\lambda_2 a_s) + \frac{1}{\lambda_2} \sin(\lambda_2 a_s)\right) \tag{4.50}$$

For the domain $[L - a_d, L]$, the bolt/grout interface debonds and the shear stress equals τ_r:

$$\tau(x) = \tau_r \tag{4.51}$$

Also, Eq. (4.1c) can be substituted to Eq. (4.12), leading to:

$$\frac{d^2\delta(x)}{dx^2} = \lambda^2 \tau_r \tag{4.52}$$

Substituting Eqs. (4.19), (4.49) and (4.50) into Eq. (4.52) leads to:

$$\delta(x) = \delta_{\mathrm{r}} + \frac{1}{2}\lambda^2\tau_{\mathrm{r}}\left(x^2 - (L-a_{\mathrm{d}})^2\right) + \left(\frac{\tau_{\mathrm{p}}\lambda^2}{\lambda_1}\tanh(\lambda_1(L-a_{\mathrm{d}}-a_{\mathrm{s}}))\cos(\lambda_2 a_{\mathrm{s}}) + \frac{\tau_{\mathrm{p}}\lambda^2}{\lambda_2}\sin(\lambda_2 a_{\mathrm{s}}) - \lambda^2\tau_{\mathrm{r}}(L-a_{\mathrm{d}})\right)(x+a_{\mathrm{d}}-L) \tag{4.53}$$

$$\sigma_{\mathrm{b}}(x) = \frac{2\tau_{\mathrm{p}}}{r_{\mathrm{b}}}\left(\frac{1}{\lambda_1}\tanh(\lambda_1(L-a_{\mathrm{d}}-a_{\mathrm{s}}))\cos(\lambda_2 a_{\mathrm{s}}) + \frac{1}{\lambda_2}\sin(\lambda_2 a_{\mathrm{s}})\right) + \frac{2\tau_{\mathrm{r}}}{r_{\mathrm{b}}}(x+a_{\mathrm{d}}-L) \tag{4.54}$$

Substituting $x = L$ and $\sigma_{\mathrm{b}}(x = L) = \frac{F}{\pi r_{\mathrm{b}}^2}$ into Eqs. (4.53) and (4.54), the pull-out displacement and load of the rock bolt can be acquired:

$$u_{\mathrm{b}} = \delta_{\mathrm{r}} + \frac{\lambda^2 a_{\mathrm{d}}^2\tau_{\mathrm{r}}}{2} + \left(\frac{\tau_{\mathrm{p}}\lambda^2}{\lambda_1}\tanh(\lambda_1(L-a_{\mathrm{d}}-a_{\mathrm{s}}))\cos(\lambda_2 a_{\mathrm{s}}) + \frac{\tau_{\mathrm{p}}\lambda^2}{\lambda_2}\sin(\lambda_2 a_{\mathrm{s}})\right)a_{\mathrm{d}} \tag{4.55}$$

$$F = 2\pi r_{\mathrm{b}}\left(\frac{\tau_{\mathrm{p}}}{\lambda_1}\tanh(\lambda_1(L-a_{\mathrm{d}}-a_{\mathrm{s}}))\cos(\lambda_2 a_{\mathrm{s}}) + \frac{\tau_{\mathrm{p}}}{\lambda_2}\sin(\lambda_2 a_{\mathrm{s}}) + \tau_{\mathrm{r}}a_{\mathrm{d}}\right) \tag{4.56}$$

The maximum pull-out load occurs in this stage and can be acquired by solving Eqs. (4.48) and (4.56) together.

At the end of this stage, the elastic length disappears. Therefore, $L - a_{\mathrm{d}} = a_{\mathrm{s}}$. Substituting it into Eq. (4.48) leads to:

$$a_{\mathrm{s2}} = \frac{1}{\lambda_2}\arccos\left(\frac{\tau_{\mathrm{r}}}{\tau_{\mathrm{p}}}\right) \tag{4.57}$$

where a_{s2}: softening length when the elastic-softening-debonding stage ends.

4.2.3.4 Softening-Debonding Stage

After the elastic length disappears, the bolt/grout interface enters softening-debonding stage. In the domain $[0, L - a_{\mathrm{d}}]$, the bolt/grout interface softens. Substituting Eqs. (4.9), (4.19) and (4.20) and $\tau(x = L - a_{\mathrm{d}}) = \tau_{\mathrm{r}}$ into Eq. (4.34) leads to:

$$\delta(x) = \frac{\tau_{\mathrm{r}}\left(\delta_{\mathrm{p}} - \delta_{\mathrm{r}}\right)}{\left(\tau_{\mathrm{p}} - \tau_{\mathrm{r}}\right)\cos(\lambda_2(L-a_{\mathrm{d}}))}\cos(\lambda_2 x) + \frac{\tau_{\mathrm{p}}\delta_{\mathrm{r}} - \tau_{\mathrm{r}}\delta_{\mathrm{p}}}{\tau_{\mathrm{p}} - \tau_{\mathrm{r}}} \tag{4.58}$$

$$\sigma_{\mathrm{b}}(x) = \frac{2\tau_{\mathrm{r}}}{r_{\mathrm{b}}\lambda_2\cos(\lambda_2(L-a_{\mathrm{d}}))}\sin(\lambda_2 x) \tag{4.59}$$

$$\tau(x) = \frac{\tau_r}{\cos(\lambda_2(L - a_d))}\cos(\lambda_2 x) \tag{4.60}$$

Substituting $x = L - a_d$ into Eqs. (4.58) and (4.59) leads to:

$$\delta(x = L - a_d) = \delta_r \tag{4.61}$$

$$\sigma_b(x = L - a_d) = \frac{2\tau_r}{r_b\lambda_2}\tan(\lambda_2(L - a_d)) \tag{4.62}$$

For the domain $[L - a_d, L]$, the bolt/grout interface debonds. Substituting Eqs. (4.19), (4.61) and (4.62) into Eq. (4.52) leads to:

$$\begin{aligned}\delta(x) = \delta_r &+ \frac{\lambda^2\tau_r}{2}\left(x^2 - (L - a_d)^2\right) \\ &+ \left(\frac{\lambda^2\tau_r}{\lambda_2}\tan(\lambda_2(L - a_d)) - \lambda^2\tau_r(L - a_d)\right)(x + a_d - L)\end{aligned} \tag{4.63}$$

$$\sigma_b(x) = \frac{2\tau_r}{r_b}\left(\frac{\tan(\lambda_2(L - a_d))}{\lambda_2} + x + a_d - L\right) \tag{4.64}$$

Substituting $x = L$ and $\sigma_b(x = L) = \frac{F}{\pi r_b^2}$ into Eqs. (4.63) and (4.64), the pull-out displacement and load of the rock bolt can be acquired:

$$u_b = \delta_r + \lambda^2\tau_r a_d\left(\frac{a_d}{2} + \frac{\tan(\lambda_2(L - a_d))}{\lambda_2}\right) \tag{4.65}$$

$$F = 2\pi r_b\tau_r\left(\frac{\tan(\lambda_2(L - a_d))}{\lambda_2} + a_d\right) \tag{4.66}$$

At the end of this stage, the debonding length equals the full embedment length. Therefore, substituting $a_d = L$ into Eqs. (4.65) and (4.66), the pull-out displacement and load of the rock bolt at the end of the softening-debonding stage can be acquired:

$$u_{b0} = \delta_r + \frac{\lambda^2\tau_r L^2}{2} \tag{4.67}$$

$$F_0 = 2\pi r_b\tau_r L \tag{4.68}$$

where u_{b0}: pull-out displacement of the rock bolt at the end of the softening-debonding stage; and F_0: pull-out load of the rock bolt at the end of the softening-debonding stage.

4.2.3.5 Debonding Stage

After the softening length disappears, the bolt/grout interface enters debonding stage. Since the full bolt/grout interface undergoes debonding, the relationship between the pull-out load and displacement can be expressed as:

$$F_0 - F = 2\pi r_b \tau_r (u_b - u_{b0}) \tag{4.69}$$

Substituting Eqs. (4.67) and (4.68) into Eq. (4.69) leads to:

$$F = 2\pi r_b \tau_r \left(L + \delta_r + \frac{\lambda^2 \tau_r L^2}{2} - u_b \right) \tag{4.70}$$

4.3 Calibration of the Input Parameters

In this analytical model, the mechanical properties of the rock bolt and the confining medium, such as r_b, E_b and E_m, can be acquired based on the rock bolt pull-out scenario. Specifically, r_b and E_b can be acquired from the rock bolt specification provided by the bolt manufacturer. E_m can be acquired by conducting uniaxial compressive strength tests on samples cored from the confining medium.

As for the mechanical properties of the bond-slip model, they can be calibrated from the experimental load–displacement results. Figure 4.6 shows a typical load–displacement curve of rock bolts.

In the initial stage of the load–displacement curve, the pull-out load of the rock bolt generally had a linear relationship with the pull-out displacement. Therefore, Point

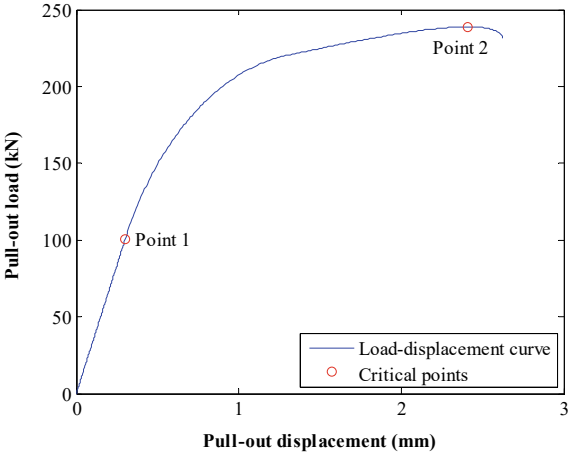

Fig. 4.6 Selecting critical points to calibrate the input bond-slip parameters

1 represents the point where the linear relationship of the pull-out load and displacement ends in the load–displacement curve. Then, δ_p equals the pull-out displacement at Point 1. Also, F_{sof} equals the pull-out load at Point 1. Substituting F_{sof} and δ_p into Eq. (4.26), τ_p can be acquired.

When the rock bolt reaches the maximum pull-out load, that point can be selected as Point 2, as shown in Fig. 4.6. Then, δ_r can be selected in the range between the pull-out displacement at Point 1 and the pull-out displacement at Point 2. Then, τ_r can be calibrated until the maximum analytical pull-out load fits well with the maximum experimental pull-out load.

4.4 Validation of the Analytical Model

In this section, two experimental pull-out tests were used to validate the credibility of this analytical model.

4.4.1 Validation with a Pull-Out Test

Bai et al. [58] conducted experimental in situ pull-out tests on rock bolts. Specifically, rock bolts with a radius of 14 mm were tested and the embedment length was 3 m. The surrounding rock mass had an elastic modulus of 6 GPa.

The mechanical properties of the rock bolt and the confining medium used in this analytical model are tabulated in Table 4.1.

As for the input parameters for the bond-slip model, they can be calibrated from experimental pull-out results, following the methods indicated in Sect. 4.3. Then, the parameters tabulated in Table 4.2 were used in this paper to analytically model the load transfer performance of rock bolts.

A comparison between the experimental result and the analytical result is shown in Fig. 4.7. There is a close match between the experimental result and the analytical result, confirming the credibility of this analytical model.

Table 4.1 Mechanical properties of the bolt and the confining medium

r_b (mm)	E_b (GPa)	L (m)	E_m (GPa)	A_m (m^2)
14	51	3	6	1

Table 4.2 Input parameters for the bond-slip model

τ_p (MPa)	δ_p (mm)	τ_r (MPa)	δ_r (mm)
2.2	3.57	1	8.91

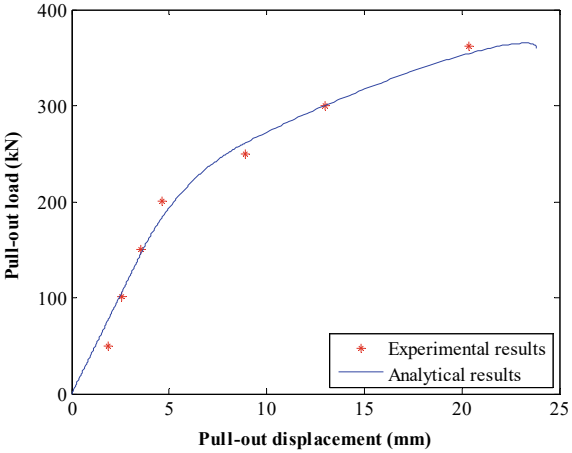

Fig. 4.7 Comparison between the experimental result acquired from Bai et al. [58] and the analytical result

4.4.2 Validation with the Other Pull-Out Test

Stillborg [59] conducted a number of pull-out tests in the mine site to study the load transfer performance of cable bolts. Cable bolts with a long embedment length of 10 m were tested. The cable bolts had a radius of 19 mm and elastic modulus of 83 GPa. The surrounding rock mass had an elastic modulus of 57 GPa. The mechanical properties of the rock bolt and the confining medium used in this analytical model are tabulated in Table 4.3.

As for the input parameters for the bond-slip model, they can be calibrated from the experimental pull-out results. In this paper, the parameters tabulated in Table 4.4 were used to calculate the load–displacement relationship of the cable bolt.

The comparison between the experimental result and the analytical result is shown in Fig. 4.8. It shows that the analytical result agrees well with the experimental result, further confirming that this analytical model can be used to simulate the load transfer performance of rock bolts.

Table 4.3 Mechanical properties of the cable bolt and the confining medium

r_b (mm)	E_b (GPa)	L (m)	E_m (GPa)	A_m (m^2)
19	83	10	57	1

Table 4.4 Input parameters for the bond-slip model

τ_p (MPa)	δ_p (mm)	τ_r (MPa)	δ_r (mm)
1.34	10.37	0.47	35.02

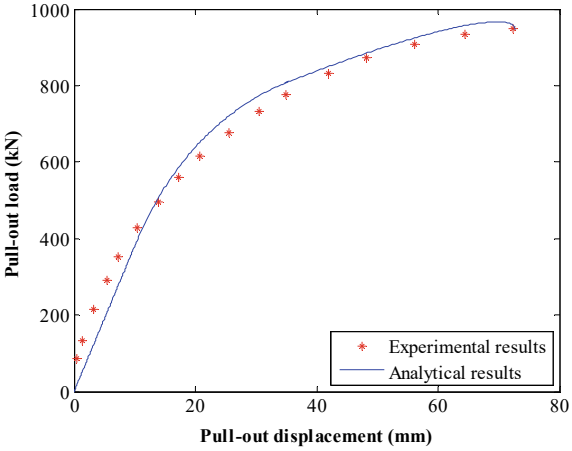

Fig. 4.8 Comparison between the experimental result acquired from Stillborg [59] and the analytical result

4.5 Parametric Study

A parametric study was conducted to evaluate the input parameters on the load transfer performance of rock bolts. Specifically, the influence of the elastic modulus of the confining medium, the shear strength of the bolt/grout interface and the shear slippage where shear strength of the bolt/grout interface reaches on the load transfer performance of rock bolts were studied.

4.5.1 Elastic Modulus of the Confining Medium

To study the influence of the elastic modulus of the confining medium on the load transfer performance of rock bolts, an analytical rock bolt pull-out scenario was created. A rock bolt with a radius of 10 mm was tested. The elastic modulus of the rock bolt and the embedment length were 196 GPa and 1.5 m. Then, the mechanical properties of the bolt and the confining medium are tabulated in Table 4.5. As for the input parameters for the bond-slip model, they are tabulated in Table 4.6.

The elastic modulus of the confining medium was changed from 10 to 90 MPa and the load–displacement performance of rock bolts was calculated, as shown in Fig. 4.9. It shows that the elastic modulus of the confining medium had an apparent

Table 4.5 Mechanical properties of the bolt and the confining medium

r_b (mm)	E_b (GPa)	L (m)	E_m (MPa)	A_m (m^2)
10	196	1.5	10	1
			50	
			90	

Table 4.6 Input parameters for the bond-slip model

τ_p (MPa)	δ_p (mm)	τ_r (MPa)	δ_r (mm)
2	1.5	0.8	3.5

influence on the load transfer performance of rock bolts. The initial stiffness and the peak load of the rock bolting system increased with the elastic modulus of the confining medium.

This finding agrees well with previous research. Hyett et al. [60] conducted laboratory and in situ pull-out tests on plain cable bolts. In the laboratory, PVC, aluminium and steel pipes were used to confine cable bolts. The results showed that the peak load of cable bolts increased with the elastic modulus of the confining medium. As for the in situ case, cable bolts were pulled from shale, limestone and granite. The results showed that when the confining medium changed from shale to granite, the peak load of cable bolts increased apparently.

Figure 4.9 also shows that with the elastic modulus of the confining medium increasing, the increasing rate of the peak load was not constant. To further study the influence of the elastic modulus of the confining medium on the peak load, a series of analytical pull-out tests was conducted. The relationship between the rock bolt peak load and the elastic modulus of the confining medium was acquired, as shown in Fig. 4.10.

It shows that for this scenario, before the elastic modulus of the confining medium increased to 280 MPa, the peak load increases rapidly. After that, the peak load is still increasing but with a much lower slope. This indicates that when the elastic modulus of the confining medium was higher than a critical limit, it had marginal effect on the peak load of rock bolts.

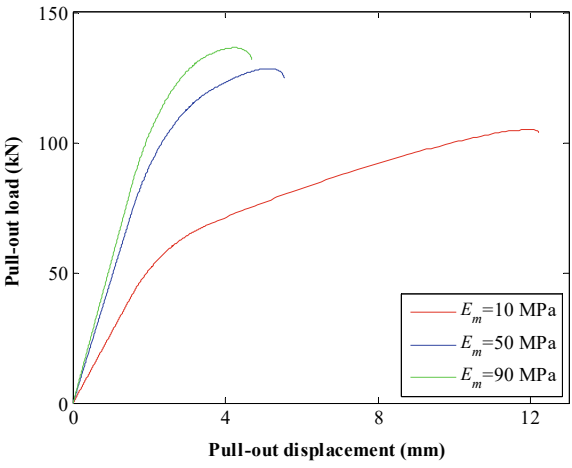

Fig. 4.9 Influence of elastic modulus of the confining medium on the performance of rock bolts

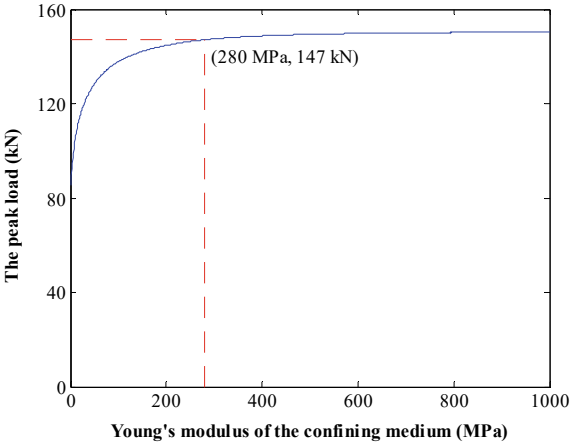

Fig. 4.10 Influence of the elastic modulus of the confining medium on the peak load of rock bolts

4.5.2 Shear Strength of the Bolt/Grout Interface

To study the influence of the shear strength of the bolt/grout interface on the load transfer performance of rock bolts, three analytical pull-out tests were conducted. In this case, the shear strength of the bolt/grout interface was varied from 2 to 6 MPa. As for the other parameters, they were kept constant.

The mechanical properties for the rock bolt and the confining medium are tabulated in Table 4.7. As for the input parameters for the bond-slip model, they are tabulated in Table 4.8.

A plot of the input bond-slip model is shown in Fig. 4.11. Based on the input bond-slip model, the calculated load transfer performance of rock bolts is shown in Fig. 4.12.

The results show that the shear strength of the bolt/grout interface played a significant role in determining the load transfer performance of rock bolts. Specifically, when the shear strength of the bolt/grout interface was 2 MPa, the rock bolt had a maximum pull-out load of 146 kN when the pull-out displacement reached 3.1 mm.

Table 4.7 Mechanical properties of the bolt and the confining medium

r_b (mm)	E_b (GPa)	L (m)	E_m (GPa)	A_m (m^2)
10	196	1.5	1	1

Table 4.8 Input parameters for the bond-slip model

τ_p (MPa)	δ_p (mm)	τ_r (MPa)	δ_r (mm)
2	1.5	0.5	3.5
4			
6			

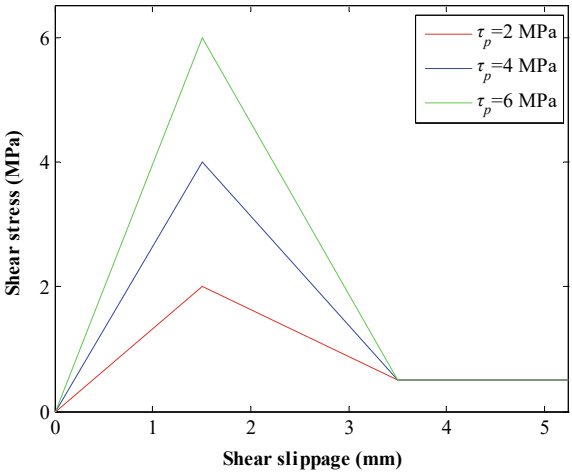

Fig. 4.11 A plot of the input bond-slip model when the shear strength of the bolt/grout interface was different

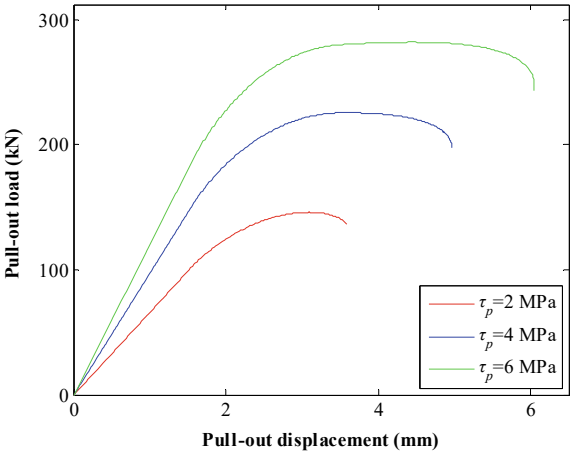

Fig. 4.12 Load transfer performance of rock bolts when the shear strength of the bolt/grout interface was different

Compared with that, when the shear strength of the bolt/grout interface was 6 MPa, the rock bolt had a maximum pull-out load of 282 kN, increasing by 93.2%. And the corresponding pull-out displacement reached 4.5 mm. Apparently, the larger the shear strength of the bolt/grout interface, the higher the maximum load transfer capacity of rock bolts.

Furthermore, the results show that the shear strength of the bolt/grout interface also had an effect in the initial stiffness of the rock bolting system. With the shear strength of the bolt/grout interface increasing, the initial stiffness of the rock bolting system also increased, as shown in Fig. 4.12.

4.5.3 Residual Shear Strength of the Bolt/Grout Interface

To study the influence of the residual shear strength of the bolt/grout interface on the load transfer performance of rock bolts, another rock bolt pull-out scenario was created. In this case, the residual shear strength of the bolt/grout interface was varied from 0.5 to 1.5 MPa. As for the other parameters, they were kept constant.

The mechanical properties of the rock bolt and the confining medium are tabulated in Table 4.9. As for the input parameters for the bond-slip model, they are tabulated in Table 4.10.

A plot of the input bond-slip model is shown in Fig. 4.13. As for the load transfer performance of rock bolts, they are shown in Fig. 4.14.

The results show that the residual shear strength of the bolt/grout interface had no effect on the initial stiffness of the rock bolting system. For example, in this case, when the residual shear strength of the bolt/grout interface increased from 0.5 to 1.5 MPa, the initial stiffness of the rock bolting system kept constant.

Nevertheless, the residual shear strength of the bolt/grout interface had an effect on the maximum load transfer capacity of rock bolts. For example, in this scenario, when the residual shear strength of the bolt/grout interface was 0.5 MPa, the maximum pull-out load of rock bolts was 226 kN and the corresponding pull-out displacement was 3.6 mm. Then, when the residual shear strength of the bolt/grout interface increased to 1.5 MPa, the maximum pull-out load of rock bolts increased to 256 kN, increasing by 13.3%. And the corresponding pull-out displacement was 4.9 mm. Apparently, increasing the residual shear strength of the bolt/grout interface was beneficial for improving the maximum load transfer capacity of rock bolts.

Additionally, compared with the shear strength of the bolt/grout interface, increasing the residual shear strength of the bolt/grout interface had less apparent effect in improving the maximum load transfer capacity of rock bolts. For example, in the above analysis, when the residual shear strength of the bolt/grout interface increased by 200%, the maximum pull-out load of rock bolts only increased by 13.3%. However, when the shear strength of the bolt/grout interface increased by

Table 4.9 Mechanical properties of the bolt and the confining medium

r_b (mm)	E_b (GPa)	L (m)	E_m (GPa)	A_m (m^2)
10	196	1.5	1	1

Table 4.10 Input parameters for the bond-slip model

τ_p (MPa)	δ_p (mm)	τ_r (MPa)	δ_r (mm)
4	1.5	0.5	3.5
		1	
		1.5	

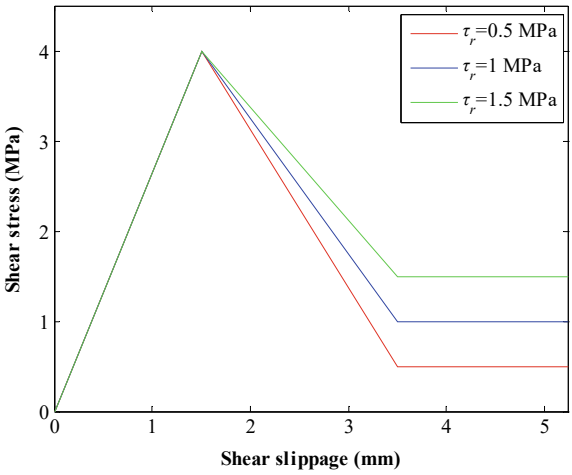

Fig. 4.13 A plot of the input bond-slip model when the residual shear strength of the bolt/grout interface was different

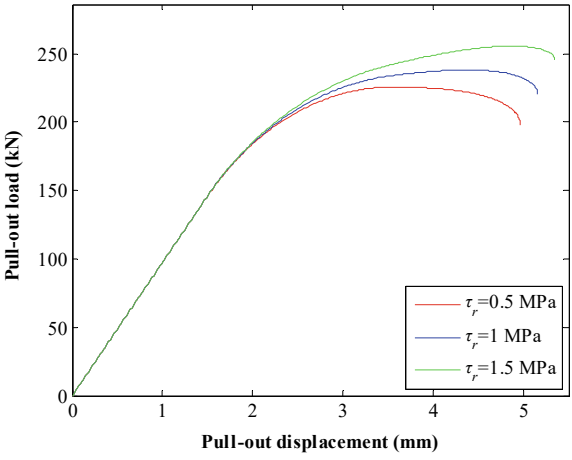

Fig. 4.14 Load transfer performance of rock bolts when the residual shear strength of the bolt/grout interface was different

200%, the maximum pull-out load of rock bolts largely increased by 93.2%. Therefore, the shear strength of the bolt/grout interface had more significant effect in deciding the maximum load transfer capacity of rock bolts.

The contribution of this paper is that it concentrated on fully grouted rock bolts with long embedment length grouted in the surrounding confining medium. Specifically, based on the previous work [38, 47], this paper acquired the specific analytical solution for this scenario. Furthermore, based on the acquired specific analytical solution, it further studied the influence of the elastic modulus of the confining medium on the load transfer performance of rock bolts. It revealed that although the peak load of rock bolts increased with the elastic modulus of the confining medium, there was a critical limit. Once the elastic modulus of the confining medium was beyond that critical limit, it had marginal effect on the peak load of rock bolts.

4.6 Conclusions

A tri-linear model was adopted to depict the bond-slip behaviour of the bolt/grout interface. It was assumed that the shear stress of the bolt/grout interface increased linearly to the shear strength of the bolt/grout interface with the shear slippage. Then, the shear stress decreased linearly to the residual shear strength of the bolt/grout interface with the shear slippage. After that, the shear stress was kept constant.

The pull-out stages of rock bolts were analysed. During the pull-out process, the bolt/grout interface underwent elastic, elastic-softening, elastic-softening-debonding, softening-debonding and debonding stages.

Experimental pull-out tests were used to validate the credibility of this analytical model. The results show that there was a good correlation between experimental and analytical results.

A parametric study was conducted to evaluate the elastic modulus of the confining medium, the shear strength of the bolt/grout interface and the residual shear strength of the bolt/grout interface on the load transfer performance of rock bolts. The results show that increasing the elastic modulus of the confining medium was beneficial for improving the load transfer performance of rock bolts. However, once the elastic modulus of the confining medium was beyond a critical limit, it had a marginal effect on the peak load of rock bolts. Additionally, increasing the shear strength of the bolt/grout interface and the residual shear strength of the bolt/grout interface led to rising of the peak load of rock bolts. However, compared with the residual shear strength of the bolt/grout interface, increasing the shear strength of the bolt/grout interface had more apparent effect in improving the load transfer capacity of rock bolts.

References

1. N. Vlachopoulos, D. Cruz, B. Forbes, Utilizing a novel fiber optic technology to capture the axial responses of fully grouted rock bolts. J. Rock Mech. Geotech. Eng. **10**, 222–235 (2018). https://doi.org/10.1016/j.jrmge.2017.11.007
2. B. Meng, H. Jing, S. Yang, Y. Wang, B. Li, Experimental study on the shear behaviour of bolted concrete blocks with oblique shear test. Adv. Civ. Eng. **2018**, 1–8 (2018). https://doi.org/10.1155/2018/7281218
3. H. Wang, Q. Wang, F. Wang, S. Li, D. Wang, Y. Ren, N. Guo, S. Zhang, Mechanical effect analysis of bolts in roadway under different anchoring lengths and its application. J. China Coal Soc. **40**(3), 509–515 (2015)
4. Y. Yokota, Z. Zhao, J. Shang, W. Nie, K. Date, K. Iwano, Effect of bolt configuration on the interface behaviour between a rock bolt and bond material: a comprehensive DDA investigation. Comput. Geotech. **105**, 116–128 (2019). https://doi.org/10.1016/j.compgeo.2018.09.017
5. Z. Zhang, W. Wang, S. Li, J. Bai, S. Hao, H. Wu, X. Yu, An innovative approach for gob-side entry retaining with thick and hard roof: a case study. Tech. Gaz. **25**(4), 1028–1036 (2018). https://doi.org/10.17559/TV-20160816155022
6. Z. Zhang, X. Yu, H. Wu, M. Deng, Stability control for gob-side entry retaining with super-critical retained entry width in thick coal seam longwall mining. Energies **12**(7), 1–16 (2019). https://doi.org/10.3390/en12071375

7. C.R. Windsor, Rock reinforcement systems. Int. J. Rock Mech. Min. Sci. **34**(6), 919–951 (1997). https://doi.org/10.1016/S1365-1609(97)80004-4
8. Y. Wang, Y. Gao, E. Wang, M. He, J. Yang, Roof deformation characteristics and preventive techniques using a novel non-pillar mining method of gob-side entry retaining by roof cutting. Energies **11**(3), 1–17 (2018). https://doi.org/10.3390/en11030627
9. D. Hou, X. Yang, Physical modeling of displacement and failure monitoring of underground roadway in horizontal strata. Adv. Civ. Eng. **2018**, 1–11 (2018). https://doi.org/10.1155/2018/2934302
10. A.G. Thompson, E. Villaescusa, C.R. Windsor, Ground support terminology and classification: an update. Geotech. Geol. Eng. **30**(3), 553–580 (2012). https://doi.org/10.1007/s10706-012-9495-4
11. S. Ma, Z. Zhao, W. Nie, Y. Gui, A numerical model of fully grouted bolts considering the tri-linear shear bond-slip model. Tunn. Undergr. Space Technol. **54**, 73–80 (2016). https://doi.org/10.1016/j.tust.2016.01.033
12. J. Chen, P.C. Hagan, S. Saydam, Sample diameter effect on bonding capacity of fully grouted cable bolts. Tunn. Undergr. Space Technol. **68**, 238–243 (2017). https://doi.org/10.1016/j.tust.2017.06.004
13. J. Chen, S. Saydam, P.C. Hagan, An analytical model of the load transfer behaviour of fully grouted cable bolts. Constr. Build. Mater. **101**, 1006–1015 (2015). https://doi.org/10.1016/j.conbuildmat.2015.10.099
14. A. Mirzaghorbanali, H. Rasekh, N. Aziz, G. Yang, S. Khaleghparast, J. Nemcik, Shear strength properties of cable bolts using a new double shear instrument, experimental study, and numerical simulation. Tunn. Undergr. Space Technol. **70**, 240–253 (2017). https://doi.org/10.1016/j.tust.2017.07.018
15. M.L. Jeremic, G.J.P. Delaire, Failure mechanics of cable bolt systems. CIM Bull. **76**(856), 66–71 (1983)
16. D.J. Hutchinson, M.S. Diederichs, *Cablebolting in Underground Mines* (BiTech Publishers Ltd., Richmond, 1996)
17. X. Feng, N. Zhang, S. Yang, F. He, Mechanical response of fully bonded bolts under cyclic load. Int. J. Rock Mech. Min. Sci. **109**, 138–154 (2018). https://doi.org/10.1016/j.ijrmms.2018.06.018
18. H. Jalalifar, *A New Approach in Determining the Load Transfer Mechanism in Fully Grouted Bolts* (University of Wollongong, Wollongong, 2006)
19. J. Chen, P.C. Hagan, S. Saydam, Load transfer behaviour of fully grouted cable bolts reinforced in weak rocks under tensile loading conditions. Geotech. Test. J. **39**(2), 252–263 (2016). https://doi.org/10.1520/GTJ20150096
20. J. Chai, Q. Liu, J. Liu, G. Zhang, D. Zhang, F. Qiu, Assessing the difference in measuring bolt stress: a comparison of two optical fiber sensing techniques. J. Sens. **2018**, 1–11 (2018). https://doi.org/10.1155/2018/7582605
21. P.G. Gambarova, On aggregate interlock mechanism in reinforced concrete plates with extensive cracking, vol. 34. IABSE Reports of the Working Commissions (1981), pp. 99–120
22. S. Ma, N. Aziz, J. Nemcik, A. Mirzaghorbanali, The effects of installation procedure on bond characteristics of fully grouted rock bolts. Geotech. Test. J. **40**(5), 846–857 (2017). https://doi.org/10.1520/GTJ20160239
23. T. Wu, C. Cao, J. Han, T. Ren, Effect of bolt rib spacing on load transfer mechanism. Int. J. Min. Sci. Technol. **27**, 431–434 (2017). https://doi.org/10.1016/j.ijmst.2017.03.009
24. C.C. Li, G. Kristjansson, A.H. Høien, Critical embedment length and bond strength of fully encapsulated rebar rockbolts. Tunn. Undergr. Space Technol. **59**, 16–23 (2016). https://doi.org/10.1016/J.TUST.2016.06.007
25. A. Mortazavi, Anchorage and shear strength properties for composite tendons used in earthwork support systems. Constr. Build. Mater. **21**(1), 109–117 (2007). https://doi.org/10.1016/j.conbuildmat.2005.06.034
26. J.M. Hawkes, R.H. Evans, Bond stresses in reinforced concrete columns and beams. Struct. Eng. **29**, 323–327 (1951)

27. I.W. Farmer, Stress distribution along a resin grouted rock anchor. Int. J. Numer. Anal. Meth. Geomech. **12**, 347–351 (1975). https://doi.org/10.1016/0148-9062(75)90168-0
28. O. Aydan, Y. Ichikawa, K. Kawamoto, Load bearing capacity and stress distributions in/along rockbolts with inelastic behaviour of interfaces, in *Fifth International Conference on Numerical Methods in Geomechanics*, Nagoya, Japan (1985), pp. 1281–1292
29. H. Rajaie, *Experimental and Numerical Investigations of Cable Bolt Support Systems* (McGill University, Montreal, 1990)
30. S. Yazici, P.K. Kaiser, Bond strength of grouted cable bolts. Int. J. Rock Mech. Min. Sci. **29**(3), 279–292 (1992). https://doi.org/10.1016/0148-9062(92)93661-3
31. P.K. Kaiser, S. Yazici, J.-P. Nosé, Effect of stress change on the bond strength of fully grouted cables. Int. J. Rock Mech. Min. Sci. **29**(3), 293–306 (1992). https://doi.org/10.1016/0148-9062(92)93662-4
32. A.J. Hyett, W.F. Bawden, G.R. Macsporran, M. Moosavi, A constitutive law for bond failure of fully-grouted cable bolts using a modified Hoek cell. Int. J. Numer. Anal. Meth. Geomech. **32**(1), 11–36 (1995). https://doi.org/10.1016/0148-9062(94)00018-X
33. A.J. Hyett, M. Moosavi, W.F. Bawden, Load distribution along fully grouted bolts, with emphasis on cable bolt reinforcement. Int. J. Numer. Anal. Meth. Geomech. **20**(7), 517–544 (1996). https://doi.org/10.1002/(SICI)1096-9853(199607)20:73.0.CO;2-L
34. M. Moosavi, A comprehensive comparison between bond failure mechanism in rock bolts and cable bolts, in *The Congress of the International Society for Rock Mechanics* (1999), pp. 1463–1466
35. C.C. Li, B. Stillborg, Analytical models for rock bolts. Int. J. Rock Mech. Min. Sci. **36**, 1013–1029 (1999). https://doi.org/10.1016/S1365-1609(99)00064-7
36. Y. Cai, T. Esaki, Y. Jiang, An analytical model to predict axial load in grouted rock bolt for soft rock tunnelling. Tunn. Undergr. Space Technol. **19**(6), 607–618 (2004). https://doi.org/10.1016/j.tust.2004.02.129
37. S. Xiao, C. Chen, Mechanical mechanism analysis of tension type anchor based on shear displacement method. J. Cent. South Univ. Technol. **15**(2008), 106–111 (2008). https://doi.org/10.1007/s11771-008-0021-z
38. F. Ren, Z.J. Yang, J.F. Chen, W.W. Chen, An analytical analysis of the full-range behaviour of grouted rockbolts based on a tri-linear bond-slip model. Constr. Build. Mater. **24**(3), 361–370 (2010). https://doi.org/10.1016/j.conbuildmat.2009.08.021
39. L. Blanco Martín, M. Tijani, F. Hadj-Hassen, A new analytical solution to the mechanical behaviour of fully grouted rockbolts subjected to pull-out tests. Constr. Build. Mater. **25**(2), 1–18 (2010). https://doi.org/10.1016/j.conbuildmat.2010.07.011
40. H. Jalalifar, An analytical solution to predict axial load along fully grouted bolts in an elasto-plastic rock mass. J. South. Afr. Inst. Min. Metall. **111**(11), 809–814 (2011). https://doi.org/10.3724/SP.J.1037.2011.00325
41. C. Cao, J. Nemcik, N. Aziz, T. Ren, Analytical study of steel bolt profile and its influence on bolt load transfer. Int. J. Rock Mech. Min. Sci. **60**, 188–195 (2013). https://doi.org/10.1016/j.ijrmms.2012.12.013
42. S. Ma, J. Nemcik, N. Aziz, An analytical model of fully grouted rock bolts subjected to tensile load. Constr. Build. Mater. **49**, 519–526 (2013). https://doi.org/10.1016/j.conbuildmat.2013.08.084
43. S. Ma, J. Nemcik, N. Aziz, Z. Zhang, Analytical model for rock bolts reaching free end slip. Constr. Build. Mater. **57**, 30–37 (2014). https://doi.org/10.1016/j.conbuildmat.2014.01.057
44. D. Li, H. Masoumi, S. Saydam, P.C. Hagan, A constitutive model for load-displacement performance of modified cable bolts. Tunn. Undergr. Space Technol. **68**, 95–105 (2017). https://doi.org/10.1016/j.tust.2017.05.025
45. D.D. Faulkner, The development and application of polyurethane injectable cable bolts, in *International Conference on Ground Control in Mining, ICGCM*, Morgantown, USA, ed. by S.S. Peng (2012), pp. 1–5
46. B. Benmokrane, A. Chennouf, H.S. Mitri, Laboratory evaluation of cement-based grouts and grouted rock anchors. Int. J. Rock Mech. Min. Sci. **32**(7), 633–642 (1995). https://doi.org/10.1016/0148-9062(95)00021-8

47. J. Vaculik, A.B. Sturm, P. Visintin, M.C. Griffith, Modelling FRP-to-substrate joints using the bilinear bond-slip rule with allowance for friction-full-range analytical solutions for long and short bonded lengths. Int. J. Solids Struct. **135**, 245–260 (2018). https://doi.org/10.1016/j.ijsolstr.2017.11.024
48. A. Teymen, A. Kilic, Effect of grout strength on the stress distribution (tensile) of fully-grouted rockbolts. Tunn. Undergr. Space Technol. **77**, 280–287 (2018). https://doi.org/10.1016/j.tust.2018.04.022
49. S. Ding, H. Jing, K. Chen, G. Xu, B. Meng, Stress evolution and support mechanism of a bolt anchored in a rock mass with a weak interlayer. Int. J. Min. Sci. Technol. **27**(3), 573–580 (2017). https://doi.org/10.1016/J.IJMST.2017.03.024
50. M. Bastamia, K. Shahriar, M. Ghadimi, Verification of the analytical model for fully grouted rock bolts based on pull-out test (case study: Tabas Coal Mine). Procedia Eng. **191**, 1068–1074 (2017). https://doi.org/10.1016/j.proeng.2017.05.280
51. C. Cao, J. Nemcik, T. Ren, N. Aziz, A study of rock bolting failure modes. Int. J. Min. Sci. Technol. **23**(1), 79–88 (2013). https://doi.org/10.1016/j.ijmst.2013.01.012
52. J. Zhang, B. Tang, Hyperbolic function model to analyze load transfer mechanism on bolts. Chin. J. Geotech. Eng. **24**(2), 188–192 (2002)
53. H. Yuan, J.G. Teng, R. Seracino, Z.S. Wu, J. Yao, Full-range behavior of FRP-to-concrete bonded joints. Eng. Struct. **26**(5), 553–565 (2004). https://doi.org/10.1016/j.engstruct.2003.11.006
54. Z. Tao, J. Chen, Behaviour of rock bolting as tunnelling support, in *Proceedings of the International Symposium on Rock Bolting*, ed. by O. Stephansson (A.A. Balkema, Abisko, Sweden, 1983), pp. 87–92
55. Y. Cai, T. Esaki, Y. Jiang, A rock bolt and rock mass interaction model. Int. J. Rock Mech. Min. Sci. **41**, 1055–1067 (2004). https://doi.org/10.1016/j.ijrmms.2004.04.005
56. L. Blanco Martín, M. Tijani, F. Hadj-Hassen, A. Noiret, Assessment of the bolt-grout interface behaviour of fully grouted rockbolts from laboratory experiments under axial loads. Int. J. Rock Mech. Min. Sci. **63**, 50–61 (2013). https://doi.org/10.1016/j.ijrmms.2013.06.007
57. Z. Wu, S. Yang, J. Zheng, X. Hu, Analytical solution for the pull-out response of FRP rods embedded in steel tubes filled in cement grout. Mater. Struct. **43**(2010), 597–609 (2010). https://doi.org/10.1617/s11527-009-9515-x
58. X. Bai, M. Zhang, N. Yan, Field contrast test and mechanism analysis on anchorage performance of anti-floating anchors with two different materials. China Civ. Eng. J. **48**(8), 38–46, 59 (2015). https://doi.org/10.15951/j.tmgcxb.2015.08.005
59. B. Stillborg, *Experimental Investigation of Steel Cables for Rock Reinforcement in Hard Rock* (Luleå University, Luleå, 1984)
60. A.J. Hyett, W.F. Bawden, R.D. Reichert, The effect of rock mass confinement on the bond strength of fully grouted cable bolts. Int. J. Rock Mech. Min. Sci. **29**(5), 503–524 (1992). https://doi.org/10.1016/0148-9062(92)92634-O

Chapter 5
Analytical Studying the Confining Medium Diameter Impact on Load-Carrying Capacity of Rock Bolts

5.1 Introduction

Rock bolts are tendons or cables that are commonly used in mining engineering and civil engineering to reinforce excavated rock masses or soils [1, 2]. Numerous in situ tests proved that rock bolts are efficient in improving the internal strength of the surrounding confining medium, namely rock masses and soils [3]. Therefore, rock bolts are becoming more significant in maintaining the stability of underground roadways, chambers, tunnels, surface slopes [4] and rooms in the room and pillar mining [5]. In the fully grouted rock bolting system, the bolt can deform consistently with the confining medium [6, 7]. Then, the bolt tendon can interact with the confining medium to transfer the force [8, 9].

To investigate the load-carrying capacity of rock bolts, laboratory pull-out tests were the most widely preferred method [10]. Specifically, a natural or artificial rock block can be prepared as the confining medium. Then, the bolt was installed in the drilled hole in the rock block. Cement-based or resin grout was poured into the drilled hole to bond the bolt and rock block. After the grout in the bolting hole fully cured, the bolt was pulled out from the rock block. During the experiment, load cell and displacement transducers were adopted to monitor the pull-out force and displacement. With the recorded data, the force–displacement relationship of rock bolts can be plotted, representing the performance of rock bolts. For example, Skrzypkowski et al. [11] considered that the load-carrying capacity of segmentally installed rock bolts can be influenced by the bolting hole diameter. To investigate this impact, they conducted pull-out tests on rock bolts with a diameter of 24 mm. Four different bolting hole diameters were used, ranging from 28 to 37 mm. The results showed that at the certain installing length of 100 mm and 200 mm, the maximum load-carrying capacity of rock bolts varied with the bolting hole diameter. Moreover, it was concluded that the optimum load-carrying capacity appeared when the bolting hole diameter was 32 mm.

J. Chen et al., *Bond Failure Mechanism of Fully Grouted Rock Bolts*,
SpringerBriefs in Applied Sciences and Technology,
https://doi.org/10.1007/978-981-99-0498-3_5

The previous research work showed that in the laboratory tests, the geometry of the rock block was different. Usually, researchers would like to prefer cylindrical or cubic rock blocks. However, it was more common to use cylindrical rock blocks [12, 13]. It is interesting to see that although researchers used this method to study the performance of rock bolts, the diameter of rock blocks was largely different. For laboratory tests, the diameter of rock blocks usually ranged from 100 to 500 mm [14]. The previous researchers conducted a number of tests to reveal the loading performance of rock bolts when the condition of the bolt, grout and rock masses varied [15–17]. However, less attention was paid to evaluate the confining medium diameter effect on load-carrying capacity of rock bolts.

Rajaie [18] was the pioneer to study the confining medium diameter effect. Moreover, he used concrete materials to cast cylindrical samples. Five different sample diameters were used: 100 mm, 150 mm, 200 mm, 250 mm and 300 mm. The results showed that when the confining medium diameter was small, the peak force of rock bolts ascended rapidly with the confining medium diameter ascending. However, it almost stopped ascending once the diameter was beyond 200 mm. This indicated that there was a critical influence diameter. Once the rock block diameter was larger than this critical influence diameter, further ascending the rock block diameter had marginal effect on the performance of rock bolts. Chen et al. [19] continued this experimental work, finding that the boundary condition had an effect in determining the critical influence diameter.

Although numerous analytical models were proposed to study the performance of rock bolts [20–23], little work has been focused on the confining medium diameter effect. Therefore, this paper conducted an analytical study to investigate the influence of the confining medium diameter on the load-carrying capacity of rock bolts. First, the analytical model concept was illustrated. Then, the confining medium diameter effect was studied with this analytical model, and the results were compared with experimental results. Last, the influence of the confining medium modulus on the critical influence diameter was analysed.

5.2 Analytical Modelling Approach

The authors of this paper previously deduced an analytical model to study the loading performance of rock bolts [24]. Specifically, after the rock bolt was loaded, shearing stress occurred at the bonding face between the tendon and grout. Moreover, shearing stress occurred at the bonding face between the grout and confining medium, as shown in Fig. 5.1.

Then, a tri-linear formula was used to illustrate the bonding and debonding behaviour of the bonding face, as shown in Eqs. (5.1a–5.1c) [25]:

$$\tau = \frac{\tau_{\mathrm{p}}}{\delta_{\mathrm{p}}}\delta\left(0 \le \delta \le \delta_{\mathrm{p}}\right) \tag{5.1a}$$

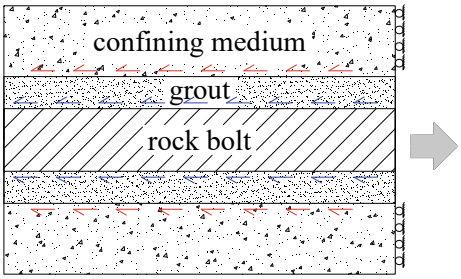

Fig. 5.1 State of the bolting system after the bolt was loaded

$$\tau = \frac{\tau_{\mathrm{p}}\delta_{\mathrm{r}} - \tau_{\mathrm{r}}\delta_{\mathrm{p}}}{\delta_{\mathrm{r}} - \delta_{\mathrm{p}}} - \frac{\tau_{\mathrm{p}} - \tau_{\mathrm{r}}}{\delta_{\mathrm{r}} - \delta_{\mathrm{p}}}\delta\left(\delta_{\mathrm{p}} < \delta \leq \delta_{\mathrm{r}}\right) \tag{5.1b}$$

$$\tau = \tau_{\mathrm{r}}(\delta > \delta_{\mathrm{r}}) \tag{5.1c}$$

Then, through analysing the equilibrium relationship between the tensile stress in the tendon and shearing stress at the bonding face, the governing equation for the bolting system was obtained [24]:

$$\frac{\mathrm{d}^2 s(x)}{\mathrm{d}x^2} - \lambda^2 \tau(x) = 0 \tag{5.2}$$

$$\lambda^2 = \frac{4}{D_{\mathrm{b}}}\left(\frac{1}{E_{\mathrm{b}}} + \frac{A_{\mathrm{b}}}{E_{\mathrm{m}}A_{\mathrm{m}}}\right) \tag{5.3}$$

The whole pull-out process of rock bolts was divided into five different phases, including the elastic phase (I), the elastic-softening phase (II), the elastic-softening-debonding phase (III), the softening-debonding phase (IV) and the debonding phase (V) [26]. Through substituting the tri-linear formula and boundary condition in each phase into Eq. (5.2), the relationship between the pull-out force and displacement can be obtained.

Specifically, in Phase I, the pull-out force and displacement can be computed as follows:

$$F = \frac{\pi D_{\mathrm{b}}\tau_{\mathrm{p}}\tanh(\lambda_1 L)}{\lambda_1 s_{\mathrm{p}}} u_{\mathrm{b}} \tag{5.4}$$

$$\lambda_1^2 = \frac{\tau_{\mathrm{p}}}{s_{\mathrm{p}}}\lambda^2 \tag{5.5}$$

In Phase II, the pull-out force and displacement can be computed as follows:

$$u_{\mathrm{b}} = \frac{\lambda_1 s_{\mathrm{p}}}{\lambda_2}\tanh(\lambda_1(L - a_{\mathrm{s}}))\sin(\lambda_2 a_{\mathrm{s}}) - \frac{\lambda_1^2 s_{\mathrm{p}}}{\lambda_2^2}\cos(\lambda_2 a_{\mathrm{s}}) + \frac{\tau_{\mathrm{p}}s_{\mathrm{r}} - \tau_{\mathrm{r}}s_{\mathrm{p}}}{\tau_{\mathrm{p}} - \tau_{\mathrm{r}}} \tag{5.6}$$

$$F = \pi D_{\mathrm{b}} \tau_{\mathrm{p}} \left(\frac{1}{\lambda_1} \tanh(\lambda_1 (L - a_{\mathrm{s}})) \cos(\lambda_2 a_{\mathrm{s}}) + \frac{1}{\lambda_2} \sin(\lambda_2 a_{\mathrm{s}}) \right) \tag{5.7}$$

$$\lambda_2^2 = \frac{\tau_{\mathrm{p}} - \tau_{\mathrm{r}}}{\delta_{\mathrm{r}} - \delta_{\mathrm{p}}} \lambda^2 \tag{5.8}$$

In Phase III, the pull-out force and displacement can be computed as follows:

$$u_{\mathrm{b}} = s_{\mathrm{r}} + \frac{\lambda^2 a_{\mathrm{d}}^2 \tau_{\mathrm{r}}}{2} + \left(\frac{\tau_{\mathrm{p}} \lambda^2}{\lambda_1} \tanh(\lambda_1 (L - a_{\mathrm{d}} - a_{\mathrm{s}})) \cos(\lambda_2 a_{\mathrm{s}}) + \frac{\tau_{\mathrm{p}} \lambda^2}{\lambda_2} \sin(\lambda_2 a_{\mathrm{s}}) \right) a_{\mathrm{d}} \tag{5.9}$$

$$F = \pi D_{\mathrm{b}} \left(\frac{\tau_1}{\lambda_1} \tanh(\lambda_1 (L - a_{\mathrm{d}} - a_{\mathrm{s}})) \cos(\lambda_2 a_{\mathrm{s}}) + \frac{\tau_1}{\lambda_2} \sin(\lambda_2 a_{\mathrm{s}}) + \tau_2 a_{\mathrm{d}} \right) \tag{5.10}$$

In Phase IV, the pull-out force and displacement can be computed as follows:

$$u_{\mathrm{b}} = \delta_{\mathrm{r}} + \lambda^2 \tau_{\mathrm{r}} a_{\mathrm{d}} \left(\frac{a_{\mathrm{d}}}{2} + \frac{\tan(\lambda_2 (L - a_{\mathrm{d}}))}{\lambda_2} \right) \tag{5.11}$$

$$F = \pi D_{\mathrm{b}} \tau_{\mathrm{r}} \left(\frac{\tan(\lambda_2 (L - a_{\mathrm{d}}))}{\lambda_2} + a_{\mathrm{d}} \right) \tag{5.12}$$

Last, in Phase V, the pull-out force and displacement can be computed as follows:

$$F = \pi D_{\mathrm{b}} \tau_{\mathrm{r}} \left(L + \delta_{\mathrm{r}} + \frac{\lambda^2 \tau_{\mathrm{r}} L^2}{2} - u_{\mathrm{b}} \right) \tag{5.13}$$

Equations from (5.4) to (5.13) contributed to the force–displacement relationship of rock bolts. Moreover, a good agreement was obtained between the model and physical test data [24].

5.3 Modelling Process and Results

To investigate the effect of the confining medium diameter on the load-carrying capacity of rock bolts, analytical tests were performed. Specifically, it was assumed that pull-out tests were conducted on deformed rock bolts with the diameter of 25 mm and elastic modulus of 200 GPa. It was admitted that the deformed rock bolts had ribs on the tendon surface. Moreover, the mechanical parameters of ribs, namely rib height and rib spacing, may be dependent on the bolt type [27, 28]. However, for this paper, at the current stage, there was no specific evaluation on the rib height and rib spacing. It was assumed that after the tendon was loaded, the deformed rock bolt induced shearing stress at the bonding face between the tendon and grout. As for the

Table 5.1 Bonding-slipping data for the bonding face between the tendon and grout

τ_1 (MPa)	s_1 (mm)	τ_2 (MPa)	s_2 (mm)
2	1	1	3

influence of the rib height and rib spacing on the shearing stress at the bonding face between the tendon and grout, further work will be continued.

The bolt was installed in the bolting hole with a diameter of 40 mm and grouted length of 2 m. For the grout, it was assumed that it had an unconfined compressive strength of 50 MPa. For the confining medium, it was assumed that it had an elastic modulus of 20 GPa and unconfined compressive strength of 30 MPa. For the bonding face between the tendon and grout, the bonding-slipping data shown in Table 5.1 was used.

Table 5.1 summarised the mechanical properties of the bonding face between the tendon and grout: shearing strength, slipping where shearing strength reached, residual shearing strength and slipping where residual shearing strength reached. They can be computed with the following equation [29]:

$$\tau = \frac{P}{\pi D_{\mathrm{b}} L} \tag{5.14}$$

Specifically, the previous research revealed that if the grouted length of the rock bolt was short enough, the shearing stress at the bonding face can be treated uniform [14]. Therefore, after conducting pull-out tests on rock bolts with short grouted length, the maximum pull-out force and residual pull-out force can be substituted into Eq. (5.14) to compute the shearing strength and residual shearing strength. Then, the slipping where shearing strength reached equalled the pull-out displacement where the maximum pull-out force occurred. The slipping where residual shearing strength reached equalled the pull-out displacement where the residual pull-out force occurred.

In this paper, for the diameter of the confining medium, four different values were used: 100 mm, 150 mm, 200 mm and 250 mm. The configuration of this analytical pull-out test is shown in Fig. 5.2. This analytical pull-out process was generally consistent with the traditional pull-out experiment of rock bolts [30], where the tendon was pulled with a loading rate of 1 mm/min and the load cell together with the linear variable differential transformer were used to measure the pull-out force and displacement, respectively.

Then, the analytical pull-out tests were performed, and the results are shown in Fig. 5.3. Apparently, the confining medium diameter had an effect in determining the performance of rock bolts. Specifically, there was a positive relationship between the load-carrying capacity of rock bolts and the confining medium diameter. Moreover, the ascending rate of the peak force had a tendency to decline. For example, when the confining medium diameter ranged from 200 to 250 mm, the peak force of rock bolts was quite close.

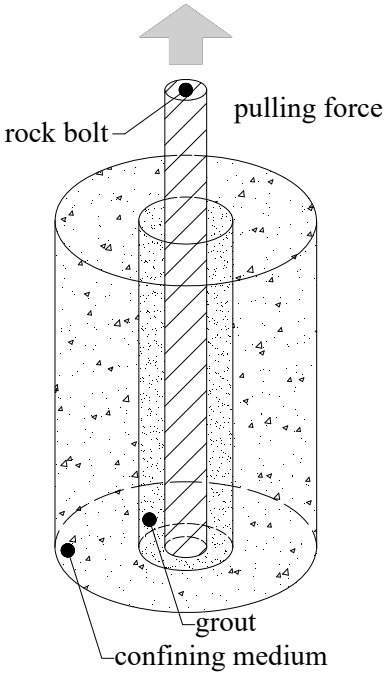

Fig. 5.2 Configuration of the rock bolt loading system

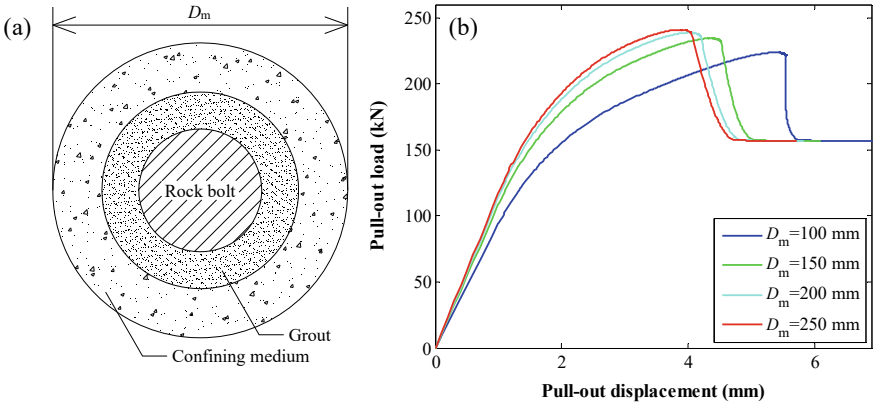

Fig. 5.3 Rock bolt performance with different confining medium diameters: **a** bolting system geometry; **b** force–displacement relationship of rock bolts

To further investigate the influence of the confining medium diameter on the performance of rock bolts, a series of pull-out tests was conducted. In this computation, the confining medium diameter varied in the domain [50 mm, 1000 mm]. Then, the variation trend of the bolt peak force, when the confining medium diameter was varying, was computed, as shown in Fig. 5.4. The peak force ascended significantly

when the confining medium diameter varied from 50 to 300 mm. However, when the confining medium diameter was larger than 300 mm, the ascending rate of the peak force became gentle. Moreover, when the diameter was beyond 400 mm, the peak force became almost constant.

To confirm the accuracy of the analytical modelling results, the experimental tests performed by Rajaie [18] were used as a comparison, as shown in Fig. 5.5. It can be seen that the peak force variation trend in analytical modelling generally agreed well with the experimental test trend. In experimental tests, the peak force rose rapidly with the confining medium diameter when it was smaller than 200 mm. After it was beyond 250 mm, the peak force became almost unchangeable. This variation trend was successfully reflected in analytical modelling.

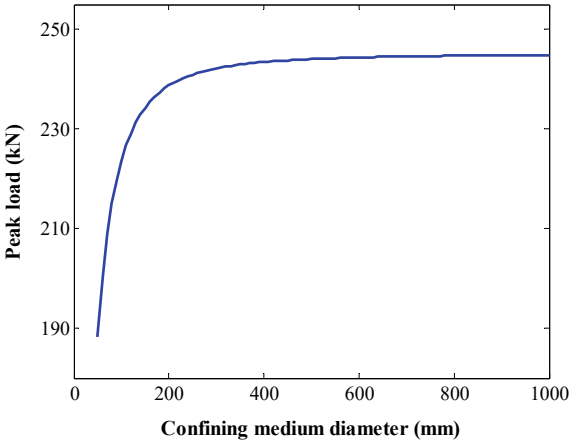

Fig. 5.4 Peak force variation trend when the confining medium diameter was ascending

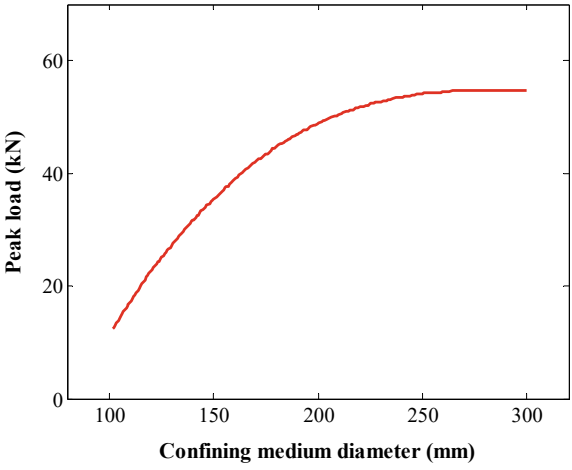

Fig. 5.5 Peak force variation trend of the plain cable bolts [18]

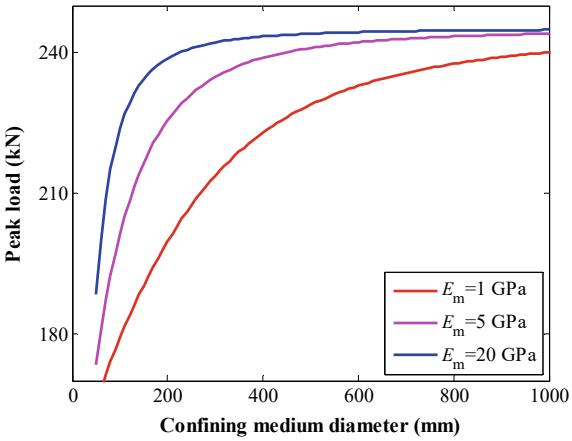

Fig. 5.6 Peak force variation trend with the confining medium ascending when the confining medium modulus was under different levels

In the above analysis, the elastic modulus of the confining medium was set as 20 GPa. However, in experimental tests, the material with different modulus can be used to cast the confining medium. Therefore, further pull-out tests were performed with different confining medium moduli. Specifically, three different moduli were used, 1 GPa, 5 GPa and 20 GPa. The peak force variation trend results are shown in Fig. 5.6. Apparently, the peak force variation trend was consistent. This indicated that although the confining medium modulus was different, there was a critical influence diameter. The confining medium had little effect on the peak force once its diameter was over than the critical influence diameter. It was also found that when the confining medium modulus was different, the critical influence diameter was also different. For example, when the confining medium modulus was 20 GPa, the peak force became almost constant when the confining medium diameter was larger than 400 mm. Nevertheless, this value was changed when the confining medium with a modulus of 1 GPa was used. For it, at a diameter of 400 mm, the peak force was still ascending rapidly.

To study the influence of the confining medium modulus on the critical influence diameter, further pull-out tests were performed. Specifically, the confining medium modulus was ranged from 1 to 50 GPa. With a certain confining medium modulus, the peak force variation trend was first computed. Then, the critical influence diameter for that confining medium modulus was recorded. The critical influence diameter was determined with the following method.

First, a relative difference percentage was defined, as shown in Eq. (5.15).

$$\Delta = \frac{F_{\max 2} - F_{\max 1}}{F_{\max 1}} \tag{5.15}$$

Where Δ: the relative difference percentage. $F_{\max 1}$: peak force when the confining medium diameter was a. $F_{\max 2}$: peak force when the confining medium diameter was $(a + \Delta a)$.

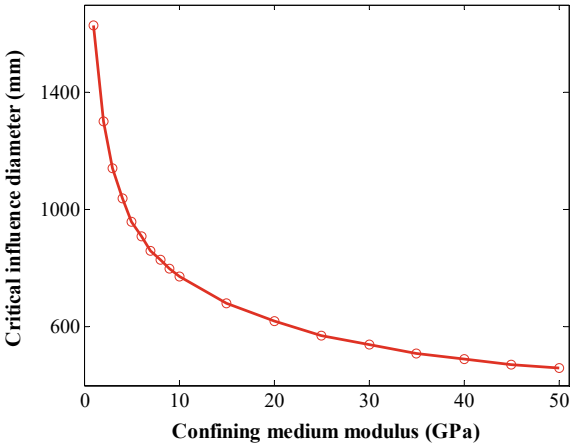

Fig. 5.7 Variation of the critical influence diameter variation when the confining medium modulus was varying

In this paper, the confining medium diameter ascended with a small interval of 10 mm. Then, when the relative difference percentage was smaller than 0.01%, it was assumed that there was no apparent ascending of the peak force. Therefore, the corresponding confining medium diameter was regarded as the critical influence diameter.

Following this method, the critical influence diameter for different confining medium moduli was acquired, as shown in Fig. 5.7. It can be seen that the confining medium modulus had a significant effect in determining the critical influence diameter. With the confining medium modulus ascending, the critical influence diameter declined nonlinearly. This indicated that for the same rock bolt, if the confining medium properties were different, the corresponding critical influence diameter may be different. Furthermore, the larger the confining medium modulus, the smaller the critical influence diameter.

5.4 Conclusions

Laboratory pull-out tests were commonly used to study the performance of rock bolts. In pull-out tests, natural or artificial cylindrical confining medium was usually used to confine rock bolts. This paper conducted an analytical investigation to study the influence of the confining medium diameter on the performance of rock bolts. In the analytical modelling, the load-carrying capacity of rock bolts with different confining medium diameters was compared. The results showed that the confining medium diameter had an apparent effect in determining the peak force of rock bolts. With the confining medium diameter ascending, the peak force ascended. However, the ascending rate of the peak force gradually declined. The peak force variation trend was compared with experimental results. And there was a good agreement between modelling trend and experimental trend.

The rock bolt peak force with different confining medium moduli was studied. It was found that although the confining medium modulus was different, the peak force variation trend was consistent. For each medium modulus, there was a certain critical influence diameter. Beyond that critical influence diameter, further ascending the confining medium diameter had marginal effect in improving the peak force of rock bolts.

Moreover, the influence of the confining medium modulus on the critical influence diameter was analysed. The results showed that the higher the confining medium modulus, the smaller the critical influence diameter.

References

1. D. Li, Y. Li, W. Zhu, Analytical modelling of load-displacement performance of cable bolts incorporating cracking propagation. Rock Mech. Rock Eng. **53**(8), 3471–3483 (2020). https://doi.org/10.1007/s00603-020-02123-1
2. A. Batugin, Z. Wang, Z. Su, S.S. Sidikovna, Combined support mechanism of rock bolts and anchor cables for adjacent roadways in the external staggered split-level panel layout. Int. J. Coal Sci. Technol. **2021**, 1–15 (2021). https://doi.org/10.1007/s40789-020-00399-w
3. A.G. Thompson, E. Villaescusa, C.R. Windsor, Ground support terminology and classification: an update. Geotech. Geol. Eng. **30**(3), 553–580 (2012). https://doi.org/10.1007/s10706-012-9495-4
4. S. Nakamoto, N. Iwasa, J. Takemura, Effects of nails and facing plates on seismic slope response and failure. Géotech. Lett. **7**(2), 1–10 (2017). https://doi.org/10.1680/jgele.16.00179
5. K. Skrzypkowski, W. Korzeniowski, K. Zagórski, A. Zagórska, Modified rock bolt support for mining method with controlled roof bending. Energies **13**(8), 1868 (2020). https://doi.org/10.3390/en13081868
6. J. Chen, H. Zhao, F. He, J. Zhang, K. Tao, Studying the performance of fully encapsulated rock bolts with modified structural elements. Int. J. Coal Sci. Technol. **8**(1), 64–76 (2021). https://doi.org/10.1007/s40789-020-00388-z
7. G. Liu, M. Xiao, J. Chen, H. Zhou, Study on mechanical characteristics of fully grouted rock bolts for underground caverns under seismic loads. Math. Probl. Eng. **2017**, 1–12 (2017). https://doi.org/10.1155/2017/1657369
8. S. Wang, D. Li, C. Li, C. Zhang, Y. Zhang, Thermal radiation characteristics of stress evolution of a circular tunnel excavation under different confining pressures. Tunn. Undergr. Space Technol. **78**, 76–83 (2018). https://doi.org/10.1016/j.tust.2018.04.021
9. S. Wang, X.G. Wu, J.H. Yang, J.Q. Zhao, F.L. Kong, Modeling mechanical behaviour of lightweight concrete structures subjected to 3D coupled static-dynamic loads. Acta Mech. (2020). https://doi.org/10.1007/s00707-020-02739-y
10. D. Li, H. Masoumi, S. Saydam, P.C. Hagan, Mechanical characterisation of modified cable bolts under axial loading: an extensive parametric study. Rock Mech. Rock Eng. **51**(9), 2895–2910 (2018). https://doi.org/10.1007/s00603-018-1475-4
11. K. Skrzypkowski, W. Korzeniowski, K. Zagórski, A. Zagórska, Flexibility and load-bearing capacity of roof bolting as functions of mounting depth and hole diameter. Energies **12**, 1–23 (2019). https://doi.org/10.3390/en12193754
12. S. Ma, X. Zhu, W. Qin, S. Hu, Determination of the bond-slip relationship of fully grouted rockbolts. Environ. Earth Sci. **77**(9), 325–326 (2018). https://doi.org/10.1007/s12665-018-7495-2
13. D. Li, H. Masoumi, P.C. Hagan, S. Saydam, Experimental and analytical study on the mechanical behaviour of cable bolts subjected to axial loading and constant normal stiffness. Int. J. Rock Mech. Min. Sci. **113**, 83–91 (2019). https://doi.org/10.1016/j.ijrmms.2018.11.011

14. L. Blanco Martín, M. Tijani, F. Hadj-Hassen, A. Noiret, Assessment of the bolt-grout interface behaviour of fully grouted rockbolts from laboratory experiments under axial loads. Int. J. Rock Mech. Min. Sci. **63**, 50–61 (2013). http://doi.org/10.1016/j.ijrmms.2013.06.007
15. Q. He, Y. Li, J. Xu, C. Zhang, Prediction of mechanical properties of igneous rocks under combined compression and shear loading through statistical analysis. Rock Mech. Rock Eng. **53**, 841–859 (2020). https://doi.org/10.1007/s00603-019-01948-9
16. C.C. Li, Performance of D-bolts under static loading. Rock Mech. Rock Eng. **45**(2), 183–192 (2012). https://doi.org/10.1007/s00603-011-0198-6
17. Q. Meng, L. Han, J. Sun, F. Min, W. Feng, X. Zhou, Experimental study on the bolt-cable combined supporting technology for the extraction roadways in weakly cemented strata. Int. J. Min. Sci. Technol. **25**(1), 113–119 (2015). https://doi.org/10.1016/j.ijmst.2014.11.010
18. H. Rajaie, *Experimental and Numerical Investigations of Cable Bolt Support Systems* (McGill University, Montreal, 1990)
19. J. Chen, P.C. Hagan, S. Saydam, Sample diameter effect on bonding capacity of fully grouted cable bolts. Tunn. Undergr. Space Technol. **68**, 238–243 (2017). https://doi.org/10.1016/j.tust.2017.06.004
20. J. Zou, P. Zhang, Analytical model of fully grouted bolts in pull-out tests and in situ rock masses. Int. J. Rock Mech. Min. Sci. **113**, 278–294 (2019). https://doi.org/10.1016/j.ijrmms.2018.11.015
21. W. Zhang, L. Huang, C.H. Juang, An analytical model for estimating the force and displacement of fully grouted rock bolts. Comput. Geotech. **117**, 1–10 (2020). https://doi.org/10.1016/j.compgeo.2019.103222
22. S. Ma, J. Nemcik, N. Aziz, Z. Zhang, Analytical model for rock bolts reaching free end slip. Constr. Build. Mater. **57**, 30–37 (2014). https://doi.org/10.1016/j.conbuildmat.2014.01.057
23. D. Li, H. Masoumi, S. Saydam, P.C. Hagan, A constitutive model for load-displacement performance of modified cable bolts. Tunn. Undergr. Space Technol. **68**, 95–105 (2017). https://doi.org/10.1016/j.tust.2017.05.025
24. J. Chen, S. Yang, H. Zhao, J. Zhang, F. He, S. Yin, The analytical approach to evaluate the load-displacement relationship of rock bolts. Adv. Civ. Eng. **2019**, 2678905 (2019). https://doi.org/10.1155/2019/2678905
25. S. Ma, Z. Zhao, W. Nie, Y. Gui, A numerical model of fully grouted bolts considering the tri-linear shear bond-slip model. Tunn. Undergr. Space Technol. **54**, 73–80 (2016). https://doi.org/10.1016/j.tust.2016.01.033
26. F. Ren, Z.J. Yang, J.F. Chen, W.W. Chen, An analytical analysis of the full-range behaviour of grouted rockbolts based on a tri-linear bond-slip model. Constr. Build. Mater. **24**(3), 361–370 (2010). https://doi.org/10.1016/j.conbuildmat.2009.08.021
27. C. Cao, J. Nemcik, N. Aziz, T. Ren, Analytical study of steel bolt profile and its influence on bolt load transfer. Int. J. Rock Mech. Min. Sci. **60**, 188–195 (2013). https://doi.org/10.1016/j.ijrmms.2012.12.013
28. C. Cao, T. Ren, C. Cook, Y. Cao, Analytical approach in optimising selection of rebar bolts in preventing rock bolting failure. Int. J. Rock Mech. Min. Sci. **72**, 16–25 (2014). https://doi.org/10.1016/j.ijrmms.2014.04.026
29. S. Ma, J. Nemcik, N. Aziz, An analytical model of fully grouted rock bolts subjected to tensile load. Constr. Build. Mater. **49**, 519–526 (2013). https://doi.org/10.1016/j.conbuildmat.2013.08.084
30. N. Vlachopoulos, D. Cruz, B. Forbes, Utilizing a novel fiber optic technology to capture the axial responses of fully grouted rock bolts. J. Rock Mech. Geotech. Eng. **10**, 222–235 (2018). https://doi.org/10.1016/j.jrmge.2017.11.007

Chapter 6
Studying the Bond Performance of Fully Grouted Rock Bolts Based on the Variable Controlling

6.1 Introduction

Fully grouted rock bolting is commonly used in roadway reinforcement in mining and tunnelling reinforcement [1]. Due to the advantage that the reinforcing resistance is significant and it can effectively improve the self-bearing capacity of rock masses, rock bolting has been widely applied in rock and soil reinforcement [2].

However, in situ practice results showed that failure of the reinforcement system still occurred [3]. The previous research summarised that failing of the reinforcement system could be bolt rupture or bond failure [4]. It is more common to encounter bond failure at the boundary surface between bolts and grout [5]. The reason is that the bond stress at the boundary surface between bolts and grout is beyond the bond strength [6]. More importantly, it is highly related to the bond capacity of bolts [7].

To study the bond mechanism of rock bolts, laboratory tests, analytical modelling, numerical simulation and engineering practices were used [8]. For example, Zhang et al. [9] conducted in situ tests on gob-side roadways to monitor the loading state of bolts under the thick coal seam mining condition. Skrzypkowski et al. [10] performed laboratory pull-out tests on bolts with different diameters to compare the performance of bolts. Chen et al. [11] used the experimental approach to study the anchorage performance of bolts installed in a bedded rock mass. Chen and Li [12] adopted the modified elements to study the interaction between bolts and in situ rock masses.

Amongst those methods, analytical modelling has the advantage that it can effectively reveal the bond course between bolts and rock masses subjected to loading [13]. Therefore, this paper studied the bond capacity of bolts based on analytical modelling.

In analytical modelling, former investigators performed numerous investigations regarding the bond capacity of bolts [14]. Wang et al. [15] analysed the coupling effect of bolts installed in rock masses. Zou and Zhang [16] used a nonlinear equation to illustrate the debonding behaviour of the boundary surface between bolts and grout. Ren et al. [17] studied the shear failure course of the boundary surface between bolts

J. Chen et al., *Bond Failure Mechanism of Fully Grouted Rock Bolts*,
SpringerBriefs in Applied Sciences and Technology,
https://doi.org/10.1007/978-981-99-0498-3_6

and grout. Zheng et al. [18] studied the reinforcing system composed of bolts and rock masses. Ma et al. [19] established the distributing link of the bond stress at the boundary surface between bolts and grout. He et al. [20] deduced the interaction link between the tensile stress in bolts and the bond stress after bolts which were loaded. Saleem [21] developed an analytical model to study the bond performance of bolts under the impact loading condition. The superiority of their model was that it could be used to predict the bond performance of different bolt types. Lv et al. [22] deduced the load-carrying force of cables based on an elastoplastic model. Wang et al. [23] developed a three-dimensional model to study the bond performance of fully grouted bolts based on a closed tri-linear relationship. Their results showed that there was a critical grouting length. Zhang et al. [24] considered the mutual interaction link between bolts and grout. Saleem and Hosoda [25] employed the Latin Hypercube sampling approach to analyse the test data regarding several fully grouted bolts. Their findings showed that grouting length had more effect on the load-carrying force of bolts compared with bolt diameter.

Those mentioned analytical modelling research successively revealed the coupling link between bolts and rock masses. However, much less work has been performed to quantitatively study the influence of parameters on the bond performance of fully grouted bolts. Moreover, little work was conducted to quantitatively examine the bond stress distributing at the boundary surface between bolts and grout.

To overcome those shortcomings, this paper used the new analytical model developed by the authors to quantitatively examine the bond performance of fully grouted rock bolts [26]. The originality of this paper is that it used the newly developed analytical model to quantitatively examine the bond performance of fully grouted bolts. Moreover, relying on this analytical model, the bond stress distributing at the boundary surface between bolts and grout was quantitatively studied.

In this paper, first, the calculating principle of this analytical model was illustrated. Then, this analytical model was used to calculate and analyse the load-carrying force of bolts. The effect of four different parameters on the load-carrying force of bolts and the bond stress distributing state was studied. This study is conducive to enriching the base of knowledge.

6.2 Calculating Principal of the Constitutive Equation

The authors of this paper previously conducted a theoretical analysis on the load-carrying force of bolts. During modelling, the shear course of the boundary surface was simulated with a tri-linear equation (Fig. 6.1) [26].

$$\tau = k\delta + \tau' \tag{6.1}$$

Where k: slope of the tri-linear equation.

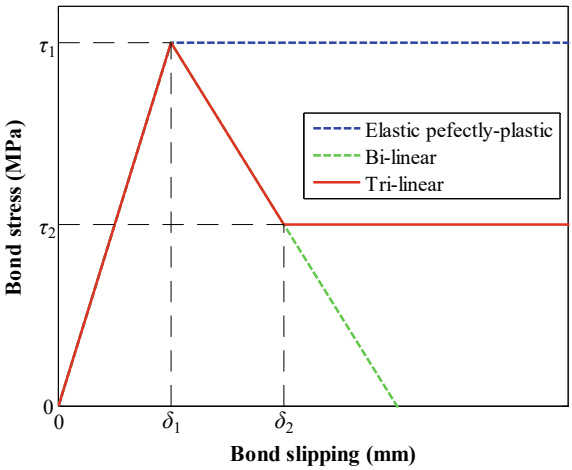

Fig. 6.1 Tri-linear equation

The tri-linear equation was revised from the elastic perfectly plastic model and the bi-linear model. However, the shortcoming of the elastic perfectly plastic model was that it neglected the post-failure performance of the boundary surface. As for the bi-linear model, its shortcoming was that it did not consider the residual shear strength of the boundary surface [27]. Therefore, through combining those two models, the tri-linear equation was used.

The tri-linear equation assumed that the bond stress of the boundary surface grew linearly with the bond slipping. When the bond slipping grew to a specific value, the bond stress reached the bond strength. After that, with the continuous growth of the bond slipping, the bond stress at the boundary surface decreased to the residual shear strength [28]. Last, with the further growth of the bond slipping, the bond stress at the boundary surface remained constant, equalling the residual shear strength.

The credibility of the tri-linear equation was confirmed with the previous experimental research. For example, Benmokrane et al. [29] conducted pull-out tests on fully grouted bolts to study the bond behaviour of the boundary surface. Their results showed that after the peak, the shear stress at the boundary surface dropped gradually. Moreover, with the slipping further growing, the shear stress was likely to be constant. Based on this phenomenon, this paper used the tri-linear equation to depict the bond behaviour of the boundary surface.

Then, this tri-linear equation was incorporated into the anchorage body, and a governing equation was developed, as calculated with Eq. (6.2).

$$\frac{\mathrm{d}\delta^2(x)}{\mathrm{d}x^2} - \lambda^2\tau(x) = 0 \tag{6.2}$$

In this equation, the coefficient of λ can be expressed with Eq. (6.3):

$$\lambda^2 = 4\left(\frac{1}{D_b E_b} + \frac{\pi D_b}{4E_m A_m}\right) \tag{6.3}$$

With the loading of bolts, the boundary surface successively experienced five stages, including the elastic stage, the elastic-weakening stage, the elastic-weakening-friction stage, the weakening-friction stage and the friction stage [30]. Then, analysis was conducted on the tensile stress in bolts and the bond stress on the boundary surface during those five stages. Therefore, the equations that describe the tensile stress distributing of bolts and the bond stress spreading at the boundary surface were obtained. The loading terminal of bolts was regarded as the research objective. Then, the link between the load-carrying force and loading displacement of bolts was obtained.

The credibility of this model was validated with experimental tests. The test conducted by Bai et al. [31] was used as an example. It showed a good match between the test and modelling [26].

6.3 Parameter Study

The input parameters of this model included bolt diameter, bolt modulus, grouting length, modulus of rock masses, the cross-sectional area of rock masses and properties of the boundary surface. Then, this paper studied the effect of relevant parameters on the load-carrying force of bolts.

6.3.1 Bolt Diameter

In this section, it was assumed that the bolt diameter was 20 mm, and the modulus of bolts was 200 GPa. The grouting length was 2 m. As for the rock masses, the modulus was 15 GPa, and the cross-sectional area was 0.5 m^2. Those parameters were shown in Table 6.1.

More importantly, the properties of the boundary surface determined the bond capacity of bolts. Then, they were shown in Table 6.2.

Table 6.1 Properties of the anchorage body

D (mm)	E_1 (GPa)	L (m)	E_2 (GPa)	A (m^2)
20	200	2	15	0.5

Table 6.2 Properties of the boundary surface

τ_1 (MPa)	δ_1 (mm)	τ_2 (MPa)	δ_2 (mm)
3	2	1.5	4

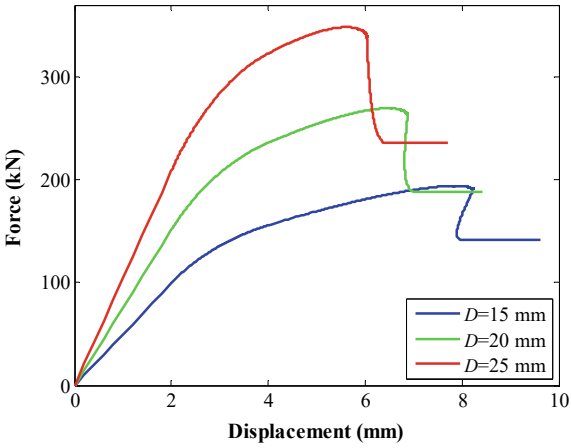

Fig. 6.2 Effect on bolt diameter on the load-carrying force of bolts

To study the effect of bolt diameter on the load-carrying force, besides the bolt diameter used in Table 6.1, another two bolt diameters were used: 15 mm and 25 mm. During the pull-out course, the load-carrying force and loading displacement at the loading terminal were recorded. Then, the bond capacity under the loading condition was obtained (Fig. 6.2). It shows that bolt diameter significantly affected the load-carrying force of bolts. When three different bolt diameters were used, the maximum force was 194 kN, 269 kN and 349 kN. With the growth of bolt diameter, the maximum force significantly grew. This finding was consistent with the experimental test results obtained by Kilik et al. [32]. Meantime, it shows that the stiffness of the anchorage body grew. When the bolt diameter was 15 mm, the initial stiffness of the anchorage body was 50 kN/mm. However, when the bolt diameter grew to 25 mm, the stiffness of the anchorage body grew to 104 kN/mm.

Also, it shows that bolt diameter had specific effect on the post-failure performance of the reinforcement system. For instance, when bolt diameter was small, such as 15 mm, after bolts reached the maximum force, the loading displacement showed an apparent snapback phenomenon. This was because the boundary surface entered the weakening-friction stage. Moreover, it was directly resulted by the continuous growth of the friction length. This phenomenon also occurred in the previous research [33]. By contrast, when bolt diameter was relatively larger, such as 25 mm, after bolts reached the maximum force, this snapback phenomenon was not apparent.

Additionally, the relationship between the maximum force of bolts and λ was analysed. With bolt diameter growing, the corresponding λ dropped from 3.66e−5 to 2.85e−5 N/m (Fig. 6.3). As for the maximum force of bolts, it grew directly. Therefore, a negative relationship between the maximum force of bolts and λ occurred.

This paper mainly focused on the maximum force of bolts. Therefore, when those bolts with three different diameters reached the maximum force, the bond stress distribution of the boundary surface was exported (Fig. 6.4). It shows that when

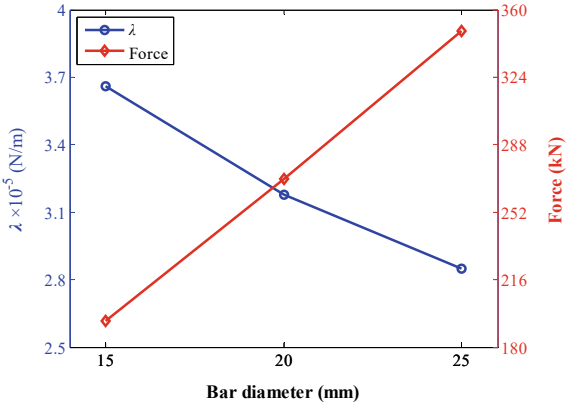

Fig. 6.3 Relationship between the maximum force of bolts, λ and bolt diameter

bolts with those three different diameters reached the maximum force, the bond stress at the boundary surface was in the elastic-weakening-friction stage.

Meantime, it shows that for bolts with a smaller diameter, when the maximum force was reached, the length of the friction section was larger. For instance, when the bolt diameter was 15 mm, the corresponding friction length was 828 mm. However, when the bolt diameter was 25 mm, the friction length dropped to 493 mm. This was related to the reinforcement stiffness of the anchorage body. When the bolt diameter was small, the reinforcement stiffness was also slight. Therefore, to reach the maximum force, a relatively large loading displacement was needed. However, under the effect of the large loading displacement, the boundary surface experienced rather large bond slipping. Then, the friction length grew.

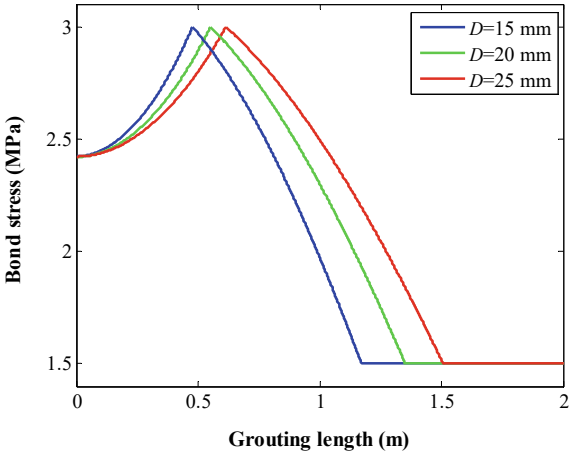

Fig. 6.4 Effect of bolt diameter on the bond stress distributing on the boundary surface when peak load occurred

6.3.2 *Elastic Modulus of Bolts*

In the in situ condition, rock bolts with different modulus may be used. For instance, in the permanent reinforcement, steel bolts with a modulus of 200 GPa were always used. However, in the roadway along the working face side, the fibre-reinforced polymer bolts with modulus of 50 GPa may be used.

Therefore, the modulus of bolts was regarded as the research objective. The purpose was to analyse its effect on the load-carrying force of bolts. In this section, a calculation was conducted on bolts with a diameter of 20 mm. To study the effect of the modulus of bolts, three pull-out analysis was conducted. The corresponding modulus of bolts was 50 GPa, 100 GPa and 200 GPa. The other input parameters were the same as the values used in Sect. 6.3.1. The comparing results of those three pull-out tests are shown in Fig. 6.5. It shows that the elastic modulus of bolts significantly affected the pre-peak and post-peak performance of fully grouted bolts. First, with the modulus of bolts growing from 50 to 200 GPa, the maximum force grew from 229 to 269 kN, growing by 17%. This indicated that although increasing the modulus of bolts was conducive to improving the bond performance of bolts, this impact was not significant. Secondly, the modulus of bolts had a significant impact on the initial stiffness of the anchorage body. Specifically, when the modulus of bolts was 50 GPa, the corresponding initial stiffness of the anchorage body was 38 kN/m. When the modulus of bolts grew to 200 GPa, the corresponding initial stiffness of the anchorage body was 76 kN/m, growing by 100%. Therefore, the larger the modulus of bolts, the higher the stiffness of the anchorage body.

Thirdly, the modulus of bolts significantly influenced the loading displacement where the maximum force of bolts occurred. For example, when bolts with a modulus of 50 GPa were tested, the loading displacement at peak force was 18.1 mm. When the modulus of bolts grew to 100 GPa, the loading displacement at peak force dropped to

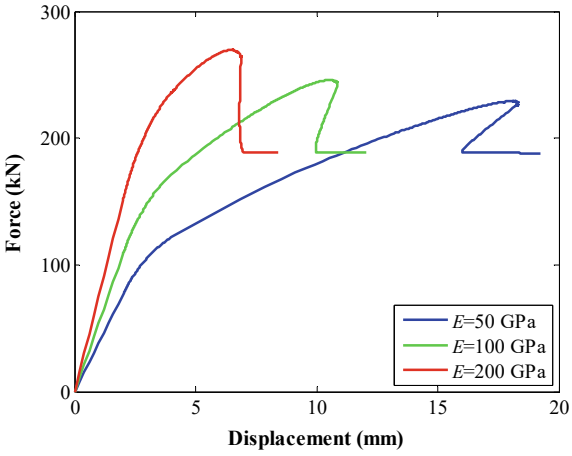

Fig. 6.5 Effect of the modulus of bolts on the load-carrying force

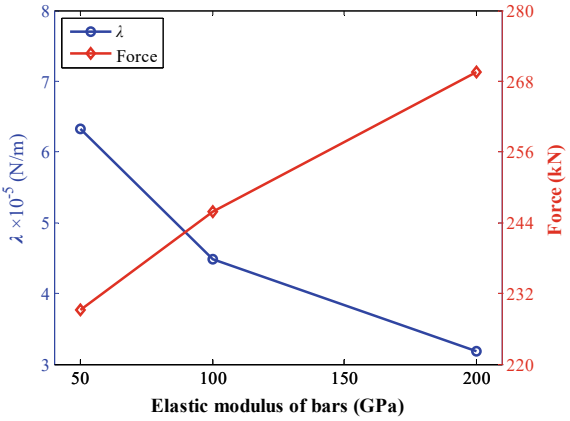

Fig. 6.6 Relationship between the maximum force of bolts, λ and elastic modulus of bolts

10.6 mm. When bolts with a modulus of 200 GPa were tested, the loading displacement dropped to 6.49 mm. Therefore, the loading displacement at peak force significantly dropped with the modulus of bolts. Last, the modulus of bolts influenced the post-peak performance of bolts. When the modulus of bolts was 50 GPa, after the peak load, there was a gradual dropping of the load-carrying force. By contrast, when the modulus of bolts grew to 200 GPa, after the peak force, the load-carrying force dropped dramatically.

Also, the relationship between the maximum force of bolts and λ was analysed. In this case, λ dropped from 6.33e−5 to 3.18e−5 N/m (Fig. 6.6). By contrast, the maximum force of bolts grew. Therefore, for this case, the smaller the λ, the larger the maximum force of bolts.

When bolts reached the maximum force, the bond stress distributing at the boundary surface is exported (Fig. 6.7). The modulus of bolts had a significant effect on the bond stress distributing at the boundary surface. When the modulus of bolts was small, the friction length of the boundary surface was relatively large. For instance, when the modulus of bolts was 50 GPa, the friction length of the boundary surface was 1322 mm. However, when the modulus of bolts was 200 GPa, the friction length of the boundary surface was 648 mm. This was because when the modulus of bolts was small, the stiffness of the reinforcement system was relatively small. Therefore, after a rather large displacement, bolts finally reached the maximum force. Moreover, when a large loading displacement generated, the boundary surface experienced relatively large bond slipping. Therefore, the friction length was relatively large.

6.3.3 Grouting Length of Bolts

In engineering practices, the grouting length can be significantly different [34]. Therefore, in this section, the effect of grouting length on the load-carrying force of bolts

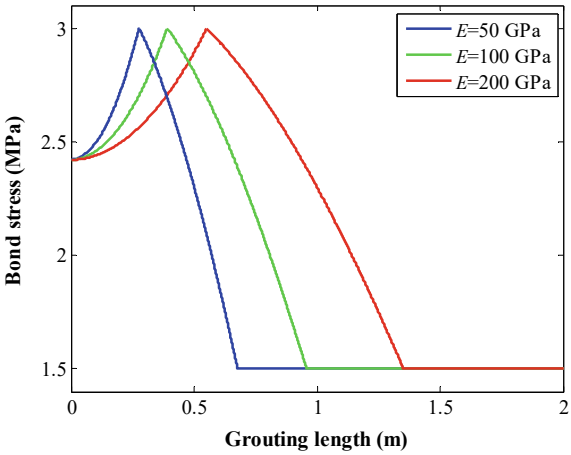

Fig. 6.7 Effect of the modulus on the bond stress distributing on the boundary surface when peak force occurred

was studied. The calculation was conducted on bolts with a diameter of 20 mm and modulus of 200 GPa. During the calculating course, the grouting length ranged between 2 and 3 m. The other input parameters were the same as the values used in Sect. 6.3.1. Then, under those three different grouting length conditions, the bond capacity of bolts was acquired (Fig. 6.8). It shows that growth of the grouting length did not affect the initial reinforcement stiffness of bolts. Under those three different grouting length conditions, in the elastic stage, the initial stiffness was almost same. However, the grouting length had a significant effect on the maximum force of bolts. With the growth of grouting length, the maximum force of bolts significantly grew. When the grouting length grew from 2 to 3 m, the maximum force of bolts grew from 269 to 364 kN.

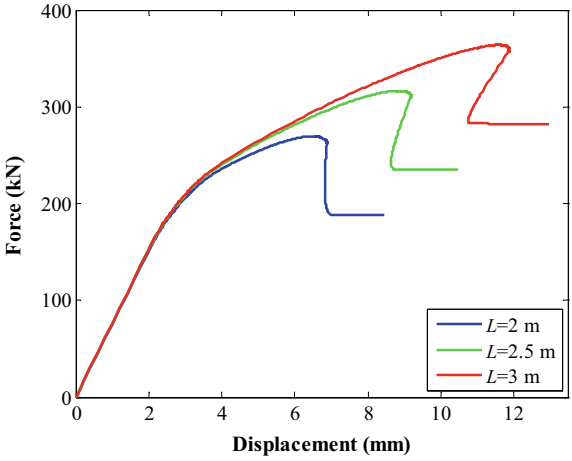

Fig. 6.8 Effect of the grouting length on the load-carrying force of bolts

Attention is paid that this analytical model can be used to calculate the ideal grouting length for bolts. For example, in this case, it is assumed that the tensile strength of bolts was 1200 MPa. Then, this tensile strength was substituted into Eq. (6.4) to calculate the rupture force of bolts.

$$F_r = \frac{\sigma_t \pi D^2}{4} \tag{6.4}$$

Where F_r: rupture force of bolts.

The calculating result showed that the rupture force of bolts was 377 kN. Then, this rupture force can be substituted into the present analytical model to back-calculate the ideal grouting of bolts. For this case, results showed that the ideal grouting length of bolts was around 3.5 m, as shown in Fig. 6.9.

When bolts reached the maximum force, the bond stress at the boundary surface was exported (Figs. 6.10, 6.11 and 6.12). Being different from other parameters, the grouting length had a marginal effect on the bond stress distributing state at the boundary surface. Under three different grouting length conditions, the elastic length of the boundary surface was around 552 mm. All the weakening length was around 800 mm. The only difference was the friction length. Under those three grouting length conditions, the friction lengths were 648 mm, 1149 mm and 1648 mm.

Figure 6.11 showed the bond stress distributing at the boundary surface at the peak force when the grouting length was 2.5 m. It clearly indicated that when the peak force was reached, the bond stress at the boundary surface was in the elastic-weakening-friction state. At the free end of bolts, the bond stress was 2.42 MPa. With the distance from the free end growing, the bond stress grew nonlinearly. When the distance from the free end grew to 0.55 m, the bond stress reached a peak of 3 MPa. With the distance from the free end further growing, the bond stress dropped nonlinearly. When the distance from the free end grew to 1.35 m, the bond stress

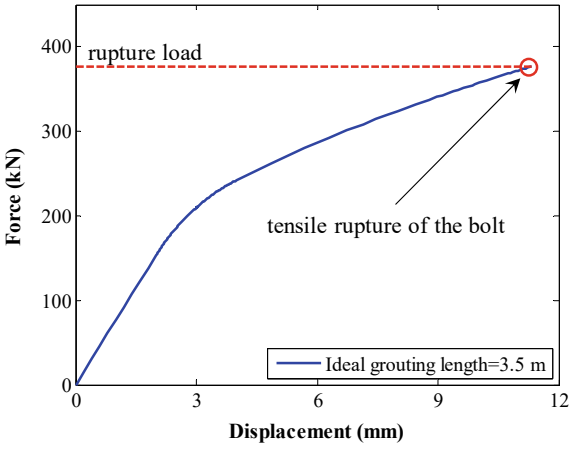

Fig. 6.9 Back calculating the ideal grouting length of bolts

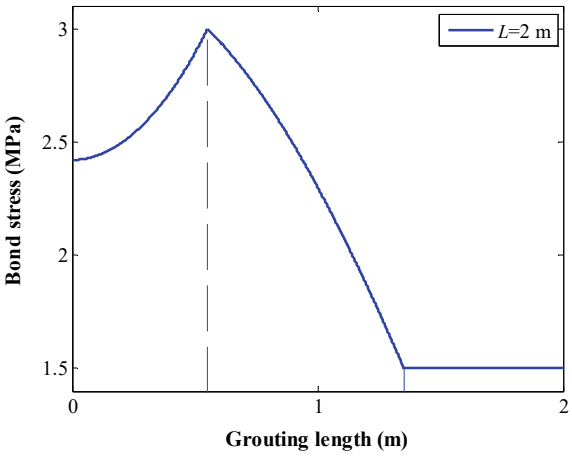

Fig. 6.10 Bond stress distributing at the boundary surface at the peak force when the grouting length was 2 m

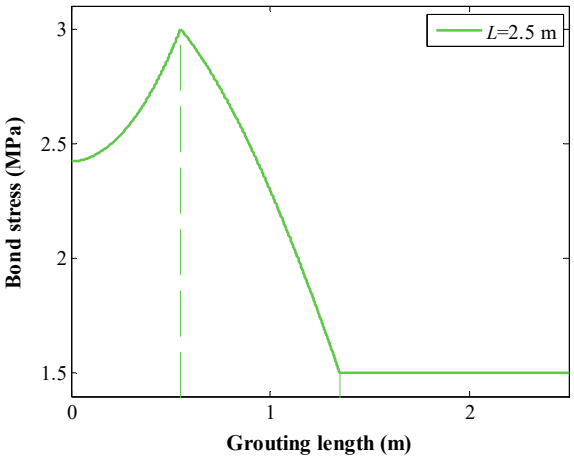

Fig. 6.11 Bond stress distributing at the boundary surface at the peak force when the grouting length was 2.5 m

dropped to the residual bond strength of 1.5 MPa. After that, the bond stress remained constant, levelling at 1.5 MPa.

Figure 6.12 showed the bond stress distributing at the boundary surface at the peak force when the grouting length was 3 m. It showed that although the grouting length grew, the bond stress distributing was still in the elastic-weakening-friction state when the maximum force was reached. More interestingly, the positions where the bond strength and the residual bond strength were reached were identical with Fig. 6.11. However, the only difference was that the friction length grew. In this case, the friction length grew to 1648 mm, 499 mm longer than the friction length shown in Fig. 6.11.

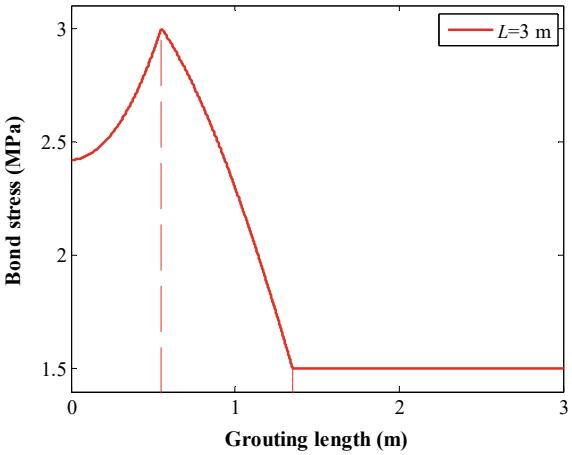

Fig. 6.12 Bond stress distributing at the boundary surface at the peak force when the grouting length was 3 m

6.3.4 Bond Slipping When the Bond Strength Was Reached

Considering that the properties of the boundary surface affected the bond capacity of bolts, the bond slipping at the bond strength was regarded as a factor to conduct the analysis. During the studying, a calculation was conducted on a bolt with a diameter of 20 mm, modulus of 200 GPa and grouting length of 2 m. To study the effect of the bond slipping, it ranged between 1 and 3 mm. The corresponding tri-linear equation is shown in Fig. 6.13.

During calculating, the other parameters were the same as the values used in Sect. 6.3.1. After that, the analytical pull-out test was conducted on bolts, and the corresponding load-carrying force was obtained (Fig. 6.14). It shows that with the

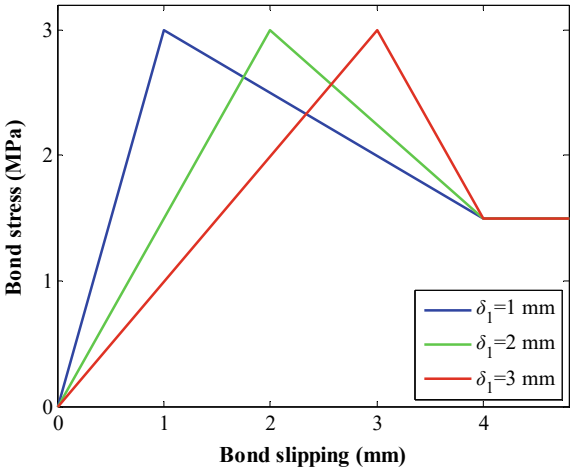

Fig. 6.13 Inputted tri-linear equation

growth of the bond slipping at the bond strength, the maximum force of bolts decreased gradually. Meantime, the stiffness of the reinforcing system gradually decreased. However, this bond slipping did not affect the residual load-carrying force of bolts. Therefore, under those three different conditions, the residual load-carrying force of bolts remained around 188 kN.

When the maximum force of bolts was reached, the bond stress at the boundary surface was exported (Fig. 6.15). With the growth of the bond slipping at the bond strength, the elastic length and the friction length of the boundary surface gradually grew. For instance, as the bond slipping at the bond strength grew from 1 to 3 mm, the elastic length of the boundary surface grew from 300 to 785 mm. Moreover, the corresponding friction length of the boundary surface grew from 483 to 814 mm. The weakening length dramatically declined from 1218 to 400 mm.

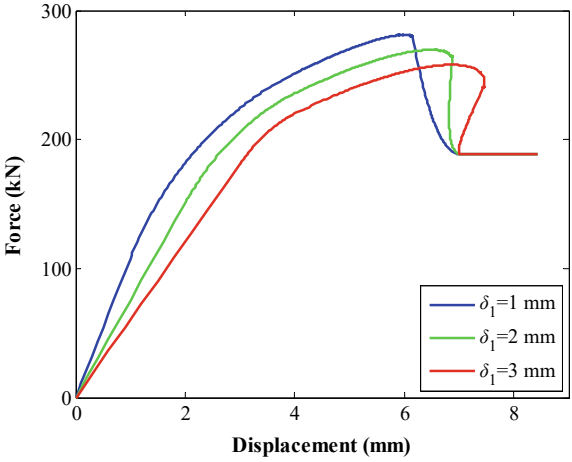

Fig. 6.14 Effect of the bond slipping at the bond strength on the load-carrying force of bolts

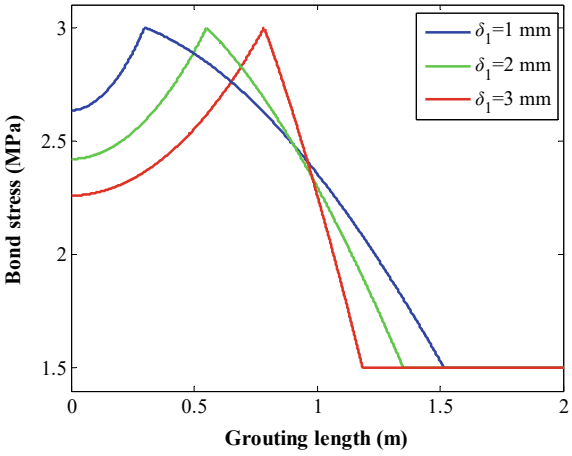

Fig. 6.15 Effect of the bond slipping at the bond strength on the bond stress distributing of the boundary surface

6.4 Limitation of the Current Study

The limitation of the current paper was that it neglected the influence of the filling grout in the borehole. It only considered the interaction between fully grouted bolts and surrounding rock mass.

6.5 Recommendation of Further Work

After the current study, the authors plan to incorporate this analytical model into the underground reinforcement scenarios. Then, the bond performance of fully grouted bolts reinforced in underground roadways and tunnels can be studied. In this way, the reinforcement parameters of fully grouted bolts used in the underground roadways and tunnels can be optimised.

6.6 Conclusions

This paper conducted an analytical study on the bond performance of fully grouted rock bolts based on the variable controlling method. Relied on this approach, the effect of bolt diameter, modulus of bolts, grouting length and bond slipping at the bond strength on the load-carrying force of bolts were studied. Moreover, the bond stress distributing at the boundary surface was studied. This paper is conducive to enriching the basement of knowledge. The main conclusions are listed below:

(1) With bolt diameter growing, the maximum force of bolts significantly grew. In this case, when bolt diameter grew from 15 to 25 mm, the maximum force of bolts grew from 194 to 349 kN, growing by 80%. Meantime, the stiffness of the reinforcement system grew by 108%. When bolts reached the maximum force, the bond stress at the boundary surface was in the elastic-weakening-friction state. Moreover, the smaller the bolt diameter, the longer the friction length.
(2) The elastic modulus of bolts significantly affected the load-carrying force of bolts. With the growth of bolts' modulus, the maximum force of bolts gradually grew. When the elastic modulus grew from 50 to 200 GPa, the maximum force grew from 229 to 269 kN, only growing by 17%. However, the stiffness of the reinforcement system grew by 100%. Moreover, the friction length at the boundary surface declined.
(3) The grouting length had a significant effect on the maximum force of bolts. With the grouting length growing, the maximum force of bolts apparently grew. With the grouting length growing from 2 to 3 m, the maximum force rose from 269 to 364 kN, growing by 35%. However, the grouting length had almost no effect on the stiffness. When bolts reached the maximum force, the bond stress distributing of the boundary surface was consistent. With the grouting

length growing, the length of the elastic part and the weakening part was equal. By contrast, only the friction length grew. With the tensile strength of bolts provided, the current analytical model can be used to back-calculate the ideal grouting length of bolts.

(4) The bond slipping at the bond strength affected the load-carrying force of bolts. When it grew from 1 to 3 mm, the maximum force dropped from 281 to 258 kN, dropping by 8%. As for the stiffness, it dropped by 44%. Moreover, the elastic length and the friction length grew. By contrast, the weakening length declined.

References

1. K. Skrzypkowski, An experimental investigation into the stress-strain characteristic under static and quasi-static loading for partially embedded rock bolts. Energies **14**(5), 1–17 (2021). https://doi.org/10.3390/en14051483
2. Z. Chong, T. Yue, Q. Yao, X. Li, C. Zheng, Z. Xia, H. Li, Experimental and numerical investigation of crack propagation in bolting systems strengthened with resin-encapsulated rock bolts. Eng. Fail. Anal. **122**, 105259 (2021). https://doi.org/10.1016/j.engfailanal.2021.105259
3. S. Ma, Y. Chen, Application of hydraulic fracturing and energy-absorption rockbolts to improve the stability of a gob-side roadway in a 10-m-thick coal seam: case study. Int. J. Geo. **17**(12), 1–12 (2017).
4. S. Yu, W. Zhu, L. Niu, S. Zhou, P. Knag, Experimental and numerical analysis of fully grouted long rockbolt load transfer behaviour. Tunn. Undergr. Space Technol. **85**, 56–66 (2019). https://doi.org/10.1016/j.tust.2018.12.001
5. X. Feng, N. Zhang, S. Yang, F. He, Mechanical response of fully bonded bolts under cyclic load. Int. J. Rock Mech. Min. Sci. **109**, 138–154 (2018). https://doi.org/10.1016/j.ijrmms.2018.06.018
6. J. Chen, P. Liu, H. Zhao, C. Zhang, J. Zhang, Analytical studying the axial performance of fully encapsulated rock bolts. Eng. Fail. Anal. **128**, 1–16 (2021). https://doi.org/10.1016/j.engfailanal.2021.105580
7. Y. Wang, Y. Gao, E. Wang, M. He, J. Yang, Roof deformation characteristics and preventive techniques using a novel non-pillar mining method of gob-side entry retaining by roof cutting. Energies. **11**(3), 1–17 (2018). https://doi.org/10.3390/en11030627
8. S. Ma, X. Zhu, W. Qin, S. Hu, Determination of the bond-slip relationship of fully grouted rockbolts. Environ. Earth Sci. **77**(9), 325–326 (2018). https://doi.org/10.1007/s12665-018-7495-2
9. Z. Zhang, X. Yu, H. Wu, M. Deng, Stability control for gob-side entry retaining with supercritical retained entry width in thick coal seam longwall mining. Energies. **12**(7), 1–16 (2019). https://doi.org/10.3390/en12071375
10. K. Skrzypkowski, W. Korzeniowski, K. Zagórski, A. Zagórska, Flexibility and load-bearing capacity of roof bolting as functions of mounting depth and hole diameter. Energies. **12**, 1–23 (2019). https://doi.org/10.3390/en12193754
11. Y. Chen, J. Teng, R.A. Bin Sadiq, K. Zhang, Experimental study of bolt-anchoring mechanism for bedded rock mass. Int. J. Geo. **20**(4), 1–12 (2020). https://doi.org/10.1061/(ASCE)GM.1943-5622.0001561
12. J. Chen, D. Li, Numerical simulation of fully encapsulated rock bolts with a tri-linear constitutive relation. Tunn. Undergr. Space Technol. **120**, 1–13 (2022). https://doi.org/10.1016/j.tust.2021.104265
13. H. Ma, X. Tan, J. Qian, X. Hou, Theoretical analysis of anchorage mechanism for rock bolt including local stripping bolt. Int. J. Rock Mech. Min. Sci. **122**, 1–6 (2019). https://doi.org/10.1016/j.ijrmms.2019.104080

14. C. Cao, T. Ren, C. Cook, Y. Cao, Analytical approach in optimising selection of rebar bolts in preventing rock bolting failure. Int. J. Rock Mech. Min. Sci. **72**, 16–25 (2014). https://doi.org/10.1016/j.ijrmms.2014.04.026
15. G. Wang, W. Han, Y. Jiang, H. Luan, K. Wang, Coupling analysis for rock mass supported with CMC or CFC rockbolts based on viscoelastic method. Rock Mech. Rock Eng. **52**, 4565–4588 (2019). https://doi.org/10.1007/s00603-019-01840-6
16. J. Zou, P. Zhang, Analytical model of fully grouted bolts in pull-out tests and in situ rock masses. Int. J. Rock Mech. Min. Sci. **113**, 278–294 (2019). https://doi.org/10.1016/j.ijrmms.2018.11.015
17. F. Ren, Z.J. Yang, J.F. Chen, W.W. Chen, An analytical analysis of the full-range behaviour of grouted rockbolts based on a tri-linear bond-slip model. Constr. Build. Mater. **24**(3), 361–370 (2010). https://doi.org/10.1016/j.conbuildmat.2009.08.021
18. X. Zheng, N. Zhang, F. Xue, Study on stress distribution law in anchoring section of prestressed bolt (in Chinese). Journal of Mining and Safety Engineering. **29**(3), 365–370 (2012).
19. S. Ma, J. Nemcik, N. Aziz, An analytical model of fully grouted rock bolts subjected to tensile load. Constr. Build. Mater. **49**, 519–526 (2013). https://doi.org/10.1016/j.conbuildmat.2013.08.084
20. F. He, W. Shi, J. Wu, Stress distribution law analysis of extensible bolting of pre-stressed anchor (in Chinese). Safety in Coal Mines. **47**(1), 212–215 (2016). https://doi.org/10.3969/j.issn.1671-749X.2017.05.013
21. M. Saleem, Multiple crack extension model of steel anchor bolts subjected to impact loading. Constr. Build. Mater. **180**, 364–374 (2018). https://doi.org/10.1016/j.conbuildmat.2018.05.275
22. Q. Lv, Z. Tao, Z. Li, M. He, W. An, Elasto-plastic mechanics analysis of large deformation anchor (in Chinese). Chin. J. Rock Mech. Eng. **37**(4), 1–10 (2018). https://doi.org/10.13722/j.cnki.jrme.2017.0977
23. Y. Wang, Z. Wu, J. Zheng, X. Zhou, Three-dimensional analytical model for the pull-out response of anchor-mortar-concrete anchorage system based on interfacial bond failure. Eng. Struct. **180**, 234–248 (2019). https://doi.org/10.1016/j.engstruct.2018.11.024
24. W. Zhang, L. Huang, C.H. Juang, An analytical model for estimating the force and displacement of fully grouted rock bolts. Comput. Geotech. **117**, 1–10 (2020). https://doi.org/10.1016/j.compgeo.2019.103222
25. M. Saleem, A. Hosoda, Latin hypercube sensitivity analysis and non-destructive test to evaluate the pull-out strength of steel anchor bolts embedded in concrete. Constr. Build. Mater. **290**, 1–13 (2021). https://doi.org/10.1016/j.conbuildmat.2021.123256
26. J. Chen, S. Yang, H. Zhao, J. Zhang, F. He, S. Yin, The analytical approach to evaluate the load-displacement relationship of rock bolts. Adv. Civ. Eng. **2019**, 2678905 (2019). https://doi.org/10.1155/2019/2678905
27. H. Yuan, J.G. Teng, R. Seracino, Z.S. Wu, J. Yao, Full-range behavior of FRP-to-concrete bonded joints. Eng. Struct. **26**(5), 553–565 (2004). https://doi.org/10.1016/j.engstruct.2003.11.006
28. L. Blanco Martín, M. Tijani, F. Hadj-Hassen, A new analytical solution to the mechanical behaviour of fully grouted rockbolts subjected to pull-out tests. Constr. Build. Mater. **25**(2), 1–18 (2010). https://doi.org/10.1016/j.conbuildmat.2010.07.011
29. B. Benmokrane, A. Chennouf, H.S. Mitri, Laboratory evaluation of cement-based grouts and grouted rock anchors. Int. J. Rock Mech. Min. Sci. **32**(7), 633–642 (1995). https://doi.org/10.1016/0148-9062(95)00021-8
30. L. Blanco Martín, M. Tijani, F. Hadj-Hassen, A. Noiret, Assessment of the bolt-grout interface behaviour of fully grouted rockbolts from laboratory experiments under axial loads. Int. J. Rock Mech. Min. Sci. **63**, 63, 50-51 (1995). https://doi.org/10.1016/j.ijrmms.2013.06.007
31. X. Bai, M. Zhang, N. Yan, Field contrast test and mechanism analysis on anchorage performance of anti-floating anchors with two different materials. China Civ. Eng. J. **48**(8), 38-46 (2015). https://doi.org/10.15951/j.tmgcxb.2015.08.005
32. A. Kilik, E. Yasar, A.G. Celik, Effect of grout properties on the pull-out load capacity of fully grouted rock bolt. Tunn. Undergr. Space Technol. **17**, 355-362 (2002). https://doi.org/10.1016/S0886-7798(02)00038-X

33. J. Vaculik, A.B. Sturm, P. Visintin, M.C. Griffith, Modelling FRP-to-substrate joints using the bilinear bond-slip rule with allowance for friction-full-range analytical solutions for long and short bonded lengths. Int. J. Solids Struct. **135**, 245-260 (2018). https://doi.org/10.1016/j.ijsolstr.2017.11.024
34. Y. Cai, T. Esaki, Y. Jiang, An analytical model to predict axial load in grouted rock bolt for soft rock tunnelling. Tunn. Undergr. Space Technol. **19**(6), 607-618 (2004). https://doi.org/10.1016/j.tust.2004.02.129

Chapter 7
Analytical Modelling Rock Bolts with a Closed Nonlinear Model

7.1 Introduction

Rock bolts have been used in the mining industry for a long time. They are used as the reinforcement tendons to keep the stability of openings in underground mining and the slope in open-pit mining. Furthermore, currently, rock bolts are commonly used not only in the mining engineering but also in civil engineering [1].

The rock bolt is a tendon which can be a rod or a cable inserted into a borehole drilled in rock masses or soils. Traditionally, the material of rock bolts was steel. However, engineering practices showed that the steel rock bolts can be easily corroded by the moist environment in underground mines. Then, the fibre-reinforced polymer (FRP) was used to manufacture rock bolts, which are termed as FRP rock bolts. Experimental results proved that the FRP rock bolts can effectively reinforce the surrounding rock masses without being corroded [2].

When rock bolts are installed, they can be point anchored or fully grouted. And the bonding agent can be polyester resin or cementitious grout. This chapter deals with fully grouted rock bolts.

After fully grouted rock bolts are installed in rock masses, the movement of surrounding rock mass induces shear deformation of the grout column. Consequently, shear stress occurs along the bolt/grout and grout/rock interfaces. Then, the load can be transferred between rock bolts and the surrounding rock masses. To study the load transfer process of rock bolts, numerous laboratory and in situ tests have been conducted. Compared with that, relatively less work has been conducted with analytical modelling to study the load transfer behaviour of rock bolts.

The pioneering work in this area should be attributed to Hawkes and Evans [3], who developed an analytical model to study the shear stress distribution along a fully grouted steel bolt. However, their results were only applicable to the case that the grouted bolt was coupled with the surrounding confining medium. Farmer [4] studied the shear stress distribution of the bolt/grout interface with an analytical

J. Chen et al., *Bond Failure Mechanism of Fully Grouted Rock Bolts*,
SpringerBriefs in Applied Sciences and Technology,
https://doi.org/10.1007/978-981-99-0498-3_7

model. Experimental work was used to validate this analytical model. However, this model was not applicable for the debonding behaviour of the bolt/grout interface.

Ren et al. [5] studied the load transfer behaviour of a fully grouted rock bolt with a tri-linear model. The pull-out stages of a rock bolt were divided into five stages, including elastic, elastic-softening, elastic-softening-debonding, softening-debonding and debonding. The model was successfully validated with laboratory and in situ test results. However, when the tri-linear model was used to depict the bond-slip behaviour of the bolt/grout interface, pure softening may also occur along the bolt/grout interface, as indicated by Blanco Martín et al. [6]. And this was not considered in the analytical model proposed by Ren et al. [5].

Recently, Liu et al. [7] proposed an analytical model to study the load transmission model for a rock bolt subjected to open and sliding joint displacements. Experimental work was used to validate this model. The modelling results revealed that for a definite joint displacement and joint location, larger anchored angle between the rock bolt and the joint face was beneficial for improving the reinforcement effect.

Ma et al. [8] proposed an analytical model to study the load transfer mechanism of fully grouted rock bolts. In their model, a closed nonlinear model was used to depict the bond-slip behaviour of the bolt/grout interface [8–10]. In this chapter, the authors adopted their model and conducted a study on the load transfer behaviour of rock bolts. First, a general illustration of the analytical model was given. Then, an experimental test was used to validate this analytical model. Following it, a parametric study was conducted with this analytical model. Last, the load distribution along a fully grouted rock bolt was studied based on this analytical model.

7.2 Illustration of the Analytical Model

For a fully grouted rock bolting system without faceplate, when the rock bolt is loaded, shear stress occurs along the bolt/grout and grout/rock interfaces. When the shear stress is higher than the interfacial bond strength, bond failure of the interface occurs. Experimental tests proved that the major failure mode is the bond failure of the bolt/grout interface [11]. Therefore, in this chapter, failure along the bolt/grout interface was studied.

Assuming that the rock bolt is in linear elastic deformation along the axial direction and the shear stress of the bolt/grout interface is equal to the axial displacement of the rock bolt at the same position, the shear stress of the bolt/grout interface, the pull-out load of the rock bolt and the load distribution along the rock bolt can be expressed with Eqs. (7.1), (7.2) and (7.3), respectively [8, 9].

$$\tau(\delta) = \frac{E_b D_b}{4} \frac{a}{b^2} e^{-\frac{\delta}{a}} \left(1 - e^{-\frac{\delta}{a}}\right) \tag{7.1}$$

Where a and b are coefficients.

$$F_{\mathrm{b}}(\delta) = \frac{E_{\mathrm{b}}\pi D_{\mathrm{b}}^2}{4}\frac{a}{b}\left(1 - \mathrm{e}^{-\frac{\delta}{a}}\right) \tag{7.2}$$

$$F_{\mathrm{b}}(\delta) = \frac{E_{\mathrm{b}}\pi D_{\mathrm{b}}^2}{4}\frac{a}{b}\frac{1}{\left(1 + \mathrm{e}^{-\frac{x-x_0}{b}}\right)} \tag{7.3}$$

Where x_0 is a coefficient and can be calculated with Eq. (7.4).

$$x_0 = L + b\ln\left(\frac{a}{b}\frac{E_{\mathrm{b}}\pi D_{\mathrm{b}}^2}{4F_{\mathrm{b}}} - 1\right) \tag{7.4}$$

7.3 Validation of the Analytical Model

To further confirm the credibility of this analytical model, an in situ pull-out test was used to validate this analytical model. Bastamia et al. [12] conducted a case study in a coal mine. Specifically, rock bolts with a diameter of 22 mm were installed in the rock mass [12]. The rock bolt has an elastic modulus of 207 GPa and embedment length of 1800 mm. During the test, the pull-out load and displacement were recorded.

In this chapter, to analytically model the pull-out process of the rock bolt, Eq. (7.2) was used to calculate the load versus displacement of the rock bolt. It was found that when $a = 1.5$ mm and $b = 620.6$ mm, there was a close match between the experimental pull-out test result and the analytical result, as shown in Fig. 7.1.

By substituting the calculated coefficients a and b into Eq. (7.1), the shear stress versus shear slippage of the bolt/grout interface can be acquired, as shown in Fig. 7.2.

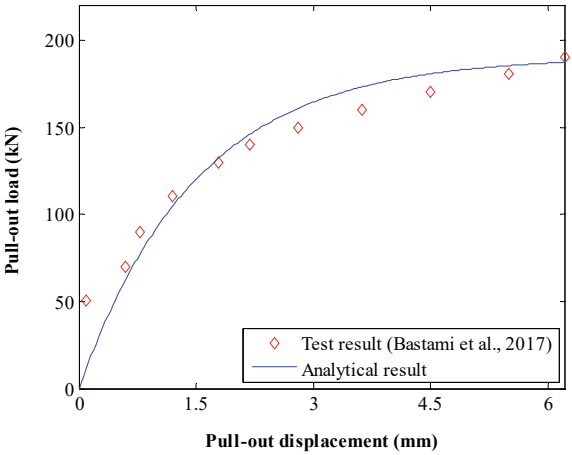

Fig. 7.1 Comparison of the in situ test result conducted by Bastamia et al. [12] and the analytical modelling result

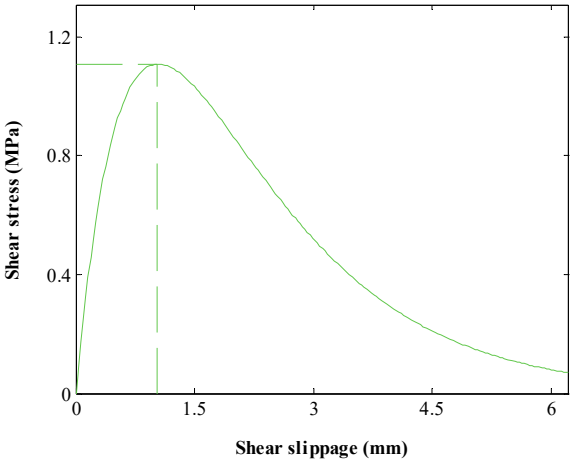

Fig. 7.2 Shear stress versus shear slippage of the bolt/grout interface

It can be seen that after the rock bolt was loaded, the shear stress of the bolt/grout interface increased nonlinearly. When the shear slippage of the bolt/grout interface was 1 mm, the shear stress of the bolt/grout interface reached the bond strength of the bolt/grout interface, which was 1.11 MPa. After that, the shear stress of the bolt/grout interface decreased exponentially.

7.4 Parametric Study

After the analytical model was validated, a parametric study was conducted with this analytical model to evaluate the influence of different parameters on the load transfer behaviour of rock bolts.

7.4.1 The First Coefficient

In this analytical model, there are two important coefficients including *a* and *b*. The parametric study was first conducted to evaluate the influence of the coefficient a on the load transfer performance of rock bolts. Specifically, the load transfer of a rock bolt with an elastic modulus of 210 GPa and diameter of 20 mm was simulated. The coefficient *b* was kept constant in this calculation and equal to 800 mm. As for the coefficient a, three different values were used separately, namely 2, 3 and 4 mm. The pull-out load versus displacement relationship is shown in Fig. 7.3.

Apparently, the coefficient *a* had an obvious effect on the load transfer capacity of rock bolts. The maximum load transfer capacity of the rock bolt was extracted. Then, the relationship between the maximum load transfer capacity of the rock bolt

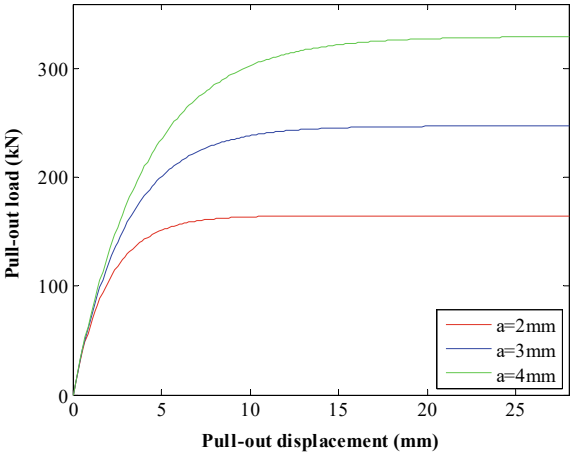

Fig. 7.3 Pull-out load versus displacement curve of the rock bolt when the coefficient a was different

and the coefficient *a* can be plotted, as shown in Fig. 7.4. It can be seen that with the coefficient *a* increasing, the maximum load transfer capacity of rock bolts increases linearly.

Meanwhile, the shear stress versus shear slippage of the bolt/grout interface can be acquired, as shown in Fig. 7.5.

The results show that although the coefficient a was different, the trend of the bond-slip behaviour of the bolt/grout interface was still consistent. However, the coefficient a had an apparent influence in deciding the shear slippage when the bond strength of the bolt/grout interface occurred. For example, with the coefficient *a* increasing from 2 to 4 mm, when the bond strength of the bolt/grout interface occurred, the shear slippage also increased from 1.4 to 2.8 mm.

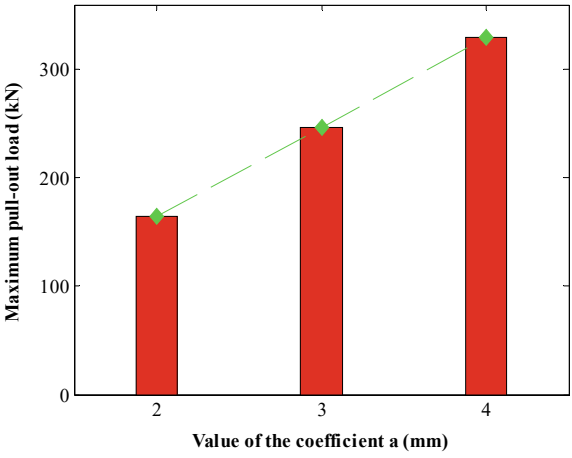

Fig. 7.4 Effect of coefficient a on the maximum load transfer capacity of the rock bolt

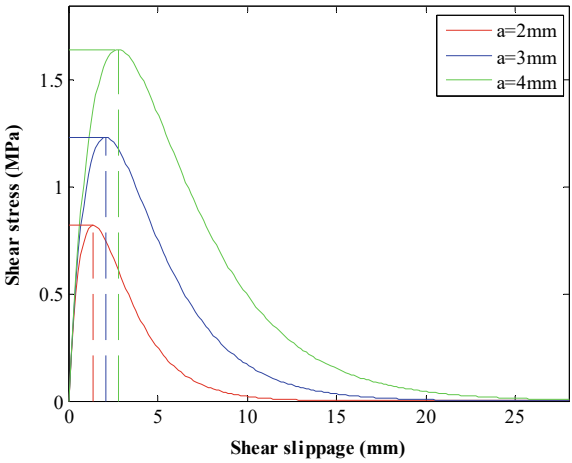

Fig. 7.5 Shear stress versus shear slippage curve of the bolt/grout interface when coefficient a was different

Furthermore, with the coefficient a increasing, the bond strength of the bolt/grout interface also increased. To further illustrate this, the bond strength of the bolt/grout interface when the coefficient a was different was extracted. Then, the relationship between the bond strength of the bolt/grout interface and the coefficient a was plotted, as shown in Fig. 7.6.

The results show that when $a = 2$ mm, the bolt/grout interface had a bond strength of 0.82 MPa. Compared with that, when $a = 3$ mm, increasing by 50%, the bolt/grout interface had a bond strength of 1.23 MPa, increasing by 50%. Last, when $a = 4$ mm, increasing by 100%, the bolt/grout interface had a bond strength of 1.64 MPa, increasing by 100%. Apparently, the larger the coefficient a, the higher the bond strength of the bolt/grout interface. Additionally, there was a linear relationship between the bond strength of the bolt/grout interface and the coefficient a.

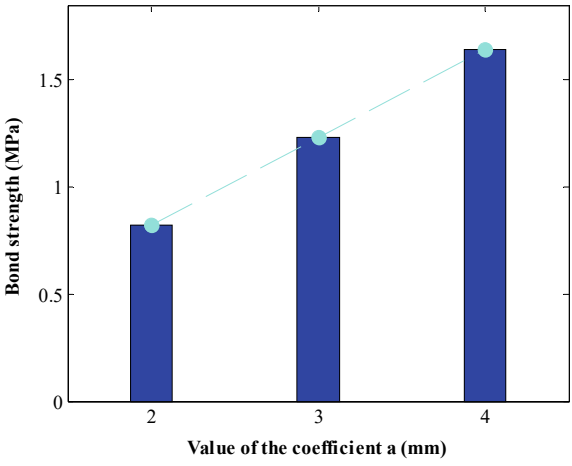

Fig. 7.6 Effect of coefficient a on the bond strength of the bolt/grout interface

7.4.2 The Second Coefficient

Similarly, the influence of coefficient *b* on the load transfer performance of a rock bolt was studied. The rock bolt had an elastic modulus of 210 GPa and diameter of 20 mm. In this case, the coefficient *a* was kept constant and equal to 2 mm. As for the coefficient *b*, three different values were used, namely 500, 600 and 700 mm. The pull-out load versus displacement relationship of the rock bolt is shown in Fig. 7.7.

Apparently, the coefficient *b* had a significant effect on the load transfer performance of rock bolts. With the coefficient *b* increasing, the load transfer capacity of rock bolts tended to decrease. To clearly show this, the maximum load transfer capacity of rock bolts was extracted and plotted with the coefficient *b* (Fig. 7.8).

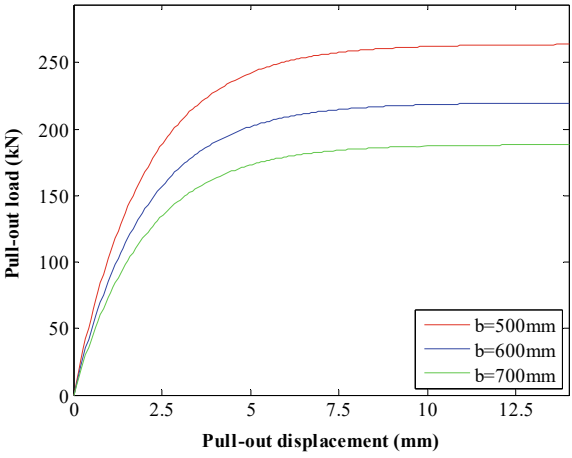

Fig. 7.7 Pull-out load versus displacement curve of the rock bolt when the coefficient *b* was different

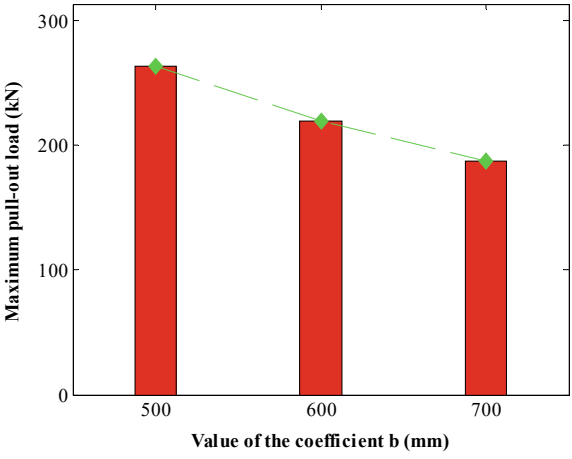

Fig. 7.8 Effect of coefficient *b* on the maximum load transfer capacity of the rock bolt

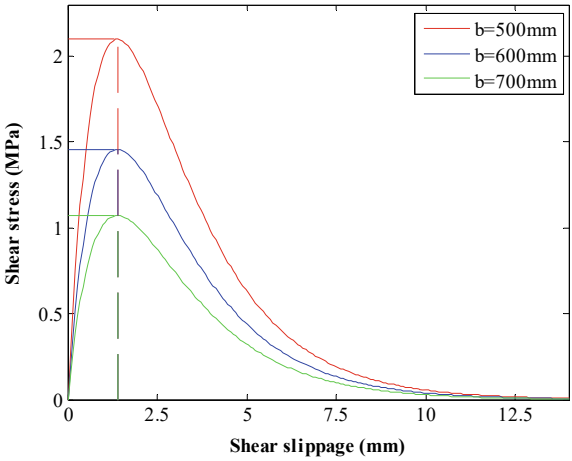

Fig. 7.9 Shear stress versus shear slippage curve of the bolt/grout interface when coefficient b was different

It shows that when $b = 500$ mm, the maximum load transfer capacity of the rock bolt was 264 kN. Compared with that, when $b = 600$ mm, increasing by 20%, the maximum load transfer capacity of the rock bolt was 220 kN, decreasing by 16.7%. When $b = 700$ mm, increasing by 40%, the maximum load transfer capacity of the rock bolt was 188 kN, decreasing by 28.8%. Therefore, increasing the coefficient b leaded to nonlinear decreasing of the maximum load transfer capacity of rock bolts. As for the influence of the coefficient b on the bond-slip behaviour of the bolt/grout interface, it is shown in Fig. 7.9.

It shows that with the coefficient b increasing, the trend of the bond-slip of the bolt/grout interface kept consistent. Furthermore, the coefficient b had no effect in deciding the shear slippage where the bond strength of the bolt/grout interface occurred. For example, in this case, although the coefficient b was different, the shear stress of the bolt/grout interface reached the bond strength at the same shear slippage of 1.4 mm.

However, the coefficient b had an apparent effect on the bond strength of the bolt/grout interface. To illustrate this clearly, the bond strength of the bolt/grout interface was extracted and plotted with the coefficient b, as shown in Fig. 7.10.

The results show that increasing the coefficient b leaded to decreasing the bond strength of the bolt/grout interface. Specifically, when $b = 500$ mm, the bond strength of the bolt/grout interface was 2.1 MPa. Compared with that, when $b = 600$ mm, increasing by 20%, the bond strength of the bolt/grout interface decreased to 1.46 MPa, decreasing by 30.5%. When $b = 700$ mm, increasing by 40%, the bond strength of the bolt/grout interface decreased to 1.07 MPa, decreasing by 49%. Therefore, there was a negative nonlinear relationship between the bond strength of the bolt/grout interface and the coefficient b.

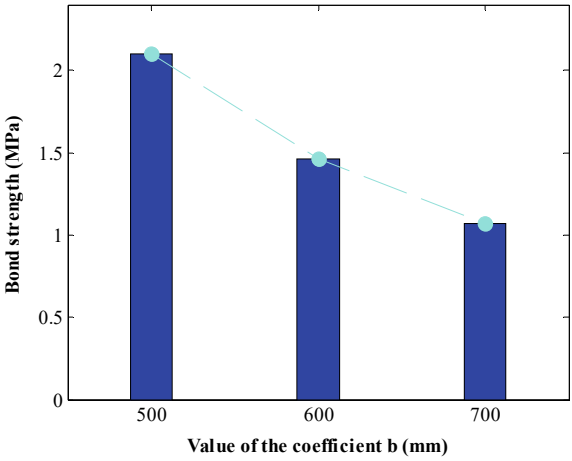

Fig. 7.10 Effect of coefficient *b* on the bond strength of the bolt/grout interface

7.4.3 Elastic Modulus of the Rock Bolt

The influence of the elastic modulus of the rock bolt was studied on the load transfer performance of rock bolts. In this case, the rock bolt had a diameter of 20 mm. As for the coefficients *a* and *b*, they were 2 and 500 mm. As for the elastic modulus of the rock bolt, they were ranged from 70 to 210 GPa with an interval of 70 GPa. The load versus displacement relationship of the rock bolt is shown in Fig. 7.11.

The results show that increasing the elastic modulus of the rock bolt was beneficial for improving the maximum pull-out load of the rock bolt. Furthermore, with the elastic modulus of the rock bolt increasing, the slope of the load–displacement curve also increased. This indicated that increasing the elastic modulus of the rock bolt was beneficial for improving the stiffness of the rock bolting system.

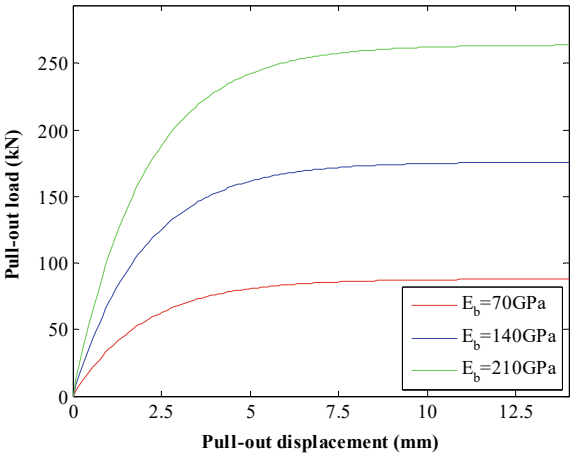

Fig. 7.11 Pull-out load versus displacement curve of the rock bolt when the elastic modulus of the rock bolt was different

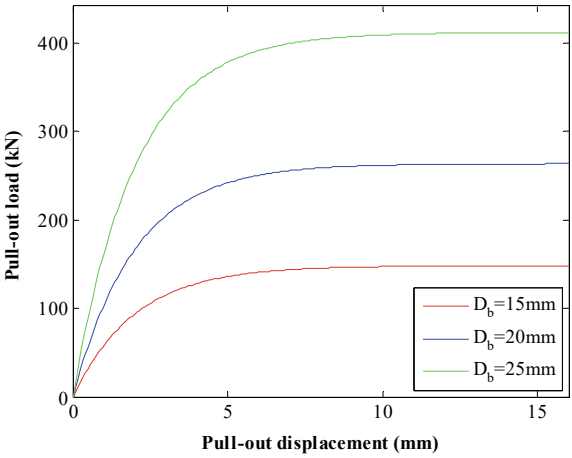

Fig. 7.12 Pull-out load versus displacement curve of the rock bolt when the rock bolt diameter was different

7.4.4 Rock Bolt Diameter

The analytical model was also used to evaluate the influence of the rock bolt diameter on the load transfer behaviour of rock bolts. Specifically, the elastic modulus of the rock bolt was kept constant and equal to 210 GPa. As for the coefficients a and b, they were set as 2 mm and 500 mm. The rock bolt diameter was ranged from 15 to 25 mm with an interval of 5 mm. The pull-out load versus displacement relationship of rock bolts is shown in Fig. 7.12. It shows that increasing the rock bolt diameter can effectively improve the load transfer capacity of rock bolts.

7.5 Load Distribution Along a Fully Grouted Rock Bolt

The load distribution along a fully grouted rock bolt was studied with this analytical model. Specifically, the rock bolt had an elastic modulus of 210 GPa and diameter of 25 mm. As for the coefficients a and b, they were set as 0.53 mm and 200 mm. To simulate the load variation along the grouted rock bolt, an embedment length of 2000 mm was used.

The rock bolt was pulled to a displacement of 3.2 mm and reached a maximum pull-out load of 273 kN. During the pull-out process, the axial load in the rock bolt was calculated when the pull-out load ranged from 50 to 250 kN with an interval of 50 kN. Specifically, by substituting the pull-out load to Eq. (7.4), x_0 can be acquired. Then by substituting x_0 to Eq. (7.3), the axial load along the rock bolt from the free end to the loaded end can be acquired, as shown in Fig. 7.13.

The results show that during the pull-out process, the axial load in the rock bolt decayed from the loaded end to the free end independent of the pull-out load. However, the decaying trend of the axial load was different. Specifically, when the

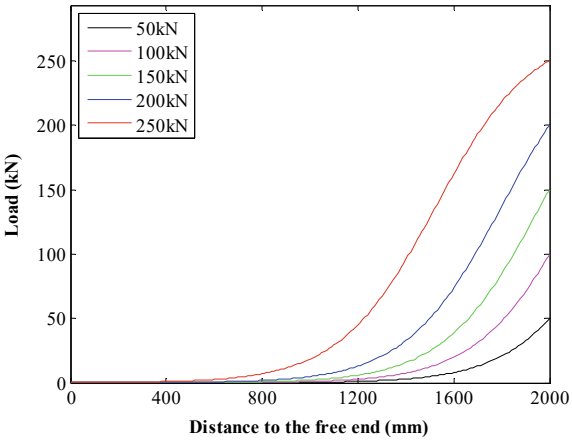

Fig. 7.13 Load distribution along the fully grouted rock bolt

pull-out load was small, for example, 50 kN, the axial load in the rock bolt decayed from the loaded end to the free end with a simple exponential form. Furthermore, the bending direction of the load distribution curve was always upward. However, when the pull-out load was large, for example, 250 kN, only the axial load in the rock bolt close to the free end decayed with an exponential form. There were two bending directions of the load distribution curve. For the section close to the free end, the bending direction of the load distribution curve was upward whilst for the section close to the loaded end, the bending direction of the load distribution curve was downward. Nevertheless, further experimental work should be conducted to validate this finding.

7.6 Limitation and Recommendation for Future Work

A limitation of the current study was that only one experimental pull-out test was used to validate the credibility of this analytical model. In fact, the previous research has proved that the rock bolt performance was influenced by many parameters such as the rock bolt profile, the rock mass property, the embedment length and the borehole diameter [13–18]. Therefore, in the future work, more experimental pull-out tests with different performance will be adopted to further confirm the accuracy of the analytical model.

7.7 Conclusions

An analytical model was used to study the load transfer behaviour of fully grouted rock bolts. In this analytical model, a closed nonlinear model was used to depict the bond-slip behaviour of bolt/grout interface.

An in situ pull-out test was used to validate this analytical model, showing that there was a close match between the experimental result and analytical result. Following it, a parametric study was conducted to evaluate the influence of two coefficients, elastic modulus of the rock bolt and the diameter of the rock bolt on the performance of rock bolts. It was found that increasing the coefficient a leaded to linear increasing of the maximum pull-out load of rock bolts and the bond strength of the bolt/grout interface. On the other hand, increasing the coefficient b leaded to nonlinear decreasing of the maximum pull-out load of rock bolts and the bond strength of the bolt/grout interface. Improving the elastic modulus of the rock bolt and the diameter of the rock bolt were beneficial for improving the load transfer capacity of the rock bolting system.

Additionally, the load distribution along the fully grouted rock bolt was studied with this analytical model. It was found that axial load in the rock bolt decayed from the loaded end to the free end independent of the pull-out load. However, the trend of the load distribution curve along the rock bolt was influenced by the pull-out load. When the pull-out load was relatively small, the bending direction of the load distribution curve was upward. However, when the pull-out load was relatively large, there were two bending directions of the load distribution curve. For the section close to the free end, the bending direction of the load distribution curve was upward whilst for the section close to the loaded end, the bending direction was downward.

References

1. A.G. Thompson, E. Villaescusa, C.R. Windsor, Ground support terminology and classification: an update. Geotech. Geol. Eng. **30**(3), 553–580 (2012). https://doi.org/10.1007/s10706-012-9495-4
2. W. Wang, Q. Song, C. Xu, H. Gong, Mechanical behaviour of fully grouted GFRP rock bolts under the joint action of pre-tension load and blast dynamic load. Tunn. Undergr. Space Technol. **73**, 82–91 (2018). https://doi.org/10.1016/j.tust.2017.12.007
3. J.M. Hawkes, R.H. Evans, Bond stresses in reinforced concrete columns and beams. Struct. Eng. **29**, 323–327 (1951)
4. I.W. Farmer, Stress distribution along a resin grouted rock anchor. Int. J. Numer. Anal. Meth. Geomech. **12**, 347–351 (1975). https://doi.org/10.1016/0148-9062(75)90168-0
5. F. Ren, Z.J. Yang, J.F. Chen, W.W. Chen, An analytical analysis of the full-range behaviour of grouted rockbolts based on a tri-linear bond-slip model. Constr. Build. Mater. **24**(3), 361–370 (2010). https://doi.org/10.1016/j.conbuildmat.2009.08.021
6. L. Blanco Martín, M. Tijani, F. Hadj-Hassen, A. Noiret, Assessment of the bolt-grout interface behaviour of fully grouted rockbolts from laboratory experiments under axial loads. Int. J. Rock Mech. Min. Sci. **63**, 50–61 (2013). http://doi.org/10.1016/j.ijrmms.2013.06.007

7. J. Liu, H. Yang, H. Wen, X. Zhou, Analytical model for the load transmission law of rock bolt subjected to open and sliding joint displacements. Int. J. Rock Mech. Min. Sci. **100**, 1–9 (2017). https://doi.org/10.1016/j.ijrmms.2017.01.018
8. S. Ma, J. Nemcik, N. Aziz, An analytical model of fully grouted rock bolts subjected to tensile load. Constr. Build. Mater. **49**, 519–526 (2013). https://doi.org/10.1016/j.conbuildmat.2013.08.084
9. Y. Zhou, Y. Wu, Y. Yun, Analytical modeling of the bond-slip relationship at FRP-concrete interfaces for adhesively-bonded joints. Compos. Part B **41**, 423–433 (2010). http://doi.org/10.1016/j.compositesb.2010.06.004
10. J. Dai, T. Ueda, Y. Sato, Development of the nonlinear bond stress-slip model of fiber reinforced plastics sheet-concrete interfaces with a simple method. J. Compos. Constr. **9**, 52–62 (2005). https://doi.org/10.1061/(ASCE)1090-0268(2005)9:1(52)
11. M. Salcher, R. Bertuzzi, Results of pull tests of rock bolts and cable bolts in Sydney sandstone and shale. Tunn. Undergr. Space Technol. **74**, 60–70 (2018). https://doi.org/10.1016/j.tust.2018.01.004
12. M. Bastamia, K. Shahriar, M. Ghadimi, Verification of the analytical model for fully grouted rock bolts based on pull-out test (case study: Tabas coal mine). Procedia Eng. **191**, 1068–1074 (2017). https://doi.org/10.1016/j.proeng.2017.05.280
13. H. Jalalifar, An analytical solution to predict axial load along fully grouted bolts in an elasto-plastic rock mass. J. Southern Afr. Inst. Min. Metall. **111**(11), 809–814 (2011). https://doi.org/10.3724/SP.J.1037.2011.00325
14. M. Ghadimi, K. Shahriar, H. Jalalifar, Optimization of the fully grouted rock bolts for load transfer enhancement. Int. J. Min. Sci. Technol. **25**, 707–712 (2015). https://doi.org/10.1016/j.ijmst.2015.07.002
15. C. Mark, C.S. Compton, D.C. Oyler, D.R. Dolinar, Anchorage pull testing for fully grouted roof bolts, in *International Conference on Ground Control in Mining, ICGCM*, Morgantown, USA, ed. by S.S. Peng (2002), pp. 101–113
16. S.P. Signer, *Field Verification of Load Transfer Mechanics of Fully Grouted Roof Bolts* (Bureau of Mines, 1990), pp. 1–18
17. S.C. Tadolini, R.C. Dyni, *Transfer Mechanics of Full-Column Resin-Grouted Roof Bolts* (Bureau of Mines, 1991), pp. 1–14
18. M.O. Serbousek, S.P. Signer, *Linear Load-Transfer Mechanics of Fully Grouted Roof Bolts* (Bureau of Mines, 1987), pp. 1–23